Alma Mater Studiorum · Università di Bologna

Scuola di Scienze
Corso di Laurea Magistrale in Fisica

Investigation of dangling bounds in Al_2O_3 passivated Si surface using electron paramagnetic resonance (EPR)

Relatore:
Prof. Anna Cavallini

Correlatore:
Dott. Saskia Kühnhold

Presentata da:
Valentina Roberti

Sessione III
Anno Accademico 2013/2014

Abstract

Nel presente lavoro di tesi magistrale, svolto presso l'istituto Fraunhofer-ISE, Fraunhofer Institute for Solar Energy Systems, a Friburgo in Brisgovia, sono stati depositati e caratterizzati sottili film di ossido di alluminio, Al2O3, (di spessore compreso tra 3-30 nm) su un substrato di FZ-Si, silicio cresciuto con il metodo *float zone*, drogato *p*. La deposizione è avvenuta mediante plasma ALD (*plasma enhanced Atomic Layer Depostion*). La tecnica spettroscopica EPR (*Electron Paramagnetic Resonance*) è stata utilizzata per studiare l'interfaccia Si/Al2O3, con e senza la presenza di un sottile strato di ossido di silicio, SiOx, tra di essi, con lo scopo di scoprire l'origine della formazione di densità di carica negativa Qf all'interfaccia Si/Al2O3: tale carica negativa induce una passivazione per effetto di campo ed è quindi la ragione per cui il dielettrico Al2O3 risulta essere un ottimo materiale passivante.

In tale studio, si è deciso di variare alcuni parametri, come lo spessore dello strato di Al2O3, lo spessore dello strato intermedio di ossido di silicio, depositato mediante ossidazione termica (*dry thermal oxidation*), e la superficie del substrato di silicio. Oggetto di studio è stato inoltre l'effetto di trattamenti termici, come l'*annealing*, sui campioni di Si/Al2O3 e Si/SiOx/Al2O3.

Sono stati realizzati cinque differenti gruppi di campioni: per ciascuno di essi sono state impiegate varie tecniche di caratterizzazione dei materiali, come la QSSPC (*Quasi Steady State Photoconuctance*), per la misura della vita media dei portatori minoritari, e la tecnica di spettroscopia ottica SE (*spettroscopic ellipsometry*). Per quattro di tali gruppi è stato utilizzato come substrato uno strato di FZ-Si drogato *p*, di spessore 50 μm, e con una resistività di 100 Ohm·cm; per il quinto gruppo di campioni, invece, lo spessore il substrato FZ-Si ha uno spessore 250 μm e una resistività di 100 Ohm·cm.

Per ogni gruppo di campioni sono stati riportati gli spettri EPR ottenuti ed i rispettivi fit, da cui è stato possibile risalire ai fattori giromagnetici di spin g, i quali sono stati riportati in tabelle con le loro possibili attribuzioni.

E’ stato dimostrato che la presenza di uno strato di *ossido di silicio* tra il substrato di silicio e lo strato di ossido di alluminio risulta essere fondamentale per la formazione di densità di carica negativa all’interfaccia: aumentando lo spessore dello strato di SiOx (nel range 1-30 nm) si assiste ad una diminuzione di carica negativa Qf. Infatti, l’ossido di silicio si comporta come una barriera riducendo l’iniezione di portatori dal substrato di silico agli stati difettivi all’interfaccia SiOx/Al2O3. In questo studio, l’effetto sopradescritto è stato dimostrato utilizzando la tecnica COCOS (*Corona-Oxide-Semiconductor Characterization*).

Inoltre, è stato dimostrato, sempre utilizzando la tecnica *COCOS*, che per i campioni sottoposti ad *annealing*, la denistà di carica negativa *Qf* tende ad aumentare, così come il tempo di vita media dei portatori minoritari.

Analizzando gli spettri EPR, è stato possibile concludere che all’interfaccia Si/Al2O3 sono presenti difetti, denominati P_b, caratteristici dell’interfaccia Si/SiOx. Le nostre osservazioni, dunque, sono coerenti con la formazione di uno strato di ossido di silicio tra Si e Al2O3.

Dallo studio degli spettri EPR del gruppo 1, è stato possibile indentificare *tre principali stati difettivi*: un *centro isotropo*, un *centro E’* e un *centro anisotropo* (di tipo P_b). Una volta sottoposti i campioni ad *annealing*, gli spettri EPR non hanno rivelato la presenza di stati difettivi.

In tale lavoro, infine, è stata studiata la dipendenza angolare del fattore giromagnetico di spin, variando l’angolo tra il campo magnetico *B* e la normale all’interfaccia (100) in un range compreso tra 0°-90°.

Abstract

In the present thesis, performed at the Fraunhofer Institute for Solar Energy Systems, thin layers of aluminium oxide (Al_2O_3) were characterized and deposited on a silicon substrate (FZ-Si, *p doped*). Al_2O_3 deposition was performed using plasma enhanced Atomic Layer Deposition. Electron Paramagnetic Resonance (EPR) has been used to investigate the interface between Si and the high-k dielectric Al_2O_3, with or without the presence of a thermal grown SiO_x layer. The aim of this work is trying to understand the origin of the *fixed negative charge density* Q_f, that induces field effect passivation, formed at the SiO_2/Al_2O_3 interface. In our study several parameters were varied: the thickness of the Al_2O_3 layer, the interlayer SiO_x thickness, the thickness and the surface of the Si substrate. Also the effect of treatments (*annealing*) on Si/Al_2O_3 and $Si/SiO_x/Al_2O_3$ stacks were considered.

Five different groups of samples have been under study: for the first four groups, the starting substrates was p FZ-Si, 50 µm thick and with a resistivity of 100 Ohm·cm; the starting substrate for group 5 is p-FZ Si, with a thickness of 250 µm and a resistivity of 100 Ohm·cm. For each group characterization techniques were used: the optical spectroscopy technique SE (*spettroscopic ellipsometry*), for thickness measurements and the QSSPC (*Quasi Steady State Photoconuctance*), for lifetime measurements. In addition, for each group of samples, EPR spectra and fits were reported. From these fits, it was possible to obtain the electron spin g-factors: g-factor values and their possible attributions were reported in tables. It has been demonstated that the presence of a SiO_x interlayer between Si and Al_2O_3 plays a key role in the origin of the negative charge formation and in the interface defect density: an increase in the SiO_x interlayer thickness over the range 1-30 nm gives rise to a decrease in negative Q_f. As a matter of fact, SiO_x acts as a barrier, reducing charge injection from the Si substrate into defect states at the SiO_x/Al_2O_3 interface. In our study this effect has been demonstrated using the *COCOS* technique (Corona-Oxide-Semiconductor Characterization)

technique: we measured the total negative charge at the Si/SiOx/Al2O3 interface of three reference wafers and we found out the the negative charge denisity *Qf* decreases with the increase of the SiOx layer thickness.

Our observations, using EPR spectroscopy, are in line with the formation of an interfacial SiOx layer. Analysing the spectra of group 1 (Si/Al2O3), it was possible to identify an *isotropic center*, an *E'-like defect* and an anisotropic center P_{b0}-like. The E'-like defects are associated with the SiOx interface. After an annealing step, EPR did not reveal the presence of any defect states. Finally, in our work we studied the angular dependence of the g values varying the angle between B and the (100) interface normal in a range 0°-90°. In all the spectra we found the presence of signals due to the *trigonal anisotropic center*, the *isotropic center* and the *E'-like center* in line with our expectations.

Table of contents

Table of contents I

1 Introduction 5

2 Objectives of this Thesis 5

2.1 Structure of this work 8

3 Photovoltaic technologies 9

3.1 Introduction 9

3.2 The photovoltaic effect: history 11

3.3 Solar radiation 13

3.4 Solar cell short description 14

3.5 Standard Si solar cell 17

3.6 Simplest description of photovoltaic devices 18

3.7 Figures of merit 20

3.8 Material properties 21

3.9 The PERC concept 22

4 Fundamental properties of semiconductors 24

4.1 Silicon fundamental properties 25

4.2 Dopant atoms and energy levels 25

4.3 Carrier concentration 26

4.3.1 Intrinsic concentration 28

4.3.2 Charge neutrality 28

4.4 Fermi energy level 29

4.4.1 Quasi Fermi energy levels 31

4.5 Defects in semiconductors 31

4.5.1 Silicon Dangling Bonds 33

5 Recombination mechanisms 34

5.1 Radiative recombination 35

5.2 Auger recombination 37

5.3 Recombination mediated by defects 38

5.4 Surface recombination 41

5.5 Emitter recombination 43

5.6 Effective lifetime 43

6 Surface passivation 44

6.1 Chemical passivation 45

6.2 Field effect passivation 46

6.3 A short review of surface passivation materials 47

7 Crystal lattices 49

7.1 Primitive lattice cell 50

7.2 Types of lattice 51

7.3 Coordination number 52

7.4 Reciprocal lattice 52

7.5 Lattice planes and Miller indices 55

7.6 Silicon crystal structure 56

7.6.1 Silicon wafer orientation 57

8 Characterization techniques 58

8.1 Quasi-Steady State Photo Conductance (QSSPC) 58

8.2 Spectral ellipsometry 61

8.3 Electron paramagnetic resonance (EPR) 62

9 EPR: theoretical aspects 63

9.1 Historical overview 63

9.2 Orbital magnetic dipole and Larmor precession 68

9.3 Spin-orbit interaction 75

9.4 Electron-nuclear hyperfine interaction 78
9.5 g-factor 82
10 EPR spectrometer 85
10.1 Source 86
10.2 EPR cavity 87
10.3 Magnetic field 88
10.4 Signal channel 89
10.5 Magnetic field controller 89
10.6 Spectrum 90
11 Oxidation and Deposition techniques 91
11.1 Atomic Layer Deposition (ALD) 91
11.2 Dry thermal oxidation 94
12 Experimental plan and results 97
12.1 Introduction 97
12.2 EPR experiments 97
13 Conclusion 138
14 Appendix 140
14.1 Corona-Oxide-Semiconductor Characterization 140
14.2 Experimental set up: pictures 142
15 Acknowledgements 144

1 Introduction

In order to reduce the costs of photovoltaic energy, the introduction of a *passivation layer* on the rear of the crystalline-silicon solar cells seems to be a successful strategy. This layer allows the increase of the light trapping, the decrease of the surface recombination losses and higher conversion efficiency. Also the use of thinner wafers becomes possible. In 2006, *aluminum oxide (Al2O3)* nanolayers were found to be a new solution for the passivation of p- and n- type crystalline Si surfaces [2]. *Fixed negative charges* induce an accumulation layer at the p-type silicon interface that yields to a very effective field-effect passivation.

2 Objectives of this Thesis

In this work, Electron paramagnetic resonance, EPR, has been used to investigate the interface between Si and the high-k dielectric Al2O3, with or without the presence of a thermal grown SiOx layer. We also tried to understand the origin of the *negative charge* formation at the SiO2/Al2O3 interface. In this section the main properties of the dielectric Al2O3 are reported.

Al2O3 can deliver excellent passivation qualities on Si substrates [1]. Several Al2O3 deposition techniques has been established in the last few years like Plasma Enhanced Chemical vapor Deposition (PECVD) [2], plasma enhanced and thermal Atomic Layer Deposition [3], plasma enhanced and thermal ALD [4], [5] have very low surface recombination velocities ly$\sim 10\mathrm{cm} \cdot \mathrm{s}^{-1}$[2][3, 6] [7].

At the present time high efficiencies have been realized by the implementation of ultrathin Al2O3 films in laboratory and industrial solar cells.

Why is Al2O3 a very good surface passivation material?

The passivation properties of Al2O3 were already reported by Hezel and Jaeger in 1989 [8]. Al2O3 features a good field effect passivation. Due to the presence of a high density of inherent negative charges at the interface, the electric field enhanced by negative charge accumulation at the p-type Si/Al2O3 interface deflects minority charge carriers.

In addition to the field effect passivation, the Al2O3 also provides good chemical passivation of the dangling bongs, reducing interface defect density [2].

As far as optical properties are concerned, with a low refractive index of 1.65 Al2O3 is well suited to improve the optical quality at the front or at the back of the solar [3] because of low absorption in the visible part of solar spectrum. It acts as a back surface reflector for the long wavelength spectra of light to increase the light trapping inside the solar cells.

Al2O3 shows also a low dependence on injection levels [9]. Even at low illumination conditions, the solar cells passivation using aluminum oxide provides a good passivation quality.

Moreover Al2O3 has a high thermal stability [10]. In fact the passivation quality of the dielectric material should be thermally stable in order to sustain high temperature processes used in solar cell production.

During deposition processes an interfacial SiOx layer is commonly formed between the Al2O3 film and the c-Si substrate [3]. This thin SiOx layer can be formed during the Al2O3 deposition process but also during the post deposition annealing. Hoex et al. found an interfacial SiOx layer of ~ 1.5 nm using High resolution TEM image[3].

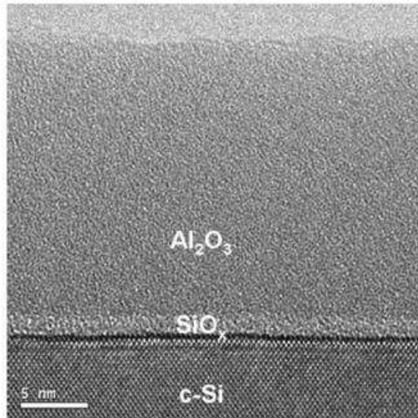

Figure 2-1: High resolution TEM image showing a 20 nm thick Al2O3 film on c-Si prepared by plasma-assisted atomic layer deposition after 30 min annealing at 425°C in a N2 environment [3]

This could be a result of the deposition process, possibly from the exposure of the substrate to the O2 plasma in the first ALD cycles [3].

The microscopic origin of defect states in the Si/Al2O3 system that lead to fixed negative charges Qf has not been clearly understood so far. It is known that the origin of the charge traps are point defects, such as vacancies and interstitials [11]. Al vacancy V_{Al} and O interstitial O_{i} produce levels in the Al2O3 bandgap below midgap [12]. These both defects are in fact likely candidates to trap negative fixed charge. When the negative charge is related to these two defects a slightly oxygen-rich structure in proximity of the Si interface would be expected. Another issue is the role of Charging of Defect states. Electron injection in the conduction band and tunneling from the dielectric into the substrate can change the charge state of an ionized defect. As far as Si/Al2O3 system is related, there are some indications that charge injection from Si into Al2O3 could play an important role in the negative charge formation. For annealed Al2O3 samples, the fixed charged density was observed to increase on the Al2O3 surface. It has been demonstrate also that an increase in the SiO2 interlayer thickness over the range 1-30 nm gave rise to a decrease in negative Qf [11, 13].

2.1 Structure of this work

In *Chapter 3*, some basic concepts of photovoltaic devices are discussed. After an introduction about photovoltaic technologies, a short description of a standard Si solar cell is given. The most significant material properties, fundamental to achive high efficiency solar cells, are summarized. Finally, a short introduction of the PERC solar cells is given: they are based of the concept of passivated emitter and rear cells.

In *Chapter 4*, the fundamental properties of semiconductors are reported: Silicon fundamental properties, dopant atoms and energy levels, carrier concentration, Fermi energy level and the main defects in semiconductor materials.

In *Chapter 5*, the main recombination mechanisms in semiconductors are discussed: radiative recombination, Auger recombination, recombination mediated by defects, surface recombination and emitter recombination.

In *Chapter 6*, the two main ways to achieve surface passivation are reported: chemical passivation and field effect passivation. Finally, a short review of surface passivation materials is given.

In *Chapter 7*, a short description of crystal lattices is given: the silicon crystal structure is described.

In *Chapter 8*, the main characterization techniques used in this work are reported: Quasi-Steady State Photoconductance (QSSPC), Spectral Ellipsometry and Electron Paramagnetic Resonance (EPR).

In *Chapter 9*, the main theoretical aspects of EPR are discussed. After a hystorical overview, orbital magnetic dipole, Larmor precession, spin-orbit interaction and electron-nuclear hyperfine interaction are described.

In *Chapter 10*, an analysis of the four essential components of an EPR spectrometer is carried out: Source, EPR cavity, magnetic field, signal channel, magnetic field controller and spectrum.

In ***Chapter 11***, the deposition and oxidation techniques used in this work are discussed: Atomic Layer Deposition (ALD) and Dry Thermal Oxidation.

In ***Chapter 12***, the detailed plan, methodology and results obtained are discussed for the five main experiments performed using EPR. The aim of the experiments is explained and for each group the detailed experimental process flow is described. The EPR sprectra are reported and compared. The final sections of each group of experiments discuss the analysis and conclusion of the experimental findings.

Chapter 13 gives the overall summary of the thesis work and the main conclusions.

Chapter 14 is the Appendix section: it includes also additional figures to supplement the information in the main work.

3 Photovoltaic technologies

3.1 Introduction

Infrared active gases, such as water vapor (H2O), carbon dioxide (CO2) and ozone (O3), absorb thermal infrared radiation emitted by the Earth's atmosphere and surface. This mechanism warms the atmosphere that emits infrared radiation: a significant portion of this energy warms the surface and the lower atmosphere. This phenomenon is called "greenhouse effect" and consituets at the present time the main origin of global warming. The amplitude of the dramatic consequences of this global warming on human, as well as vegetal and animal life is difficult to predict. Some predictions however are based largely on computer models that simulate fundamental geophysical process-

es.Modern civilization has a big need of energy, which is mainly provided by fussil fuels. As worldwide energy demand increases, conventional fossil fuels will be exhausted within the next century (the resources of fossil fuels will probably not last longer than 50 years). The side effect of using fossil fuels is the release of greenhouse gases such as carbon dioxide to the environment. The transition from fossil fuel to renewable energy sources is therefore necessary. Renewable electricity or power from wind, water and sun will play a main role in a safe and stable energy transition [1].

The major candidate for obtaining energy from the sun is the solar cell[1]. Solar Photovoltaic systems provide clean energy from small scale residential to large industrial applications. Recently researches of low-cost flat-panel solar panels, thin-film devices and many innovative concepts have increased. The global solar photovoltaic market has shown a significant growth due to the use of this source of solar power generation.

New photovoltaic installation have been made in the year 2010 and in 2011, a total of 69 GWp of PV panels were installed worldwide with a capacity to generate some 85TWh of electricity annually. PV technology is become more and more important and constitutes a competitive solution for power generation with high effriciency (obtained in laboratory) of above 24 %.

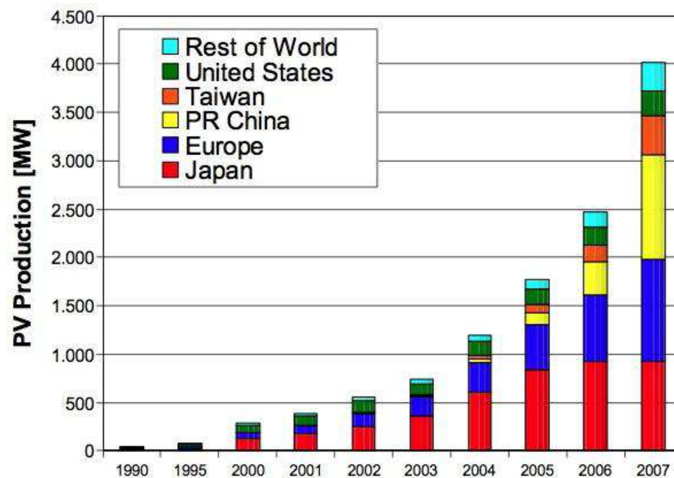

Figure 3-1: Worl PV Cell/Module Production from 1990 to 2007 (data source: PV News[Pvn 2008], Photon International [Pho 2008])

To reduce the total cost related to solar technology must be reduced. One way to achieve this goal is the reduction of wafer thickness. A new generation of thinner solar cell has begun. However, increasing the surface to volume ratio electrical losses occur due to surface recombination. This problem causes losses in electrical efficiency in the solar cells. To minimize these losses, due mostly to the presence of dangling bonds at the crystal surface, thin dielectric layers are applied to reduce surface recombination. Standard passivation layers are Silicon dioxide (SiO2), Silicon Nitride (SiNx) and hydrogenated amorphous Silicon (a-Si:H). These passivation layers however are found not to be suitable during all cases of application limitin solar cell efficiency.

New technologies and new passivation layer are therefore required. One such technology coul be the passivated emitter and rear solar cell (PERC): the cell is passivated on both emitter and rear side in order to reduce recombination at the interface. An alternative passivation layer colud be Aluminum Oxide (Al2O3): it has suitable properties such as a refractive index of about 1.65 with low absorption in the visible region of the solar spectrum and low density of interface states leading to high quality of chemical passivation.

3.2 The photovoltaic effect: history

Solar cells operate by converting sunlight directly into electricity using the electronic properties of a class of material known as semiconductors. A semiconductor material or device is said to be “photovoltaic” when exposure of the material to light that can be absorbed by the material is able to transform the energy of the light photons into electrical energy in the form of a current and voltage. The number of materials that are able to exhibit photovoltaic characteristic is large but the number of such materials or devices that are able to make the transformation of solar radiation to electrical energy with high efficiency , of the order of 20%, at low cost and with stability is not large [3].

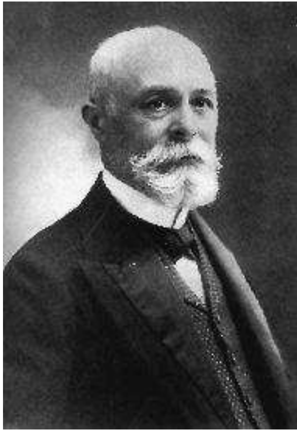

Figure 3-2: Antoine-Henri Becquerel

The photovoltaic effect was discovered by Becquerel, a French experimental physicist, while experimenting with an electrolytic cell made up of two metal electrodes in 1839 [3]. Willoughby Smith discovered the photoconductivity of selenium in 1873. In 1904 Hallwachs discovered that a combination of copper and cuprous oxide was photosensitive. Solar efficiencies of about 1% characterized selenium and copper oxide cell by about 1914.[3] In this year Einstein published his paper on the photoelectric effect.

Millikan provided experimental proof of the photoelectric effect in 1916. Two year later a Polish scientist named Czochralski developed a way to grow single-crystal silicon. In 1954 the PV effect in Cd was reported; primary work was performed by Rappaport, Loferski and Jenny at RCA. Bell Labs researchers Pearson, Chapin, and Fuller reported their discovery of 4.5% efficient silicon solar cells; this was raised to 6% only a few months later (by a work team including Mort Prince). Chapin, Fuller, Pearson (AT&T) submitted their results to the Journal of Applied Physics. AT&T demonstrated solar cells in Murray Hill, New Jersey, then at the National Academy of Science Meeting in Washington, DC. The year 1954 also dates the announcement of the first all-thin-film cell composed of a $\mathrm{Cu_xS/\ CdS}$ junction with an efficiency of 6%, later increased to over 9%. One year later, Western Electric began to sell commercial licenses for silicon PV technologies; early successful products included PV-powered dollar bill changers and devices that decoded computer punch cards and tape. Bell System's demonstration of the type P rural carrier system began in Americus, Georgia.[1, 3] In 1964 Peter Glaser, A.D. Little, conceived the idea of a satellite solar power station. Tyco Labs developed the edge-defined, film-fed growth (EFG) process, first to grow crystal sapphire ribbons and then silicon. To date, solar cells have been made out of many other semiconductors, using various device configurations and employing single crystal, polycrystal, and amorphous thin-film structures [1].

3.3 Solar radiation

Nuclear fusion reaction is the origin of the radiative energy output from the sun. In every second, about 6x10^{11} kg of $\mathrm{H_2}$ is converted to He, that corresponds to a net mass loss of about 4x10^{3} kg , that is converted through the Einstein relation:

$$E = mc^2 \tag{3.1}$$

to 4x10^{20} kg . This energy is emitted primarily as electromagnetic radiation in the ultraviolet to infrared and radio spectral ranges. Now the total mass of the sun is about 2x10^{30} kg. The sunlight is attenuated by the atmosphere when it reaches the earth's surface: this is mainly due to water-vapor absorption in the infrared, ozone absorption in the ultraviolet, and scattering by airborne dust and aerosols. Air mass quantifies the degree to which the atmosphere affects the sunlight received at the earth's surface. The air mass number (AM) is the secant of the angle between the sun and the zenith and it measures the atmospheric path length relative to the minimum path length when the sun is directly overhead. The AM0 spectrum represents the solar spectra outside the earth's at-mosphere and the AM1 spectrum represents the sunlight at the earth's surface when the sun is at zenith and the incident power is about 925 W/m^2 .The AM2 spectrum is the spectrum for $\theta = 60^\circ$ and has an incident power of $691\ \mathrm{W/m^2}$[1].

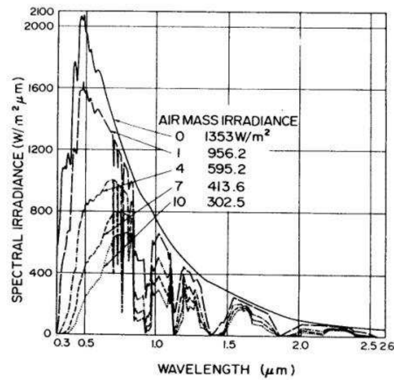

Figure 3-3: Solar spectrum at different air-mass conditions [1]

Figure 3-3 shows the solar spectrums at various AM conditions. The upper curve is the AM0 condition. This spectrum is the relevant one for satellite and space-vehicle application. For terrestrial applications, the AM1.5 conditions, with sun at 45° above the horizon, represent an energy-weighted average. Because each photon produces an electron-hole pair, the solar power has to be converted in photon flux [1]. To convert the wavelength to photon energy we have to use this expression is used:

$$\lambda = \frac{c}{\nu} = \frac{1.24}{h\nu(e\mathrm{V})}\ \mu\mathrm{m} \tag{3.2}$$

The total power for AM1.5 is $844\ \mathrm{W/m^2}$[1].

3.4 Solar cell short description

Semiconductors are crystalline materials whose outer shell atomic levels exhibit an energy band structure.This band structure is due to the close, periodic arrangement of the atoms in the crystal which causes an overlapping of the electron wavefunctions. The so called Valence Band (VB) is the

highest occupied energy level at zero point temperature. The Conduction Band (CB) is the next unoccupied energy level at the zero point. There is an energy gap between valence and conduction bands of the order of $\sim$ 1eV. Figure (3.4) schematically illustrates this basic structure consisting of a valence band,a forbidden energy gap and a conduction band. The band configuration for conductors and insulators is also shown for comparison. At zero temperature all allowed energy states in the valence band are completely occupied and all allowed energy states in the conduction band are completely empty. As the temperature increases, the number of thermally excited electrons across the forbidden band gap increases. The Fermi energy level corresponds to the energy of the highest occupied state in the system.

The probability of occupation of allowed energy states of any given energy E in thermal equilibrium is described by the Fermi-Dirac distribution [4]:

$$f(E) = \frac{1}{1 + \exp\left(\frac{E - E_F}{k_B T}\right)} \tag{3.3}$$

where T is the temperature in Kelvin and k_B is the Boltzmann's constant and E_F is the Fermi energy level.

Figure (3.4) schematically illustrates this basic structure consisting of a valence band,a forbidden energy gap and a conduction band. The band configuration for conductors and insulators is also shown for comparison.

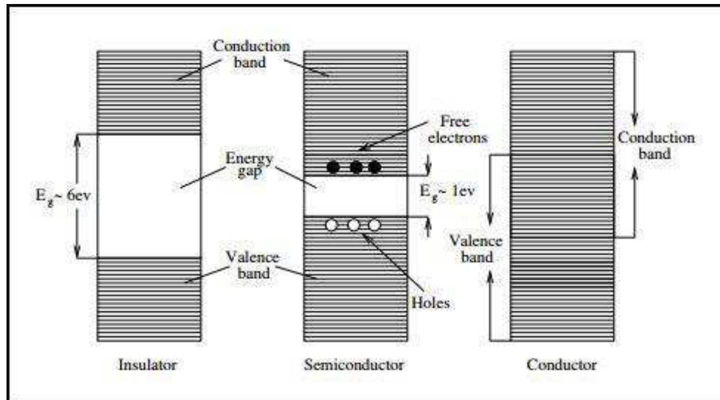

Figure 3-4: Energy band structure of conductors, insulators and semiconductors

When a photon with energy larger than the Band Gap strikes an electron in the silicon crystal lattice, the energy gets absorbed and the electron is ejected from its state in the Valence Band to a free excited state in the Conduction State and it can contribute to the electrical conduction.

A solar cell works on the principle of the '' photovoltaic effect''. When a solar cell is exposed to light, the photon energy is absorbed by the semiconducting material: electron-hole pairs are created, resulting in the generation of free charge carriers. These charge carriers are separated across a space charge region (*p-n* junction). At the *p-n* junction the potential energy of the n-type and p-type substates become identical.The *p-n* junction permits the partial separation of charges, allowing electrons to diffuse to emitter and holes to diffuse to the bulk to reach the junction terminals. Near the p-n junction the electrons diffuse into the vacant holes in the p material causing a depletion zone, the space charge region (SCR)This depletion zone acts like an insulator preventing other free electrons in the n-type silicon and holes in the p-type silicon from combining[1, 4].This forms an electric field across the *p-n* junction, opposing the diffusion force.Finally, the movement of these charges through an external circuit creates electrical generation. A potential difference is built by the charge accumulation at the emitter (n-region) and bulk (p-region) terminals. The charge concentration at these terminals develops a photocurrent which flows in the opposite direction respect to the diffusion current. An external load is connected between the front and the back contacts of

the solar cell. When the overall magnitude of photocurrent is bigger than the diffusion current a current flow is extracted.

The crystalline silicon (c-Si) solar cell, which dominates the PV market at present, has a simple structure, and provides a good example of a typical solar cell structure. In the next chapter a standard Si solar cell is described.

3.5 Standard Si solar cell

The structure of a silicon solar cell is composed of a bulk substrate (usually p-type semiconductor) and an emitter (n-type semiconductor) forming a p-n junction.

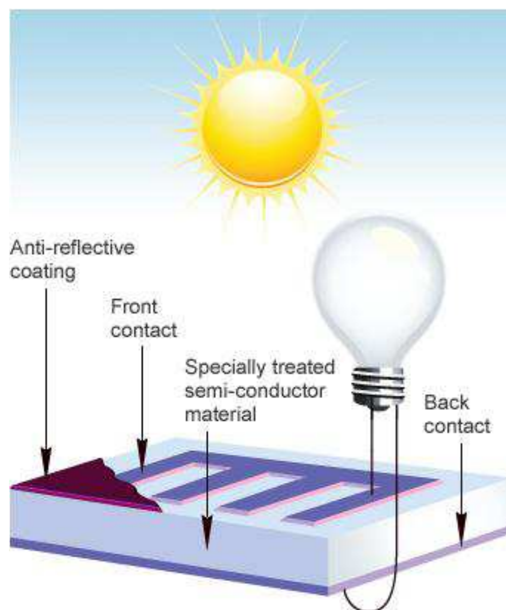

Figure 3-5: Illustratiuon of a standard solar-cell. The base and the emitter form a p-n junction. Electrons and holes are separated by an electric field and a potential difference is created

At the front surface above the emitter a thin dielectric layer is usually employed as an Anti-ReflectionCoating (ARC).This Anti-Reflection Coating is used to reduce reflection losses at the front surface.

ARC consists of a thin dielectric layer, with a certain thickness so that light reflection gets disabled due to destructive interference. Of course this interference condition is true only for a certain wavelength. The antireflection coating is usually optimized for λ=600 nm.

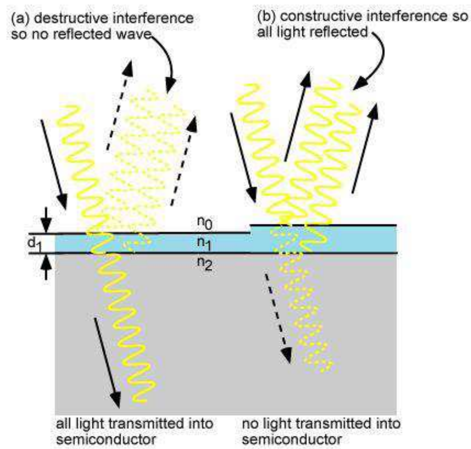

Figure 3-6: ARC consist of a dielectric layer, with a specially chosen thickness so that interference effects in the coating cause the wave reflected from the anti-reflection coating top surface to be out of phase with the wave reflected from the semiconductor surfaces. These out-of-phase reflected waves destructively interfere with one another, resulting in zero net reflected energy

3.6 Simplest description of photovoltaic devices

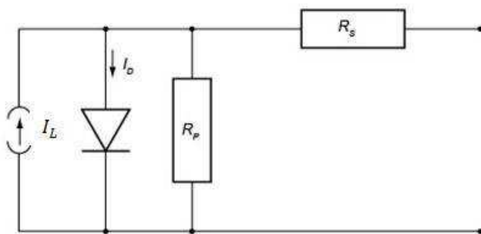

Figure 3-7: Simple equivalent circuit for a photovoltaic cell, with a current generator with total light current I_L, a diode with total dark current I_D, a series resistance R_S, and a parallel resistance R_P [3]

We can consider an “ideal device” with $R_S = 0$ and $R_P = \infty$. The current density *J* flowing in the device in the presence of photo excitation can be expressed with this equation:

$$J = J_0 \left[\exp\left(\frac{q\phi}{AkT}\right) - 1\right] - J_L \tag{3.4}$$

The first term on the right, $J_0 \left[\exp\left(\frac{q\phi}{AkT}\right) - 1\right]$, is the forward current driven by the voltage ϕ and the second term, J_L is the reverse current that is associated with photoexcitation. J_0 is also called “reverse saturation current” of the diode. *A* is the “ideality factor” that has a value depending on the mechanism of the junction transport. If the voltage is 0 we have the short-circuit condition and there is zero current in the dark.

In the light we have:

$$J_{SC} = -J_L \tag{3.5}$$

The short circuit current is controlled only by the photoinduced current generation and recombination processes. If the total current under illumination is zero (open-circuit condition) we obtain:

$$\phi_{OC} = \left(\frac{AkT}{q}\right) \ln\left[\left(\frac{J_L}{J_0}\right) + 1\right] \tag{3.6}$$

We can see that the open-circuit voltage is controlled by the current generation and recombination processes but also by the nature of the junction transport currents.

The relation between J_{SC} and ϕ_{OC} is given by:

$$J_{SC} = J_0 \left[\exp\left(\frac{q\phi_{OC}}{AkT}\right) - 1\right] \tag{3.7}$$

3.7 Figures of merit

The efficiency of a solar cell is maximal when the product of the current density J and the voltage ϕ is a maximal. The efficiency η can be expressed in this way:

$$\eta = \frac{P_m}{P_{rad}} = \frac{J_m \phi_m}{P_{rad}} = \frac{J_{sc} \phi_{oc} FF}{P_{rad}} \quad (3.8)$$

where P_{rad} is the total radiation power incident on the cell and FF is called the fill factor: it is the measure of the “sqareness” of the light $J - V$ curve.

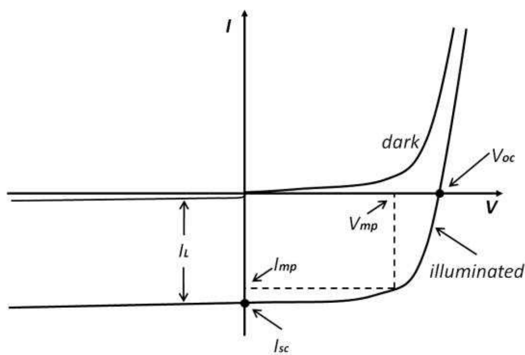

Figure 3-8: I-V characteristic of a solar cell during light and dark condition[3]

J_m and ϕ_m are respectively the values of current density and voltage at the condition corresponding to maximum power.

The definition of the fill factor *FF* is given by the following equation:

$$FF = J_m \phi_m / J_{sc} \phi_{oc} \quad (3.9)$$

with:

$$\phi_m = \phi_{oc} - (Ak_BT/q)\ln[(q\phi_m/Ak_BT) + 1] \quad (3.10)$$

Once a value for ϕ_m has been obtained, the value of $J_m$and the maximum power $P_m = J_m\phi_m$ can be obtained.

3.8 Material properties

We can summarize the most significant material properties that are fundamental to achive high efficiency solar cells.

The band gap of the absorbing material should be small enough to allow absorption of an appreciable portion of the solar spectrum but at the same time large enough to minimize the reverse saturation junction current density. The diffusion length of minority carriers L_{min} must be as large as possible so that carriers excited by light will be able to diffuse to the junction and be collected before they recombine with carriers of the opposite sign.

$$L_{min} = (D_{min}\tau_{min})^2 \quad (3.11)$$

D_{min} ist he diffusion constant and τ_{min} ist he lifetime of minority carriers

Using the Einstein relation:

$$\frac{D_n}{\mu_n} = \frac{D_p}{\mu_p} = \frac{k_BT}{q} \quad (3.12)$$

Equation (3.9) becomes:

$$L_{min} = \left[\left(\frac{k_B T}{q}\right)(\mu\tau)_{min}\right]^{1/2} \tag{3.13}$$

where μ_{min} and k_B are the mobility for minority carriers and the Boltzmann constant respectively. It is desired, therefore, to have a material in which the minority carriers have large mobility and lifetime.

The junction structure and composition are also important because they determine the magnitude of the junction transport current density $J_0$and of the ideality factor A. To produce junctions with as low junction current as possible the formation of the semiconductor junction must be carefully controlled [3].

3.9 The PERC concept

In PERC solar cells, based of the concept of passivated emitter and rear cells, surface passivation is used to enhance the efficiency of solar cells. In fact recombination losses at the cell surface are reduced. In contrast to standard solar cells, here passivation is applied at the front as well at the rear surface. In addition to the ARC, Anti-Refletion Coating, in these solar cells additional technologies such as laser fired electrical contacts and local Aluminum BSF (Back surface field) are applied [5].

High-efficiency crystalline solar cells require three basic elements:

- The silicon substrate must be high quality with a long carrier lifetime.

- The cell should have low surface reflection with a good light-trapping capability.
- Emitter design should be able to collect all light-generated carriers and good metal contacts for low series resistance.

Advanced crystalline cell types such as PERC have been developed to integrate the three basic cell design requirement.

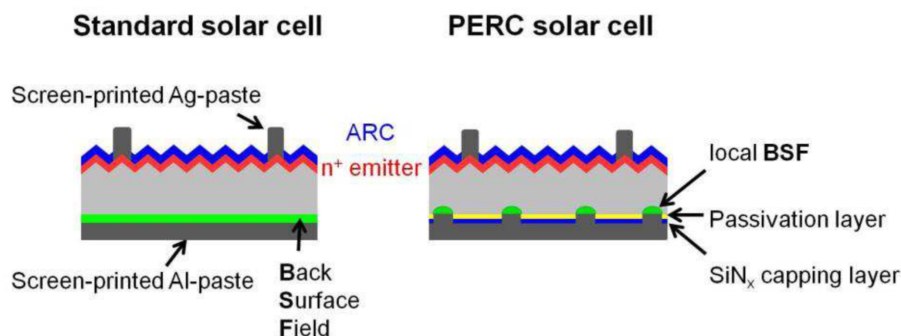

Figure 3-9: Schematic diagram of a typical industrial solar cell with a full-area Al-BSF (left) and a PERC solar cell (right) with a dielectric rear side passivation layer and screen-printed local aluminum contacts on the rear. The emitter on the textured front side is covered with an anti-reflective coating (ARC)

The development of p-type PERC solar cells using mono-crystalline silicon substrates involves an alkaline chemical texturing process: silicon wafers are put in an alkaline solution to create upright pyramids on the surface. Since the wafers are dipped in a chemical bath, ther is pyramid formation at the rear as well as at the front surfaces although ideally texturing process is required only on the front surface of the cells to reduce reflection losses. The texturing step is a high temperature diffusion process to create an emitter above the bulk substrate: in this way we have a p-n junction diode at the semiconductor front interface. During the diffusion process, there is a formation of an emitter layer at the rear surfaces of the c-Si substrate: an undesired process. During the diffusion process we have another undesirable process: the formation of an emitter layer at the rear surfaces of the c-Si substrate. The rear surface is polished in order to remove the emitter layer formed at the

rear surface and also to increase the effect of surface passivation and the texture. The total rear surface area is reduced after the polishing of the surface: that lowers the probability of defects at the cell surface. Therefore, flat surface results in reduced probability of surface recombination at the rear interface. When the dielectric material is applied, the effect of passivation is further increased. The next step is the application of passivation layers at the front surface that acts also as an ARC in order to avoid surface recombination of charge carriers at the interface. The final step is the creation of electrical metal.

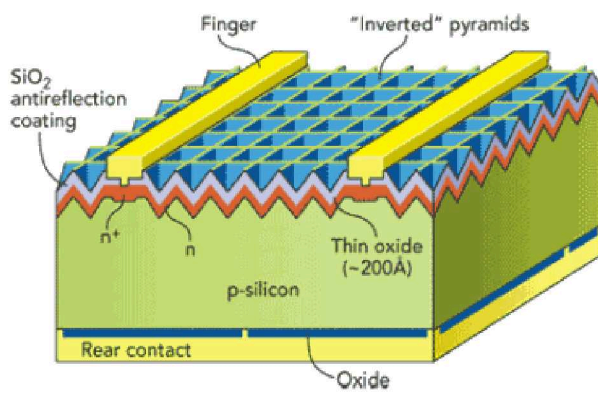

Figure 3-10: Complete PERC solar cell

4 Fundamental properties of semiconductors

We define an intrinsic semiconductor as a material without impurities like foreign atoms within the crystal. An extrinsic semiconductor is defined as a semiconductor in which a certain number of impurities are located. This technic is called doping. Doping has a fundamental influence on the

semiconductor characteristics. For example the thermal-equilibrium of the electron and hole concentration differs from the intrinsic carrier concentration [1, 2].

4.1 Silicon fundamental properties

Silicon is a light chemical element belonging to group 4 in the periodic table. The atom has 14 electrons in its shells. The two inner shells are full (2 and 8 electrons) while the outmost shell contains 4 electrons. Silicon is the second most abundant element and comprises over 20 per cent of the earth's crust. It occurs in nature never as the element, but as silica (SiO_2) and silicates. SiO_2 abounds in massive form as quartzite, agate, jasper, carnelian, opal and flint. The silicates include such minerals as micas and zeolites.

To be used as semiconductor, silicon needs to have high purity. Otherwise it is not capable of reaching high enough efficiency for the solar cell marked.

4.2 Dopant atoms and energy levels

We can consider a silicon lattice in which we add a group V element, such as phosphorous as a substitutional impurity. The group V element, such as phosphorous, has five valence electrons and four of these will contribute to the covalent bonding with the silicon atoms. The fifth Phosphorus open bound provides an additionally electron. The phosphorus atom without the donor electron is positively charged. This donor electron is bound to the phosphorus atom at very low temperatures. If a small amount of energy is added to the donor electron, it can go to the conduction band, leaving behind a positive charged phosphorus ion. Now the electron in the conduction band can move through the crystal and leaving the positive charged ion fixed in the crystal. This type of

impurity atoms is called “donor impurity atoms”. These atoms add electrons to the conduction band but they don’t create holes in the valence band. The material is at this moment an n-type semiconductor.

We can consider now a group 3 element, such as boron. It has three valence electrons, which are all taken up in the covalent bonding. To occupy this empty position, its energy must be greater than that of the valence electrons, since the net charge state of the boron atom would now be negative. This energy however is not sufficient to reach the conduction band. The empty position associated where the boron atom becomes occupied and other valence electron positions become vacated: they are holes in the semiconductor material. The group 3 atom accepts an electron from the valence band and so is referred to as an “acceptor impurity atom”. This type of material is a p-type semiconductor [2].

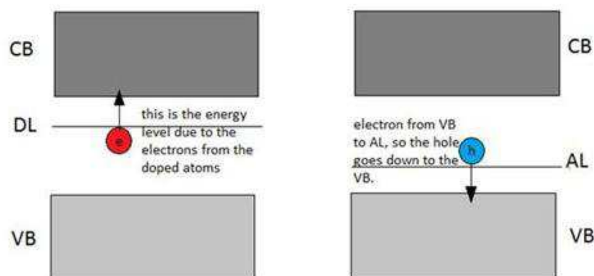

Figure 4-1: Simplified energy-band diagrams for degenerately doped n-type (left) and p-type (right) semiconductors

4.3 Carrier concentration

The Boltzmann statistic can be used to calculate the carrier concentration for non-degenerate semiconductors in equilibrium:

$$n_0 = n_i \exp\left(\frac{E_F - E_i}{qV_{th}}\right) \tag{4.1}$$

$$p_0 = p_i \exp\left(\frac{E_i - E_F}{qV_{th}}\right) \tag{4.2}$$

where n_0 and p_0 are the equilibrium electron and hole densities, n_i is the intrinsic carrier density, E_i and E_F are the intrinsic energy level and the Fermi level respectively. The expression of the thermal voltage is:

$$V_{th} = \frac{k_B T}{q} \tag{4.3}$$

k_B is the Boltzmann constant, T is the temperature and q in the charge. By definition, in non-degenerate semiconductors, the doping concentrations are smaller respect to N_C, the effective density of states in the conduction band, and the Fermi levels are more than several $k_B T$ below E_c, the energy of the conduction band.

In the case of degenerate semiconductors, where n- or p-concentrations are near or beyond the effective density of states, the value of Fermi-Dirac integral has to be used instead of the Boltzmann statistics.

4.3.1 Intrinsic concentration

For intrinsic semiconductors at finite temperatures, thermal agitation occurs, which results in continuous excitation of electrons from the valence to the conduction band, and leaving an equal number of holes in the valence band. At steady state, the net result is:

$$n = p = n_i \tag{4.4}$$

The Fermi level for an intrinsic semiconductor is:

$$E_F = E_i = \frac{(E_C + E_V)}{2} + \frac{k_B T}{2} \ln\left(\frac{N_V}{N_C}\right) \tag{4.5}$$

For non-degenerate semiconductors the product of the majority and minority carrier concentration is fixed to be:

$$pn = N_C N_V \exp\left[-\frac{E_g}{k_B T}\right] = n_i^2 \tag{4.6}$$

which is known as the mass-action law. For degenerate semiconductors, $pn < n_i^2$.

4.3.2 Charge neutrality

In thermal equilibrium, the semiconductor crystal is electrically neutral. The electrons are distributed among the various energy states, creating negative and positive charges, but the net charge

density is zero. This condition of charge-neutrality is used to determine the thermal-equilibrium electron and hole concentrations as a function of the impurity doping concentration.

A compensated semiconductor is one semiconductor that contains both donor and acceptor impurity atoms in the same region. If $N_A = N_D$ we have a completely compensated semiconductor, that is the characteristics of an intrinsic material. The charge neutrality condition is express by equating the density of negative charges to the density of positive charges.

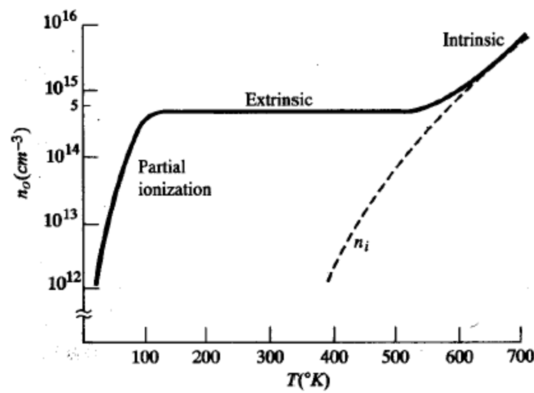

Figure 4-2: Electron concentration versus temperature showing three regions: partial ionization, extrinsic and intrinsic [1]

4.4 Fermi energy level

The position of the Fermi energy level within the bandgap can be determined for the thermal equilibrium electron and hole concentrations. We assume the Boltzmann approximation to be valid then we have:

$$n_0 = N_C \exp\left[-\frac{(E_C - E_F)}{k_B T}\right] \tag{4.7}$$

And we can solve for $E_C - E_F$. If we consider an n-type semiconductor in which the concentration of donors, N_d is >> n_i we have:

$$E_C - E_F = k_B T ln\left(\frac{N_C}{N_d}\right) \tag{4.8}$$

The distance between the bottom of the conduction band and the Fermi energy is a logarithmic function of the donor concentration: as the donor concentration increases, the Fermi level moves closer to the conduction band. We can derive the same type of equation for a p-type semiconductor, assuming that the concentration of acceptors, $N_a$is >>n_i. We have:

$$E_F - E_V = k_B T ln\left(\frac{N_V}{N_a}\right) \tag{4.9}$$

The distance between the Fermi level and the top of the valence-band energy for a p-type semiconductor is a logarithmic function of the acceptor concentration: as the acceptor concentration increases the Fermi level moves closer to the valence band.

E_F is a function of temperature also. As the temperature increases, n_i increases, and E_F moves closer to the intrinsic Fermi level.

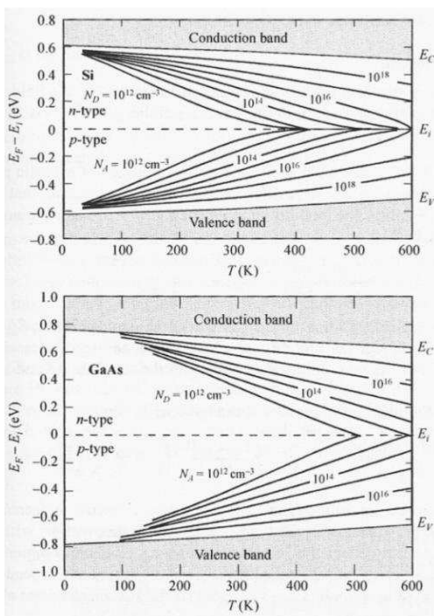

Figure 4-3: Fermi level for (a) Si and (b) GaAs as a function of temperature and impurity concentration [1]

4.4.1 Quasi Fermi energy levels

If excess carriers are created in a semiconductor, we are no longer in thermal equilibrium and the Fermi energy is strictly no longer defined. However we can define a quasi-Fermi level for electron and a quasi-Fermi level for holes that apply for non-equilibrium. We can call δn and δp the excess electron and hole concentration respectively and we can write:

$$n_0 + \delta n = n_i \exp((E_{Fn} - E_{Fi}) / k_B T) \quad (4.10)$$

And

$$p_0 + \delta p = n_i \exp((E_{Fi} - E_{Fp}) / k_B T) \quad (4.11)$$

Where E_{Fn} and E_{Fp} are the quasi-Fermi energy levels for electrons and holes respectively. The total electron concentration and the total concentration are function of the quasi-Fermi levels.

4.5 Defects in semiconductors

Crystalline defects are regions where the microscopic arrangement of ions differs from that of a perfect crystal. Defects are called surface, line, or point defects if the imperfect region is bounded on the atomic scale in one, two or three dimension respectively [6].

The most important kinds of defects in a semiconductor material are the following:

- Vacancy and interstitial

These defects are called point defects and they consist of the absence of ions or presence of extra ions. Such defects are entirely responsible for the electrical conductivity of ionic crystal and can alter the optical properties such as their color.

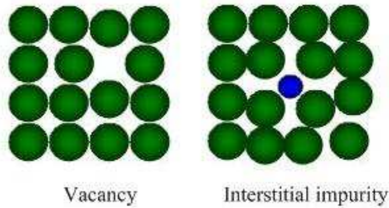

Figure 4-4: Schematic representation of vacancy and interstitial impurity

- Line defects

Linear crystal defects are edge and screw dislocations.

Edge dislocations consist of an extra half plane of atoms “inserted” into the crystal lattice. Due to the edge dislocations metals possess high plasticity characteristics: ductility and malleability.

Screw dislocation forms when one part of crystal lattice is shifted relative to the other crystal part. It is called screw as atomic planes form a spiral surface around the dislocation line.

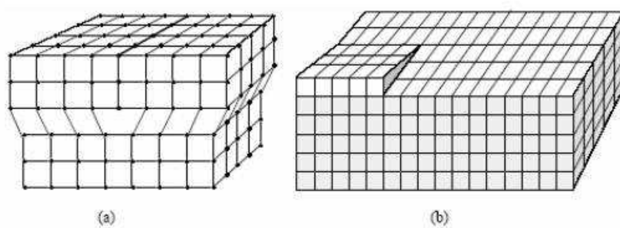

Figure 4-5: a) edge dislocation b) screw dislocation

- Two dimensional defects

Stacking faults (SF), Twin Boundaries (TB), Grain Boundaries (GB) Subboundaries (SB) and Surfaces are the typical examples of two dimensional defects in crystal. They have significant influence

on the electrical and oprical properties of semiconductors. Most of these influenced is caused by the defct levels at the boundaries of the semiconductors which are charged and attract compensating charges in the adjacent space charge of the crystal.

- Shallow- and Deep Level Defects

In a semiconductor there may exist following two types of electronically active defects: Shallow Level Defects and Deep Level Defects. This distinction is related to their different position in the energy band gap with respect to the conduction or valence band. Deep levels have highly localized wave function.

4.5.1 Silicon Dangling Bonds

The silicon atoms possess four valence electrons and therefore require four bonds to saturate the valence shell. In the crystalline structure each silicon atom establishes bonds to its four neighboring atoms, leaving no unsaturated bond behind. At the surface of the silicon crystal atoms are missing and traps are formed.

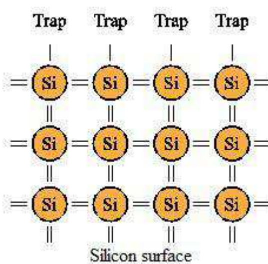

Figure 4-6: Traps formation at the silicon surface

After oxidation most interface states are saturated with oxygen atoms [6].

5 Recombination mechanisms

When the thermal-equilibrium condition of a semiconductor system is disturbed the mass-action law is no more valid:

$$pn \neq n_i^2 \tag{5.1}$$

Processes exist to restore the system in equilibrium.

These processes are recombination processes when $pn > n_i^2$ and thermal generation processes when $pn < n_i^2$.

There are three fundamental recombination mechanisms in semiconductors: **radiative**, **Auger** and **multi-phonon** recombination. These three processes differ in the way the excess carrier energy is dispersed, being mediated by phonons, electrons and phonons respectively All three mechanisms can occur either from band-edge to band-edge, or via an intermediate level in the band-gap. However, when recombination occurs from band to band, it occurs principally through the radiative and Auger processes. In contrast, recombination through intermediate levels is almost exclusively dominated by multi-phonon emission.

Multi-phonon recombination through intermediate levels is known as Shockley-Read-Hall (SRH) recombination. This defect-mediated process is not intrinsic: it requires the presence of localized levels within the band-gap. SRH recombination can occur either as a result of surface states, which are typically caused by dangling bonds, or through bulk defects or impurities [4].

5.1 Radiative recombination

Radiative recombination is the process of optical absorption: it involves the emission of a photon with energy approximately equal to that of the band gap. These emitted photons may be absorbed again before they escape from the crystal. However these low-energy photons are weakly absorbed. The radiative recombination rate U_{rad} depends on both the electron and hole concentrations, since one of each is required for the process to occur. In p-type material we have the following expression:

$$U_{rad} = B\Delta n(N_a + \Delta n) \tag{5.2}$$

where ***B*** is a constant and the equilibrium electron concentration has been neglected. The radiative recombination lifetime τ_{eff} is given by:

$$\tau_{eff} = \frac{1}{B(N_A + \Delta n)} \tag{5.3}$$

because the recombination lifetime is expressed in this form:

$$\tau = \frac{\Delta n}{U} \tag{5.4}$$

Radiative recombination is the dominant recombination process in direct semiconductors such as GaAs. In indirect semiconductors such as Silicon such processes are less probable because of the requirement for simultaneous photon and phonon emission. Figure (5.1) shows the radiative lifetime

as a function of excess carrier concentration Δn in comparison to Auger and Shockley-Reed Hall, SRH recombination lifetime for a $1\,\Omega\,\mathrm{cm}$ p-type silicon, a typical resistivity for solar cells.

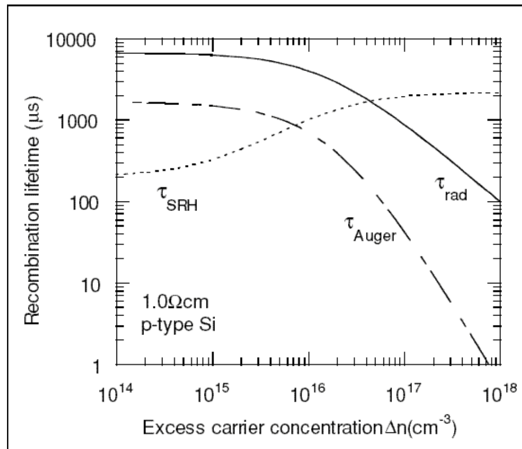

Figure 5-1: Radiative lifetime as a function of excess carrier concentration Δn in comparison to Auger and Shockley-Reed Hall, SRH recombination lifetime for a $1\,\Omega\,\mathrm{cm}$ p-type silicon [1]

The figure shows that SRH recombination tends to dominate at low carrier concentrations. For more lightly doped samples, radiative recombination can overtake the Auger process in low-injection, but in these cases SRH recombination is usually completely dominant.

The radiative recombination coefficient is temperature dependent and it decreases with increasing temperature. Its temperature dependence is shown in table:

Table 5-1: Temperature dependence oft he radiative recombination coefficient

$Temperature(K)$	$\Delta n\ (\mathrm{cm}^{-3})$	$B(T)(\mathrm{cm}^3/\mathrm{s})$
77	1.95×10^{-20}	8.01×10^{-14}
90	8.87×10^{-15}	4.57×10^{-14}
112	3.69×10^{-8}	2.14×10^{-14}
300	9.97×10^{-9}	4.73×10^{-15}

5.2 Auger recombination

Auger recombination occurs when the energy released by the recombination of an electron-hole pair is carried off by a third free carrier. In lowly-injected p-type silicon, the third carrier is most likely to be a hole, and the corresponding recombination rate:

$$U_{Auger} = C_p \Delta n N_a^2 \tag{5.5}$$

where $C_p = 9.9 \times 10^{-32} c\mathrm{m}^{-6}\mathrm{s}^{-1}$ is the low-injection Auger coefficient for p-type silicon. A similar expression holds for n-type silicon where $C_n = 2.8 \times 10^{-31}\mathrm{cm}^{-6}\mathrm{s}^{-1}$.

The low-injection Auger lifetime then for p-type silicon is:

$$\tau_{Auger} = \frac{1}{C_p N_a^2} \tag{5.6}$$

For low injection and:

$$\tau_{Auger} = \frac{1}{C_a \Delta n^2} \tag{5.7}$$

For high injection; where $C_a = 1.66 \times 10^{-30}\mathrm{cm}^{-6}\mathrm{s}^{-1}$ is the *ambipolar* Auger coefficient. Non interacting free particles should result in C_a being equal to the sum of C_n and C_p.

Like radiative recombination, Auger processes are intrinsic, in the sense that their presence does not depend on the specific techniques used for silicon crystal growth.

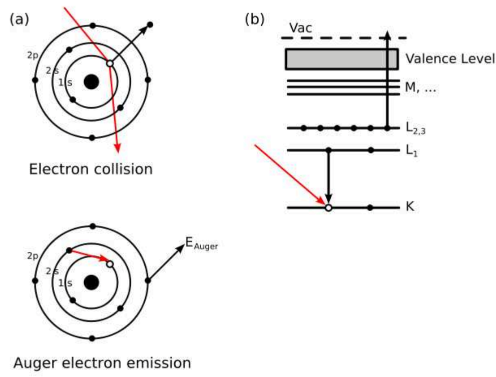

Figure 5-2: Example of Auger recombination

5.3 Recombination mediated by defects

Recombination center can act also as traps, in which a carrier is captured and subsequently injected back into the band from which it came. Trapping changes the free carrier concentration and can impact strongly on the overall carrier dynamics. We can write the first order differential equations in Δn e Δp:

$$g_e - \frac{d\Delta n}{dt} = \frac{\Delta n}{\tau_n} = \frac{1}{\tau_{n0}}\left[\frac{(n_0 + n_1 + \Delta n)(\Delta n - \Delta p)}{N} + \frac{\Delta n n_1}{n_0 + n_1}\right] \tag{5.8}$$

$$g_e - \frac{d\Delta p}{dt} = \frac{\Delta p}{\tau_p} = \frac{1}{\tau_{p0}}\left[\frac{(p_0 + p_1 + \Delta p)(\Delta p - \Delta n)}{N} + \frac{\Delta p p_1}{p_0 + p_1}\right] \tag{5.9}$$

Here g_e is the generation rate arising from external illumination and n_0 and p_0 are the electron and hole concentration in thermal equilibrium. τ_{n0} and τ_{p0} are the fundamental electron and hole lifetimes and are related to the carrier thermal velocity v_{th}, the recombination center density N and the capture cross-sections σ_n and σ_p of the center.

$$\tau_{p0} = 1/Nv_{th}\sigma_p \tag{5.10}$$

$$\tau_{n0} = 1/Nv_{th}\sigma_n \tag{5.11}$$

The factors $n_1$and p_1 are the electron and hole densities when the Fermi level corresponds to the recombination center energy E_T :

$$n_1 = N_C \exp\left(\frac{E_T - E_C}{KT}\right) \tag{5.12}$$

$$p_1 = N_V \exp\left(\frac{E_C - E_G - E_T}{KT}\right) \tag{5.13}$$

where N_C and N_V are the effective densities of states at the conduction and valence band edges, and E_C and E_G are the conduction band energy and the band-gap energy.

The equations on the left of equation (5.8) and equation (5.9) define the carrier lifetimes in terms of the carrier densities and generation rate, which may be a function of time. The lifetime defined in this way is valid for arbitrary illumination conditions. If we consider the full equations, the aim is to solve them for τ_n and τ_p in terms of Δn or Δp. Under steady-state conditions, when the derivative terms are zero, there exist general analytic solutions for τ_n and τ_p.

In samples where the recombination center density *N* is relatively large, these full expressions should be used. If *N* is small compared to Δn and Δp and the dopant density, the long expressions reduce to the expressions of the Shockley-Read-Hall model. We can write this expression with the use of the following identities:

$$\frac{n_0}{n_0 + n_1} = \frac{p_0}{p_0 + p_1} \tag{5.14}$$

And

$$p_1 n_1 = p_0 n_0 \tag{5.15}$$

$$g_e = \frac{\Delta n}{\tau_n} = \frac{\Delta p}{\tau_p} = \frac{\Delta n p_0 + \Delta p n_0 + \Delta n \Delta p}{\tau_{n0}(p_0 + p_1 + \Delta p) + \tau_{p0}(n_0 + n_1 + \Delta n)} \tag{5.16}$$

In the SRH model, *N* is small: the trapping of the carriers by the centers is negligible in comparison to the excess densities and we can consider $\Delta n = \Delta p$. We can now write the equation for the recombination lifetime $\tau_{SRH} = \tau_n = \tau_p$:

$$\tau_{SRH} = \frac{\tau_{n0}(p_0 + p_1 + \Delta n) + \tau_{p0}(n_0 + n_1 + \Delta n)}{n_0 + p_0 + \Delta n} \tag{5.17}$$

This equation reduces for p-type silicon to:

$$\tau_{SRH} = \frac{\tau_{n0}(N_A + p_1 + \Delta n) + \tau_{p0}(n_1 + \Delta n)}{N_A + \Delta n} \tag{5.18}$$

This equation shows that the SRH lifetime is in general function of the excess carrier concentration. This equation could also be simplified in the case of very low and high injection.

In the case of deep centers, n_1 and p_1 are much smaller than N_A and Δn, the expression becomes:

$$\tau_{SRH} = \tau_{n0}; \quad deep\ center, low-injection \tag{5.19}$$

$$\tau_{SRH} = \tau_{n0} + \tau_{p0}; \quad deep\ center, high-injection \tag{5.20}$$

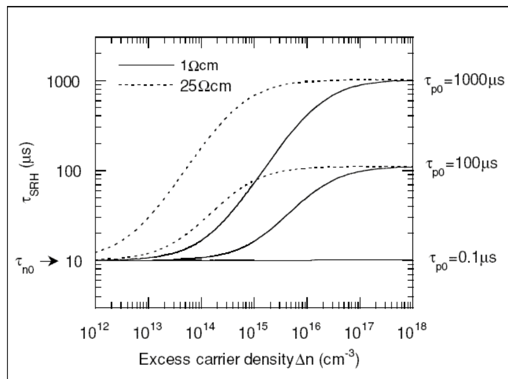

Figure 5-3: SRH recombination lifetimes for two different resistivities and different values of τ_{p0}

5.4 Surface recombination

Surface recombination is a special case of SRH recombination in which the localized states occur at the surface. These states, unlike bulk SRH centers, do not usually occupy a single energy level but form a set of states distributed across the band-gap. Analysis of the surface recombination is made in terms of *surface recombination velocity*.

In the simpler case, we can consider a sample with a constant bulk lifetime, τ_b, and a small constant SRV. The effective lifetime is:

$$\frac{1}{\tau_{eff}} = \frac{1}{\tau_b} + \frac{2S}{W} \tag{5.21}$$

In the extreme case of infinite surface recombination velocity, the effective lifetime will be dominated by the transit time of carriers to the surfaces, provided the bulk lifetime is not very small. Under steady state conditions, the effective lifetime in this case is given by:

$$\frac{1}{\tau_{eff}} = \frac{1}{\tau_b} + \frac{12D}{W^2} \tag{5.22}$$

D is the carrier diffusivity. In low injection conditions should be used the value D for the minority carriers while in high injection conditions an ambipolar diffusivity is more appropriate. This equation is used to estimate bulk lifetimes in samples with very high surface recombination velocities and low bulk lifetimes. In the transient decay mode, we have this equation:

$$\frac{1}{\tau_{eff}} = \frac{1}{\tau_b} + \frac{\pi^2 D}{W^2} \tag{5.23}$$

This amounts to a 22% higher effective lifetime measured in decay mode for a sample with a long bulk lifetime. For low bulk lifetime the difference is reduced.

5.5 Emitter recombination

Recombination within the heavily doped emitter region is another import source of carrier loss in silicon solar cells. Essentially, the high recombination rate in this region is due to Auger processes. It is possible to characterize total emitter recombination in terms of a single parameter: the emitter saturation current density, J_{0e}. This parameter contains recombination at the emitter surface as well as within the emitter bulk.

The effective recombination lifetime due to the emitter can be written as:

$$\tau_{emitter} = \frac{qn_1^2 W}{J_{0e}(N_A + \Delta n)} \tag{5.24}$$

In conditions of low injection, the lifetime is injection-level independent but in high-injection conditions, it decreases linearly with excess carrier density. Values for J_{0e} vary depending on the diffusion profile and the passivation quality.

5.6 Effective lifetime

For independent processes, the net recombination rate is the sum of all the single contributes, resulting in an effective lifetime τ_{eff}:

$$\frac{1}{\tau_{eff}} = \frac{1}{\tau_{SRH}} + \frac{1}{\tau_{Auger}} + \frac{1}{\tau_{emitter}} \tag{5.25}$$

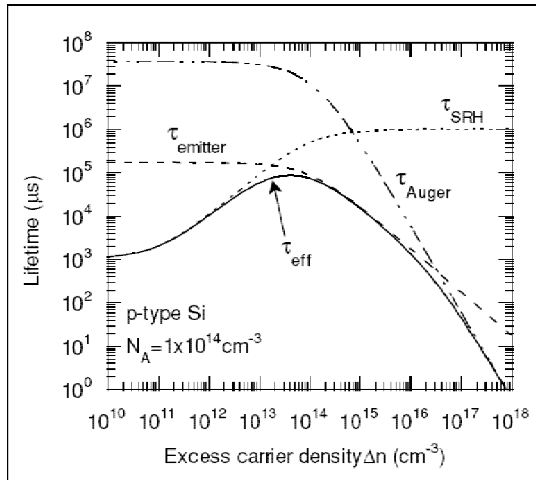

Figure 5-4: Lifetime in function of excess carrier density for a substrate with $N_A = 1 \times 10^{14}\ \mathrm{cm}^{-3}$ and a deep SRH center with $\tau_{n0} = 1\ \mathrm{ms}$ and $\tau_{po} = 1\ s$

In low injection, the sample is dominated by SRH recombination, at highest injection levels Auger recombination is the most important process.

6 Surface passivation

In order to minimize surface recombination, thin films of dielectric materials are used on crystalline solar cells as passivating layers. Surface passivation can be achieved mainly in two ways:

- reducing the recombination of charge carriers at the interface (chemical passivation)
- electrostatically, shielding the charge carriers from the interface by an internal electric field (field-effect passivation)

6.1 Chemical passivation

The chemical passivation mechanism reduces the surface recombination of charge carriers

reducing the interface defect density.

We can write the equation for the surface recombination rate:[7]

$$U_S = \left(n_S p_S - n_i^2\right) = \int_{E_V}^{E_C} \frac{\nu_{th} D_{it}(E_t) dE_t}{[n_S + n_1(E_T)]\sigma_p^{-1}(E_T) + [p_S + p_1(E_T)]\sigma_n^{-1}(E_T)} \tag{6.1}$$

where:

U_S= surface recombination rate per unit area

n_S= electron density per unit volume at the cell surface

p_S= hole density per unit volume at the cell surface

n_i= intrinsic charge carrier density

σ_n= capture cross section of electron

σ_p= capture cross section of hole

ν_{th}= thermal velocity of charge

E_T= Defect energy carrier level

D_{it}= Interface defect concentration

$n_1 - p_1$= SRH electron and hole density

From equation (6.1) we can see that the surface recombination rate is directly proportional to the Dit: a lower Dit value results in fact in a lower SRV.

The recombination is mainly due to the presence of dangling bonds and impurities at the surface. One way to reduce the recombination and thus lower the recombination velocity is by chemically saturating these dangling bonds with the application of a passivation layer (dielectric layer as Al2O3). Elements such hydrogen and oxygen atoms that are present in the passivation layer bind with the dangling bonds in order to make these trapping centers electrically inactive: lifetime of charge carriers will increase. Chemical passivation has the advantages that it is simple and low cost to apply and can be performed at room temperature.

6.2 Field effect passivation

Passivation can also be achieved electrostatically, shielding the charge carriers from the interface by an internal electric field. Due to the inclusion of additional charges into the semiconducting material, the minority charge carriers can be repelled from the cell surface to avoid recombination. This is called field effect passivation.

The first experimental attempts to reduce surface recombination losses in solar cells by means of the field effect passivation method were performed in the late 70s by Schartz et al.

Field effect passivation can be achieved in two ways:

- Passivation through diffused surface

Through the additional doping of donor and acceptor atoms in the semiconductor, an additional electric field such as n+/p+ or n-/p- layer is formed near the cell surface and that repeals the minority charge carriers

- Passivation through fixed charges in the dielectric layer

Some passivation materials contain fixed positive or negative charges in the dielectric layers. These charges influence the movement of charge carriers. When a dielectric material containing negative charges such as Al2O3 is applied to p-type silicon, the high negative charge density in the passivation layer acts as a shield and causes the repulsion of minority charge carriers, reducing the rate of charge carrier recombination at the interface. This results in a lower surface recombination velocity, SRV.

At the same way, when a dielectric material containing inherent positive charges such a SiNx is applied to p-type silicon, the high positive charge density at the interface attracts minority charge carriers. This causes the formation of an inversion layer at the interface between p-type silicon and the dielectric layers. We have a depletion of majority charge carriers, in this case holes, at the active recombination sites. Recombination rate at the surface is reduced.

6.3 A short review of surface passivation materials

Three of the most important surface passivation materials used for photovoltaic technologies are silicon dioxide, SiO2, hydrogenated amorphous silicon nitride, a-SiNx:H, and hydrogenated amorphous Si, a-Si:H.

- Silicon dioxide,SiO2

The high quality of interface between thermally grown SiO2 and Si is responsible for high solar cell efficiencies . [8]Silicon thermal oxide layers allow for a surface recombination velocity of below 10 cm/s on p-type surfaces .[9] The passivation mechanism of these films is based on chemical passivation and that leads to a low interface trap density at the Si/SiO2 interface ($D_{it} \approx$

$10^{10} \text{cm}^{-2} \cdot \text{eV}^{-1}$). Typical values for the positive fixed charge density are in the range of $1 \text{ to } 5 \times 10^{11} \text{ cm}^{-2}$ [9].This high level of chemical passivation can be achieved for both n- and p-type surfaces. Forming gas annealing for example introduces hydrogen that passivates the electronically active defects such as Pb-type defect that is a Si-dangling bond [2].

- Hydrogenated amorphous silicon nitride, a-SiNx:H

The optical properties of this material can be varied in a wide range; SiNx is in fact the standard material for antireflection coatings in solar cells. Films containing nitrogen exhibit refractive indices around 2: for this reason they are applied at the front of a solar cell. In addiction SiNx releases hydrogen during firing und this plays an important role in the bulk passivation of multicrystalline Si [10]. The passivation mechanisms of a-SiNx:H films depends on the content of nitrogen. For example, when the nitrogen content is low, the high level of passivation is mainly due to chemical passivation. When the concentration of N is high, on the other hand, the films induce a significant amount of field effect passivation [2, 10].

- Hydrogenated amorphous Si, a-Si:H

The deposition of hydrogenated amorphous silicon (a-Si:H) is another way to obtain excellent passivation. In contrast to hydrogenated amorphous silicon nitride (a-SiNx: H), the amorphous silicon (a-Si: H) does not contain inherent positive charges in the dielectric layer. This avoids shunting at the rear surface and the recombination in the interface [11]. Limitation of the application of a-Si:H surface passivation films are parasitic absorption effects and the lack of thermal stability during firing [2].

7 Crystal lattices

In this section a short overview of crystallography is given, expecially Silicon crystal structure has been analyzed. Most of the equations of this section have been taken from the textbook *Solid State Physics, Ashcroft Neil W., Mermin N. David* [6].

An ideal crystal consists of the infinite repetition of identical units in space. This unit constitutes of a single atom or of many atoms or molecules [6]. One lattice is described through three fundamental vectors, $\boldsymbol{a}_1$,$\boldsymbol{a}_2$,$\boldsymbol{a}_3$ .The atomic arrangement looks the same when viewed from the point $\boldsymbol{r}$ and viewed from the point:

$$\boldsymbol{r}' = \boldsymbol{r} + u_1\boldsymbol{a}_1 + u_2\boldsymbol{a}_2 + u_3\boldsymbol{a}_3 \tag{7.1}$$

where u_1,$u_2$and u_3 are arbitrary integers.

The points $\boldsymbol{r'}$defined by equation (7.1) for all u_1,$u_2$and u_3 defines a lattice: a set of periodic array of points in space. A crystal structure is defined by this relation:

$$lattice + basis = crystal\ structure$$

A basis of atoms consists of identical copies of the same physical unit.

If any two points $\boldsymbol{r'}$and $\boldsymbol{r}$ from which the atomic arrangement looks the same always satisfy the equation (7.1) then lattice and translational vectors are called primitive [12].

The number of atoms in the basis is not always the same for every crystal: it could be one or more than one. The position of the center of an atom *j* of the basis relative to the associated lattice point is:

$$\boldsymbol{r_j} = x_j\boldsymbol{a}_1 + y_j\boldsymbol{a}_2 + z_j\boldsymbol{a}_3 \tag{7.2}$$

7.1 Primitive lattice cell

A primitive cell is a type of cell or unit cell whose volume is the minimum. The number of atoms in a primitive cell or primitive basis is always the same for a given crystal structure. There is always one lattice point per primitive cell.

The volume of a parallelepiped with axes $\boldsymbol{a_1}$,$\boldsymbol{a}_2$,$\boldsymbol{a_3}$is:

$$V_C = |\boldsymbol{a}_1 \cdot \boldsymbol{a}_2 \times \boldsymbol{a}_3| \tag{7.3}$$

The primitive basis is the basis associated with primitive cell. It doesn’t exist a basis which contains fewer atoms than a primitive cell [6, 12].

7.2 Types of lattice

A lattice in three dimensional crystals is defined by three vectors $\boldsymbol{a_1}$,$\boldsymbol{a_2}$,$\boldsymbol{a_3}$and three angles α,$\boldsymbol{\beta}$and $\boldsymbol{\gamma}$. There are an infinite number of possible crystals but a finite number of lattice types. The different types are called Bravais lattices. When a Bravais lattice is repeated it can fill the whole space. A three dimensional Bravais lattice consists of all points with position vectors $\boldsymbol{R}$ of this form:

$$\boldsymbol{R} = u_1\boldsymbol{a}_1 + u_2\boldsymbol{a}_2 + u_3\boldsymbol{a}_3 \tag{7.4}$$

In three dimensions we have five distinct Bravais lattices but in three dimensions there are fourteen that can be grouped in 7 lattice systems: triclinic, monoclinic, orthorhombic, trigonal, tetragonal, cubic and hexagonal [6].

There are three lattices in the cubic system: the *simple cubic* (SC) lattice, the *body-centered cubic* (BCC) and the *face-centered cubic* (FCC) lattice. The characteristic of these cubic lattices are summarized below:

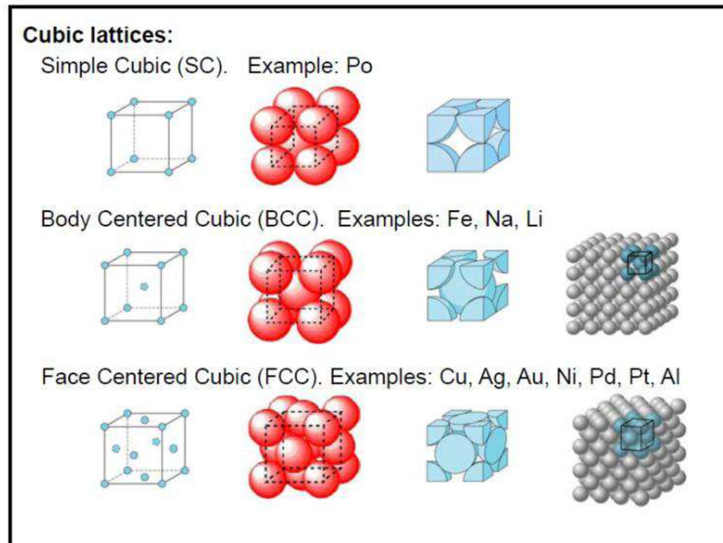

Figure 7-1: Three lattices in the cubic system: simple cubic (SC), body center cubic (BCC) and face centered cubic (FCC)

7.3 Coordination number

The points in a Bravais lattice that are closest to a given point are called nearest neighbors. Each point, because of the periodic nature of the Bravais lattice, has the same number of nearest neighbors. This number of nearest neighbors is called *coordination number of the lattice*. A simple cubic lattice has coordination number 6; a body center cubic lattice has coordination number 8; and a face-centered cubic lattice 12 [12].

7.4 Reciprocal lattice

The reciprocal lattice is the lattice in which the Fourier transform of the spatial wavefunction of the direct lattice is represented.

A reciprocal lattice is defined as the set of all wave vectors K that yields plane waves with the periodicity of a given Bravais lattice.

$\boldsymbol{K}$ belongs to the reciprocal lattice of a Bravais lattice of points $\boldsymbol{R}$;

the following expression holds for r and for all R in the Bravais lattice:

$$e^{i\boldsymbol{K}\cdot(\boldsymbol{r}+\boldsymbol{R})} = e^{i\boldsymbol{K}\cdot\boldsymbol{r}} \qquad (7.5)$$

The reciprocal lattice can be also represented as the set of wave vectors $\boldsymbol{K}$ satisfying this equation:

$$e^{i\boldsymbol{K}\cdot\boldsymbol{R}} = 1 \qquad (7.6)$$

for all $\boldsymbol{R}$ in the Bravais lattice.

The reciprocal lattice is a Bravais lattice. Consider $\boldsymbol{a}_1$, $\boldsymbol{a}_2$ and $\boldsymbol{a}_3$, a set of primitive vectors for the direct lattice. We can define three primitive vectros that can generate the reciprocal lattice:

$$\boldsymbol{b}_1 = 2\pi \frac{\boldsymbol{a}_2 \times \boldsymbol{a}_3}{\boldsymbol{a}_1 \cdot (\boldsymbol{a}_2 \times \boldsymbol{a}_3)}$$

$$\boldsymbol{b}_2 = 2\pi \frac{\boldsymbol{a}_3 \times \boldsymbol{a}_1}{\boldsymbol{a}_1 \cdot (\boldsymbol{a}_2 \times \boldsymbol{a}_3)} \qquad (7.7)$$

$$\boldsymbol{b}_3 = 2\pi \frac{\boldsymbol{a}_2 \times \boldsymbol{a}_3}{\boldsymbol{a}_1 \cdot (\boldsymbol{a}_2 \times \boldsymbol{a}_3)}$$

And $\boldsymbol{b}_i$ satisfy:

$$\boldsymbol{b}_i \cdot \boldsymbol{a}_j = 2\pi\delta_{ij} \tag{7.8}$$

Where δ_{ij} is the Kronecker delta symbol.

At this point any vector $\boldsymbol{k}$ can be written has a linear combination of the $\boldsymbol{b}_i$ as follows:

$$\boldsymbol{k} = k_1\boldsymbol{b}_1 + k_2\boldsymbol{b}_2 + k_3\boldsymbol{b}_3 \tag{7.9}$$

And if $\boldsymbol{R}$ is any direct lattice vector, then:

$$\boldsymbol{R} = u_1\boldsymbol{a}_1 + u_2\boldsymbol{a}_2 + u_3\boldsymbol{a}_3 \tag{7.10}$$

Where the u_1,$u_2$and u_3 are integers. It follows form the equation (7.8) that:

$$\boldsymbol{k} \cdot \boldsymbol{R} = 2\pi(k_1u_1 + k_2u_2 + k_3u_3) \tag{7.11}$$

[6, 12]

7.5 Lattice planes and Miller indices

A lattice plane is defined as any plane containing at least three noncollinear Bravais lattice points. A family of lattice planes is a set of parallel, equally spaced lattice planes, that contain all the points of the three dimensional Bravais lattice. Any family of lattice planes separated by a distance $\boldsymbol{d}$ is associate with reciprocal lattice vectors perpendicular to the planes, the shortest of which have a length of $2\pi/d$ [6].

The Miller indices of a lattice plane are the coordinates of the shortest reciprocal lattice vector normal to that plane, with respect to a specific set of primitive reciprocal lattice vectors. A plane with Miller indices *h*,*k*,*l*, is normal to the reciprocal lattice vector:

$$h\boldsymbol{b}_1 + k\boldsymbol{b}_2 + l\boldsymbol{b}_3 \tag{7.12}$$

Table 7-1: Miller indices: notation and interpretation

NOTATION	*INTERPRETATION*
(hkl)	Crystal plane
[hkl]	Crystal direction
{hkl}	Equivalent planes
$< hkl >$	Equivalent directions

Miller indices are used to specify directions and planes; these could be in lattices or in crystals and the number of indices will match with the dimension of the lattice of the crystal [6, 12].

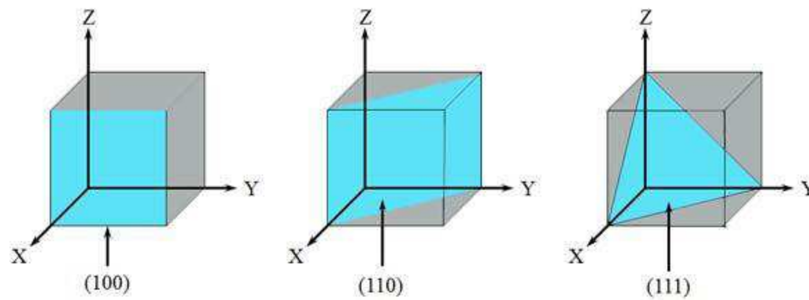

Figure 7-2: Silicon crystal planes

7.6 Silicon crystal structure

As far as the silicon crystal structure is concenrned, silicon crystallizes as diamond, the unit celli is cubic and each Si atom has 4 nearest neighbors. The lattice constant is 5.431 Å. 4 atoms are completely inside the cell and each of the 8 atoms on corner is shared among shells. Each of the 6 atoms on the faces is shared among 2 cells [6].

Diamond Structure

The diamond lattice consists of two interpenetrating face-centered cubic Bravais lattices. It can be considered as a face-centered cubic lattice with the two point basis $\mathbf{0}$ and $(a/4)(\hat{\boldsymbol{x}}+\hat{\boldsymbol{y}}+\hat{\boldsymbol{z}})$. The coordination number is 4. The diamond lattice is not a Bravais lattice because the environment of any point differs in orientation from the environment of its nearest neighbors. In table we can find elements crystallizing in the diamond structure:[6, 12]

Table 7-2: Cube side of carbon, silicon and germanium

$ELEMENT$	$CUBE\ SIDE\ a(\dot{A})$
C (diamond)	3.57
Si	5.43
Ge	5.66

7.6.1 Silicon wafer orientation

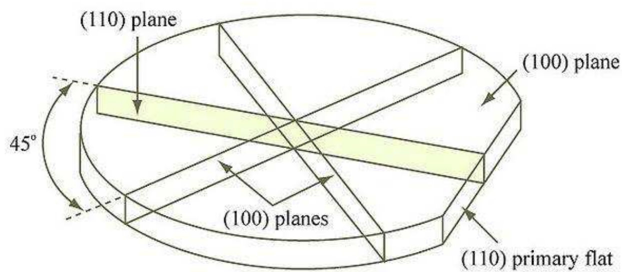

Figure 7-3: crystal orientation in FZ-Si wafers with SEMI M1 specification

Standard silicon wafers used in semiconductor manufacturing are extensively standardized by SEMI (Semiconductor Equipment and Material International). These standards stipulate most of the important parameters, like dimensions, dimensional tolerances, key measurement technique. In this work p-type FZ-Silicon wafers with SEMI M1 specification are used, with flat specification: [13]

$$< 100 > \ to \{110\}$$

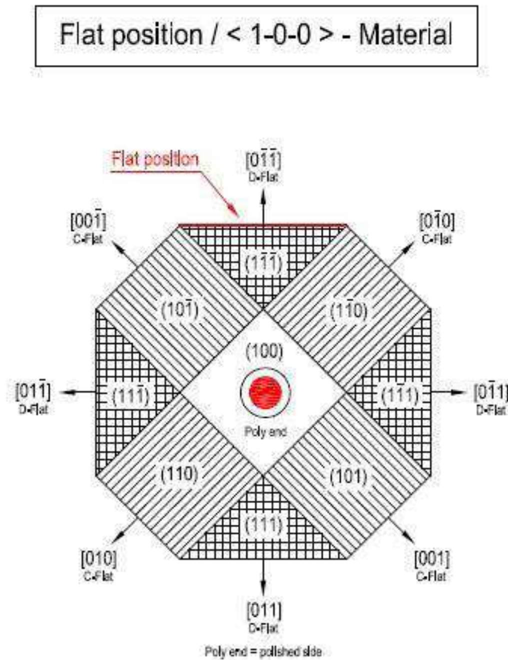

Figure 7-4: Image of the crystal orientation in FZ-Si wafers with SEMI M1 specification from the Siltronic AG corporation, Münche

8 Characterization techniques

8.1 Quasi-Steady State Photo Conductance (QSSPC)

In this work we used the QSSPC, "quasi-steady-state-photoconductance" technique to measure the lifetime of our samples. This technique was first suggested by Sinton and Cuevas in 1996 [14]. Measurements of minority carrier lifetimes in silicon are extremely important for process control and device optimization as well as material device research The QSSPC method monitors the decay of optically excessed charged carriers to their equilibrium conditions [14].

The QSSPC method is based on the principle of electromagnetic induction: a change in the sample conductivity is measured.

Suppose we have no traps in the bulk of the semiconductor $\Delta n = \Delta p$ the net excess conductance $\Delta\sigma$ is given by this equation:

$$\Delta\sigma = q\Delta n(\mu_n + \mu_p)W \tag{8.1}$$

.

Where *W* is the width of the sample and μ_n and μ_p are the mobilities of electrons and holes.

A flash lamp is used as generation source. There are three different ways to obtain lifetime measurements: it depends on the illumination time with the flash lamp.

When we have to measure low lifetime, Quasi-Static measurement is used and the sample is exposed to light for a significantly long time to obtain the lifetime value [15].

As seen is section 5, the relation between excess carrier density and carrier lifetime is obtain by the following equation:

$$\tau(\Delta n) = \frac{\Delta n(t)}{G} \tag{8.2}$$

G is the excess carrier generation rate after illumination and depends on the intensity of illumination, on the optical properties and material characteristic.

The Transient Measurements method is used to measure high values of sample lifetimes. The sample is illuminated for a short time and the generation rate G is neglected due to dark measurement. The lifetime in this case is expressed by the following expression:

$$\tau(\Delta n) = \frac{\Delta n}{\frac{d\left(\Delta n(t)\right)}{\Delta t}} \tag{8.3}$$

Nagel et al. proposed also another method, more accurate, to determine carrier lifetime. In this method, lifetime measurements are independent from the duration of the flash lamp [16].

$$\tau(\Delta n) = \frac{\Delta n}{G(t) - \frac{d\left(\Delta n(t)\right)}{\Delta t}} \tag{8.4}$$

In this method, a specific parameter, before the measurement, has to be known. This parameter is called the optical factor f_{abs} .

$$G = \frac{N_{ph} f_{abs}}{W} \tag{8.5}$$

where N_{ph} is the flux of photons and W is the thickness of the sample [17].

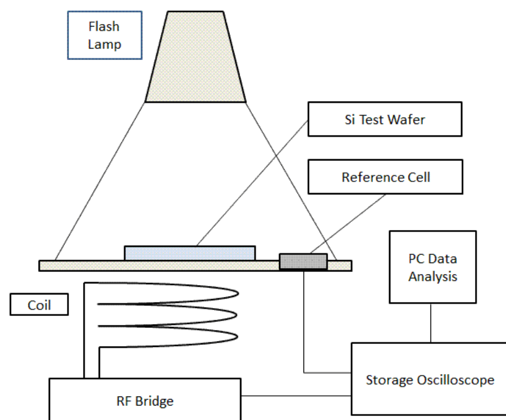

Figure 8-1: Schematic of the QSSPC working principle

8.2 Spectral ellipsometry

Spectral ellipsometry measurements are based on the principle that, when a linearly polarized beam of light is made incident on a surface, there is a change in the polarization of the light beam from the material surface.

Table 8-1: Features of spectral ellipsometry [18]

Measurement probe	Light
Measurement value	(Ψ, Δ)
Measurements region	Infrared-visible/ultraviolet region
Application area: semiconductor	Substrates, thin film, gate dielectrics, lithography films
Real-time monitoring	Chemical vapor deposition(CVD), molecular beam epitaxy(MBE), etching, oxidation, thermal annealing, liquid phase processing etc.
Restrictions	Surface roughness of samples has to be small Measurement has to be performed at oblique incidence

To measure the thickness of our sample we use a spectral Ellipsometer that works on the principle described above. Ellipsometry is also applied to characterize composition, roughness, doping concentration, and other material properties associated with a change in optical response.[18] The spectral Ellipsometer measures the two values, (Ψ, Δ): the amplitude ratio Ψ and phase difference Δ between light waves known as p- and s-polarized light waves. The change in light polarization after reflection can be measured using this expression (according to Fresnel equations):

$$\rho = \left(\frac{r_p}{r_s}\right) = \tan(\Psi)\, e^{i\Delta} \quad (8.6)$$

Where:

ρ is the complex reflectance ratio;

r_p is the component of the beam parallel to the angle of incidence (p-polarized waves)

r_s is the component of the beam perpendicular to the angle of incidence (s-polarized waves)

Ψ is the amplitude ratio

Δ is the phase difference between r_p and r_s after reflection

8.3 Electron paramagnetic resonance (EPR)

Electron Paramagnetic Resonance is an analytical tool that can provide chemical and structural information about trapping centers. In addition, it can also provide measurements of the density of these centers. Most trapping centers will capture a single electron or a single hole: with the capture of either an electron or a hole an initially diamagnetic center will be rendered paramagnetic and it will turn to be EPR active. and a Also an initially paramagnetic center can be rendered diamagnetic and thus EPR inactive with the capture of either an electron or a hole. EPR can identify the response of a defect to charge carriers, measure its density, and identify its chemical and structural nature.

9 EPR: theoretical aspects

9.1 Historical overview

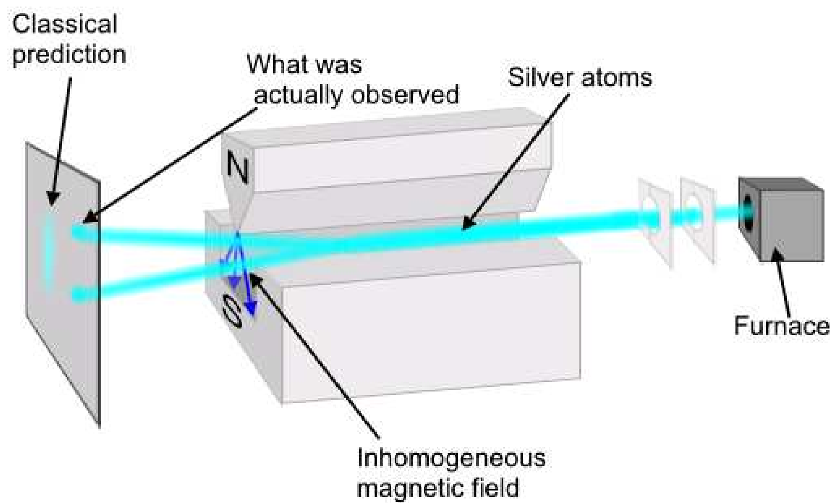

Figure 9-1: Scheme oft he Stern-Gerlach apparatus

The technique of electron paramagnetic resonance spectroscopy may be seen as an extension of the Stern-Gerlach experiment.

This experiment in the 1922 discovered a new aspect of nature and at the same time found the simplest quantum system in existence. In the Stern-Gerlach experiment a beam of hot atoms (silver) is passed through a non uniform magnetic field. This field would interact with the magnetic dipole moment of the atom and deflect it.

The quantum mechanics predictions are that μ_{lz}, the orbital magnetic dipole moment in the z direction, can have only the quantized values:

$$\mu_{lz} = -g_l \mu_B m_l \tag{9.1}$$

.

where:

μ_B= Bohr magneton

g_l= orbital g-factor

m_l= magnetic dipole moment

and

$$m_l = -l, -l+1, \ldots, 0 \ldots, +l-1, +l \tag{9.2}$$

Thus, the quantum mechanical prediction is that the deflected beam would be spread in discrete components. As far as the classical predictions are concerned, a continuous distribution of values of μ_{lz} would be expected and thus the beam would be spread in a continuous band.

Stern and Gerlach found out that the beam of silver atoms is split into two discrete components: one component was bent in the positive z direction and the other in the negative z direction. They showed also that this result was independent of the choice of the negative z direction.

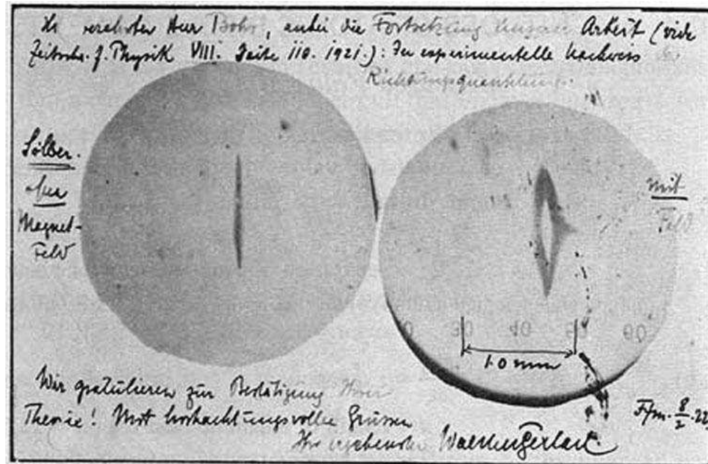

Figure 9-2: The actual images taken from the post card Gerlach sent to Bohr announcing his results (February 1922). It shows a photograph of the beam splitting

This experiment discovered that the atoms, specifically the unpaired outer electron, did have a magnetic dipole moment. In effect, in addition to being charged, electrons acted like bar magnets. An electron has in fact an intrinsic magnetic dipole moment μ_s, due to the fact that it has an intrinsic angular momentum *S* called spin. The magnitude S and the z component of the spin angular momentum are related to two quantum number, s and m_s , by quantisation relations which are identical to those for orbital angular momentum:

$$S = \sqrt{s(s+1)}\hbar \tag{9.3}$$

$$S_Z = m_s\hbar \tag{9.4}$$

$$\boldsymbol{\mu_s} = -\frac{g_s\mu_B}{\hbar}\boldsymbol{S} \tag{9.5}$$

$$\mu_{sz} = -g_s \mu_B m_s \tag{9.6}$$

The quantity g_s is called the *spin g factor*. From the experimental observation that the beam of hydrogen atoms is split into two symmetrically deflected components, it is apparent that μ_{sz} can assume just two values, which are equal in magnitude but opposite in sign. The possible values of m_s differ by one and range from –s and +s:

$$m_s = -\frac{1}{2}, +\frac{1}{2} \tag{9.7}$$

And that s has the single value

$$s = 1/2$$

By measuring the splitting of the beam of hydrogen atoms, it is possible to evaluate the net force F_z they feel while traversing the magnetic field:

$$F_z = -\left(\frac{\partial B_Z}{\partial z}\right) g_s \mu_B m_s \tag{9.8}$$

Since μ_B is known and $\frac{\partial B_Z}{\partial z}$ can be measured the experiments determine the value of the quantity $g_s m_s$ and it was found that:

$g_s m_s = \pm 1$. This implies:

$$g_s = 2$$

These conclusions are confirmed by many different experiments.

The splitting of energy levels of an atom when it is placed in an external magnetic field is called the ***Zeeman effect.*** The splitting occurs because of the interaction of the magnetic moment of the atom with the magnetic field B slightly shifts the energy of the magnetic levels. This splitting corresponds of the two possible values of the orientational potential energy:

$$\Delta E = -\boldsymbol{\mu_s} \cdot \boldsymbol{B} = -\mu_{sz} \cdot B = g_s \mu_B m_s B = \pm \frac{g_s \mu_B B}{2} \qquad (9.9)$$

where the z axis is taken into the direction of the applied field. This energy shift depends on the relative orientation of the magnetic moment and the magnetic field. Electron spin resonance depends on the Zeeman splitting of a single energy level within the atom.

The first observation of an electron paramagnetic resonance peak was made in 1945 when Zavoisky's results were interpreted by Frenkel as paramagnetic resonance absorption. Other experiments were undertaken at higher microwave frequencies in magnetic field of 100-300 mT: it was showed the advantage of use of high frequencies and field. After the World War 2 equipment for the 9-GHz region had been extensively used for radar. Also in the United States and in England studies were made in this field. Theorists such as Abgram, Bleaney, Pryce and Van Vleck contributed in the interpretation of the EPR spectra. In the 1980s, the equipment became cheaper and the first commercial pulse EPR was released to the market. Ten years later, the first commecial high field spectrometer was released [20-22].

9.2 Orbital magnetic dipole and Larmor precession

An electron of mass *m* and charge –*e* that moves with velocity of magnitude *v* in a circular orbit of radius *r*, produces a current of magnitude:

$$i = \frac{e}{T} = \frac{ev}{2\pi r} \tag{9.10}$$

T= orbital period of the electron whose charge has magnitude *e*.

This loop produces a magnetic field orientated perpendicular to its plane. If we consider a current I circulating is a loop of area A, the magnitude of the orbital magnetic dipole moment μ_l of the equivalent dipole is:

$$\mu_l = iA \tag{9.11}$$

Electrons are negative charged: for that reason its magnetic moment μ_l is antiparallel to its orbital quantum momentum *L*:

$$L = mvr \tag{9.12}$$

Combining these two first expressions and evaluating *i* from the first equation, we obtain:

$$\mu_l = iA = \frac{evr}{2}$$ (9.13)

And we can obtain

$$\frac{\mu_l}{L} = \frac{evr}{2mvr} = \frac{e}{2m}$$ (9.14)

This ration can be written as:

$$\frac{\mu_l}{L} = \frac{g\mu_B}{\hbar}$$ (9.15)

where

$$\mu_B = \frac{e\hbar}{2m} = 0.927 \times 10^{-23}\ \mathrm{amp} - \mathrm{m}^2$$

is called the *Bohr magneton*.

The quantity *g* is called *the orbital g factor*.

Equation (8.15) can be written also as a vector equation:

$$\boldsymbol{\mu_l} = -\frac{g\mu_B}{\hbar}\boldsymbol{L}$$ (9.16)

Because the ratio μ_l/L does not depend on the size of the orbit or on the orbital frequency this equation can also be rewritten in this way:

$$\boldsymbol{\mu_l} = \frac{g\mu_B}{\hbar}L = \frac{g\mu_B}{\hbar}\sqrt{l(l+1)}\hbar = g\mu_B\sqrt{l(l+1)}$$

(9.17)

(using the quantum mechanical expression: $L = \sqrt{l(l+1)}\hbar$)

And:

$$\mu_{lz} = -\frac{g\mu_B}{\hbar}L_z = -g\mu_B m_l$$

(9.18)

If we consider the behavior of a magnetic dipole of moment μ_l placed in an external magnetic field B, it will experience a torque:

$$\boldsymbol{\tau} = \boldsymbol{\mu_l} \times \boldsymbol{B}$$

(9.19)

This torque tends to align the dipole to the field. There is also a potential energy associated to this torque:

$$\Delta E = -\boldsymbol{\mu_l} \cdot \boldsymbol{B}$$

(9.20)

The orientational potential energy ΔE of the system must remain constant if there are not possibilities for the system to dissipate energy. In this situation $\boldsymbol{\mu_l}$ cannot align itself with B. The magnetic dipole moment will precess around B but the angle between these two vectors must remain constant such as the magnitude of both vectors.

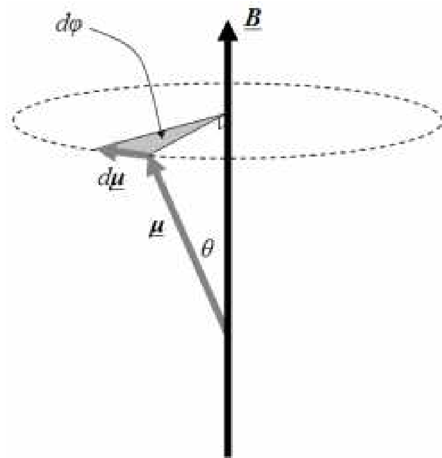

Figure 9-3: The magnetic dipole moment precesses around the magnetic field B

We can write at this point the angular frequency of precession of μ_l about *B*:

$$\boldsymbol{\omega} = \frac{g\mu_B}{\hbar}\boldsymbol{B} \tag{9.21}$$

This equation shows the phenomenon called *Larmor precession*: the sense of the precession is in the direction of **B** [19, 20].

The phenomenon of electron spin resonance spectroscopy can be explained by considering the behavior of a free electron. According to quantum theory the electron has a spin which can be understood as an angular momentum leading to a magnetic moment.

Consequently, the negative charge that the electron carries is also spinning and constitutes a circulating electric current. The circulating current induces a magnetic moment which, if the electron is subjected to a steady magnetic field, $H_0||z$, causes the electron to experience a torque tending to align the magnetic moment with the field. As seen in the section 8.1, the relation between the magnetic moment and the spin vector is:

$$\mu_s = -g\mu_B S/\hbar$$

where $\mu_B = eh/4\pi m_e$ is the Bohr magneton and $g = 2.002319$ is the Lande' factor. The energy of the system depends on the projection of the spin vector along the field H_0.Only two values are permitted for an electron

$$S_Z = \pm\frac{\hbar}{2}$$

which means that the electron magnetic moment can only assume two projections on the applied field as shown in Figure.

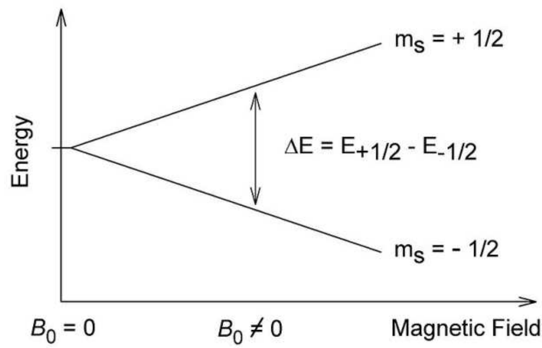

Figure 9-4: Energy level scheme for the simplest system, the free electron as a function of the applied magnetic field B, showing EPR absorption

$$\mu_Z = \pm\frac{g\mu_B}{2} \quad (9.22)$$

and the two values of the energy levels are:

$$E_\pm = \frac{g\mu_B}{2}H_0 \quad (9.23)$$

Magnetic resonance occurs when the energy difference between the two electron orientations is equal to Planck's constant,h, times the microwave frequency. For the case of an isolated electron, the resonance requirement may be expressed as:

$$\Delta E = E_{+} - E_{-} = h\nu = g\mu_B H \tag{9.24}$$

This expression describes the resonance condition for a single electron that is not supposed to interact with its surroundings.

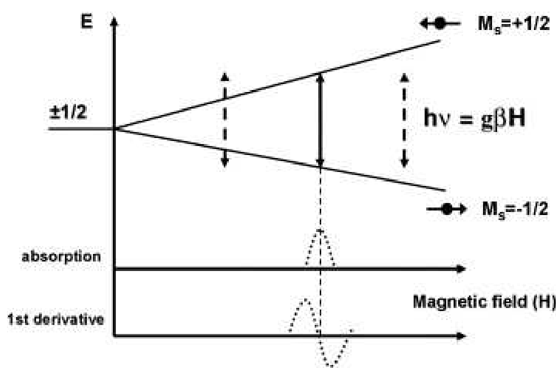

Figure 9-5: The absorption peak corresponds to the resonance condition for a single electron that not interacts with the surroundings

For electrons bound into an atom or into a molecule, the phenomenon of EPR may not be observed at all, because electron spins pair off in atomic or molecular orbitals so that no net spin magnetism is exhibited and the material is said to be ***diamagnetic***.

When an atom or a molecule has an odd number of electrons, however, complete pairing is not possible and the material is said to be ***paramagnetic***. In that case EPR signal can be observed.

In EPR measurements, the sample under study is exposed to a large slowly varying magnetic field and a microwave frequency (300 GHz – 300 MHz) magnetic field oriented perpendicular to the applied field. Usually the measurements are made at the *X* band: that corresponds to a microwave frequency of $\nu = 9.5\ GHz$.

At the resonance condition the microwave energy allows the transition between the two electron energy levels and thus the inversion of the spin orientation with respect to the direction of the applied magnetic field.

EPR samples consist of collections of many paramagnetic species, and not single isolated paramagnetic centers.

If the population of radicals is in thermodynamic equilibrium, its statistical distribution is described by the Maxwell-Boltzmann equation:

$$\frac{n_{upper}}{n_{lower}} = \exp\left(\frac{-E_{upper} - E_{lower}}{KT}\right) = \exp\left(-\frac{\Delta E}{KT}\right) = \exp\left(-\frac{h\nu}{KT}\right) \tag{9.25}$$

where n_{upper} is the number of paramagnetic centers occupying the upper energy state, n_{lower} is the number of paramagnetic centers occupying the lower energy state, *K* is the Boltzmann constant, and *T* is the temperature in Kelvins. At 298 K, X-band microwave frequencies (9.75 GHz) give

$$\frac{n_{upper}}{n_{lower}} = 0.998$$

That means that the upper energy level has a smaller population than the lower one. Therefore, transitions from the lower to the higher level are more probable than the reverse, which is why there is a net *absorption of energy*.

DEVIATION:

The structural information provided by EPR is due to some deviation from this expression. The most important deviations are due to *spin-orbit coupling* and *electron-nuclear hyperfine interaction* [21].

9.3 Spin-orbit interaction

In a one-electron atom, if we consider the motion of the nucleus from the point of view of the electron, the origin of the magnetic field experienced by the electron can be easily understood. In a frame of reference fixed on the electron, the charged nucleus moves around the electron and the electron is placed in a current loop which produces a magnetic field.

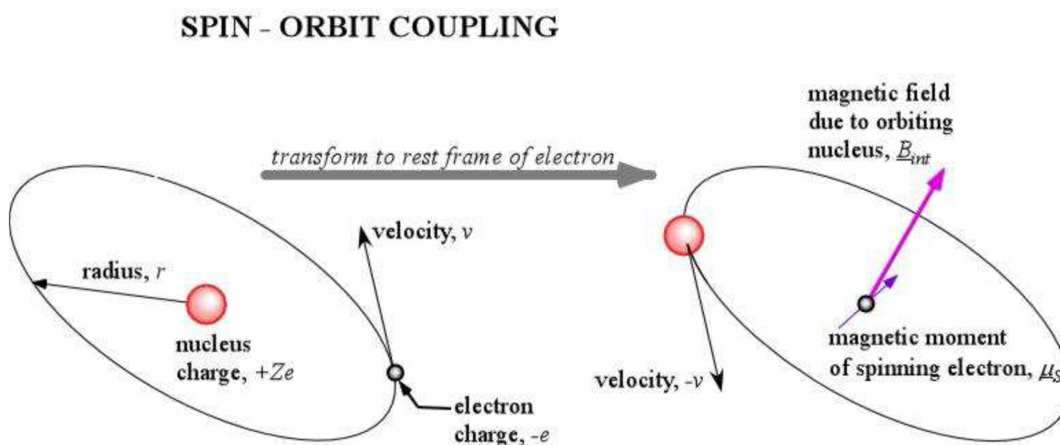

Figure 9-6: Spin-orbit coupling in the rest frame of the nucleus and of the electron

The charge nucleus moving with velocity $-\boldsymbol{v}$ constitutes a current element $\boldsymbol{j} = -Ze\boldsymbol{v}$

According to the Ampere's law, this produces a magnetic field B:

$$B = \frac{\mu_0}{4\pi}\frac{\boldsymbol{j}\times\boldsymbol{r}}{r^3} = \frac{Ze\mu_0}{4\pi}\frac{v\times r}{r^3} \tag{9.26}$$

at the position of the electron.

According to Coulomb's law we can also express this expression in terms of the electric field E:

$$E = \frac{Ze}{4\pi\varepsilon_0}\frac{\boldsymbol{r}}{r^3} \tag{9.27}$$

And from this last equation we have:

$$B = -\varepsilon_0\mu_0\boldsymbol{v}\times\boldsymbol{E} \tag{9.28}$$

Or:

$$B = -\frac{1}{c^2}\boldsymbol{v}\times\boldsymbol{E} \tag{9.29}$$

where $c = 1/\sqrt{\varepsilon_0}\mu_0$.

The quantity B is the magnetic field experienced by the electron when it is moving relative to the nucleus.

The orientational potential energy of the magnetic dipole moment in this magnetic field is:

$$\Delta E = -\boldsymbol{\mu_S} \cdot \boldsymbol{B} \tag{9.30}$$

Or, in terms of the electron spin angular momentum S:

$$\Delta E = \frac{g_s \mu_B}{\hbar} \boldsymbol{S} \cdot \boldsymbol{B} \tag{9.31}$$

These equations are valid in a frame of reference in which the electron is at rest. For the evaluation of the energy in the normal frame of reference (in which the nucleus is at rest) relativistic transformation of velocities has to be taken into account.

The spin-orbit energy is:

$$\Delta E = \frac{g_s \mu_B}{2\hbar} \boldsymbol{S} \cdot \boldsymbol{B} \tag{9.32}$$

The spin-orbit coupling may thus be included in the EPR resonance condition by replacing the constant g_s with a symmetric rank tensor g_{ij}. The symmetry of this tensor reflects the symmetry of the paramagnetic center. Perturbation theory allows calculation of the g tensor for simple defects. The components of the g tensor are given by:

$$g_{ij} = g_0 \delta_{ij} - 2\lambda \sum_k \frac{< \alpha|L_i|k >< k|L_j|\alpha >}{E_k - E_\alpha} \tag{9.33}$$

Here g_0 is the free electron value, λ the atomic spin-orbit coupling constant, $L_i$and L_j are angular momentum operators appropriate for the x,y or z directions and the summation is over all excited states k. State $\alpha$and energy E_α correspond to the paramagnetic ground state of the system [19, 20].

9.4 Electron-nuclear hyperfine interaction

The hyperfine interaction of the unpaired electron with the nuclei is another source of deviation from this expression:

$$h\nu = g_0 \mu_B B \tag{9.34}$$

A hyperfine splitting of the energy levels can be observed for many atoms. It is smaller than the spin-orbit splitting by three orders of magnitude. Hyperfine splitting can be due to the interaction between an intrinsic magnetic dipole moment of the nucleus and a magnetic field produced by the atomic electrons, and/or to the interaction between a nonspherically symmetrical nuclear charge distribution and a nonspherically symmetrical electric field produce by the atomic electrons. These effects can provide useful information about the nucleus .

In metal/insulator/silicon systems we can report the most significant magnetic nuclei:
Si(spin 1/2), H(spin 1/2), P(spin 1/2) and N (spin 1). A spin ½ has two possible orientations in the applied field and a spin 1 nucleus three possible orientations.
We can consider the nuclear moment interacting with an unpaired electron whose wave function is a linear combination of atomic orbitals (LCAO, linear combination of atomic orbitals). The wave functions of molecular orbitals can be approximated by taking linear combinations of atomic orbit-als.
The LCAO for an unpaired electron can be written as:

$$|\alpha> = \sum_n a_n \{c_s|s> + c_p|p>\} \tag{9.35}$$

Where s and p represent the atomic orbitals corresponding to the *n*th site,

a_n^2 is the localization on the *n*th site,

c_s^2 and c_p^2 represent the amount of s and p character of the wave function on the *n*th atomic site.

To first order we can consider $a_n^2 \cong 1$ because the unpaired electron can be considered well localized at a single nuclear site. To first order then we can interpret EPR spectra in term of s/p hybridized atomic orbitals localized at a central site.

The electron nuclear interaction of an electron in a p orbital is anisotropic:

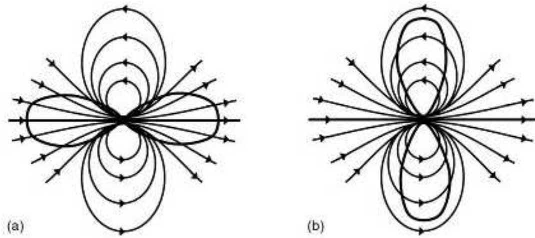

Figure 9-7: Schematic illustration of an electron in a p orbital interacting with a magnetic nucleus. a) In the first case the nuclear moment is parallel to the symmetry axis. b) In the second case the nuclear moment is perpendicular to the symmetry axis

The interaction is strongest when the field is parallel to the symmetry axis. When the field is perpendicular to the symmetry axis the sign of the interaction changes and the magnitude is decrease. The electron-nuclear hyperfine interaction is isotropic in a s orbital:

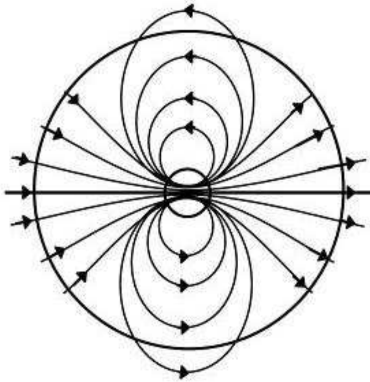

Figure 9-8: Diagram of the isotropic interaction of an s orbital electron with a magnetic nucleus

Because of the spherical symmetry of the orbital the interaction with this field is zero; the interaction is not zero only in a spherical region about the nucleus (with a radius of an imaginary current loop generating the nuclear moment's field). When the s orbital has a probability density at the nucleus that differs from zero we have a large isotropic interaction. For the s orbital hyperfine interaction we can consider the magnetic field at the center of a current loop of radius a:

$$\frac{2\mu}{a^3} \tag{9.36}$$

according to the Biot-Savart law, where a is the radius of the current loop and μ is the magnetic moment of the current loop. We can consider the probability density of the electron to be constant because it doesn't vary much over the volume of the nucleus.

At this point we can write the isotropic interaction

$$A(isotropic) = \left(\frac{4}{3}\pi a^3 |\alpha(0)|^2\right)\left(\frac{2\mu}{a^3}\right) \tag{9.37}$$

We have considered only the fraction of the electron wave function at the nucleus:

$$\frac{4}{3}\pi a^3|\alpha(0)|^2 \tag{9.38}$$

The magnetic moment of the nucleus is the nuclear *g* factor, g_n, times the nuclear Bohr magneton, μ_{Bn}. The isotropic or Fermi contact interaction can be rewritten as:

$$A(isotropic) = \left(\frac{8}{3}\pi\ g_n\mu_{Bn}|\alpha(0)|^2\right) \tag{9.39}$$

The hyperfine interaction is expressed in terms of a second rank tensor. In good approximation, the wave functions of the paramagnetic centers in Silicon thin films are axially symmetric and thus an axially symmetric tensor is appropriate. The component of the hyperfine tensor correspond to sums of the isotropic and anisotropic interactions for the applied field parallel and perpendicular to the unpaired electron's orbital symmetry axis:

$$A_{\parallel} = A_{iso} + 2A_{aniso};$$

$$A_{\perp} = A_{iso} - A_{aniso} \tag{9.40}$$

If we consider a paramagnetic center with a specific orientation the resonance condition is:

$$H = H_0 + M_1 A \tag{9.41}$$

$$H = H_0 + M_1 A$$

Where

$$H_0 = \frac{h\nu}{g\mu_B}$$

And M_1 is the nuclear spin quantum number.

$$g = g_{\parallel}^2 \cos\theta^2 + g_{\perp}^2 \sin\theta^2 \quad (9.42)$$

And

$$A = (A_{\parallel}^2 \cos\theta^2 + A_{\perp}^2 \sin\theta^2) \quad (9.43)$$

These equations are a very reliable basis for analyzing EPR results for defects with a specific orientation with respect to the applied magnetic field. The evaluation of EPR hyperfine tensor allows a reliable identification of the wave function of unpaired electrons [19, 20].

9.5 g-factor

An unpaired electron responds not only to a spectrometer's applied magnetic field B but also to any local magnetic fields of atoms or molecules:

$$\mathbf{B}_{\mathrm{eff}} = \mathbf{B} + \mathbf{B}_{\mathrm{local}} \quad (9.44)$$

Where

$$\mathbf{B}_{\text{eff}} = (1 - \sigma)\mathbf{B}$$

(9.45)

σ includes effect of local fields (positive or negative).

At this point we can rewrite equation (9.34)

$$h\nu = g_0 \mu_B (1 - \sigma) B$$

(9.46)

and the quantity:

$$g = g_0(1 - \sigma)$$

(9.47)

is given as g-factor.

In many free radicals and some transition ions the g factor determined from EPR experiment is equal to g_0. There are also many systems that show deviations from this value. That tells us that the ratio of spin magnetic moment to angular moment could be different than free electron. Thus the electron must have gained or lost angular momentum through spin-orbit coupling.

The magnitude of the change gives information about the nature of the atomic or molecular orbital containing the unpaired electron.

The anisotropy of the g factor is related to the symmetry of the electronic orbital of the unpaired electron under study. The origin of g anisotropy is the spin-orbit coupling (seen in section 9.3).

An isotropic g factor corresponds to a symmetric environment such as cubic, octahedral and tetrahedral symmetry: g is a scalar. As far as the anisotropic g factor is concerned, the system has an axial symmetry or rotational. The g factor consists of a matrix/tensor. Choosing an appropriate coordinate system (x,y,z for example) we can "diagonalize" this tensor, reducing the maximum number of its components from nine to three

$$\begin{matrix} g_x & 0 & 0 \\ 0 & g_y & 0 \\ 0 & 0 & g_z \end{matrix}$$

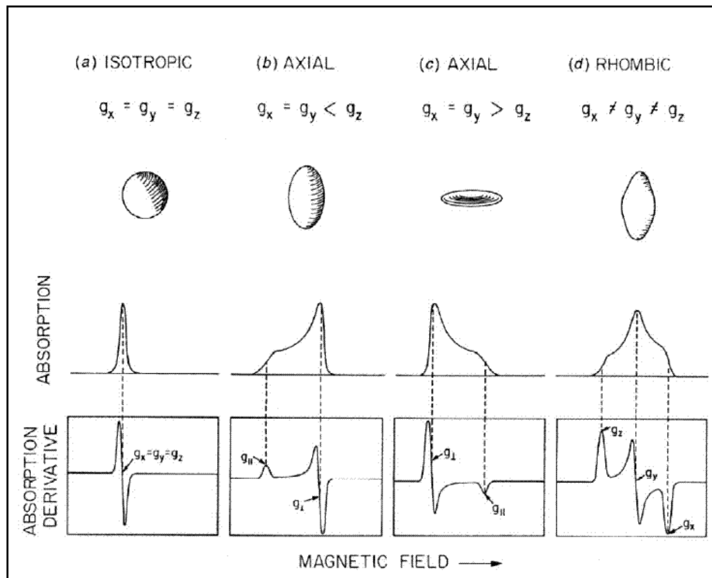

Figure 9-9: absorption and first-derivative spectra for three different classes of anisotropy. In the first class, called **isotropic**, all of the principal g factors are the same. In the second class, called axial, there is a unique axis that differs from the other two ($g_x = g_y \neq g_z$). The g factor along the unique axis is said to be parallel with it, $g_z = g_{\parallel}$ while the remaining two axes are perpendicular to it, $g_z = g_{\perp}$. The last class, called **rhombic**, occurs when all the g factors differ [21].

10 EPR spectrometer

An EPR spectrometer consists of four essential components:

1) A monochromatic microwave source

2) A waveguide for guiding the microwave power to the sample

3) A cavity designed to ensure a proper coupling between the sample and the incoming wave

4) A detector for microwave power to detect the response of the sample to microwave irradiation

A schematic drawing of the EPR spectrometer is shown in Figure 10-1:

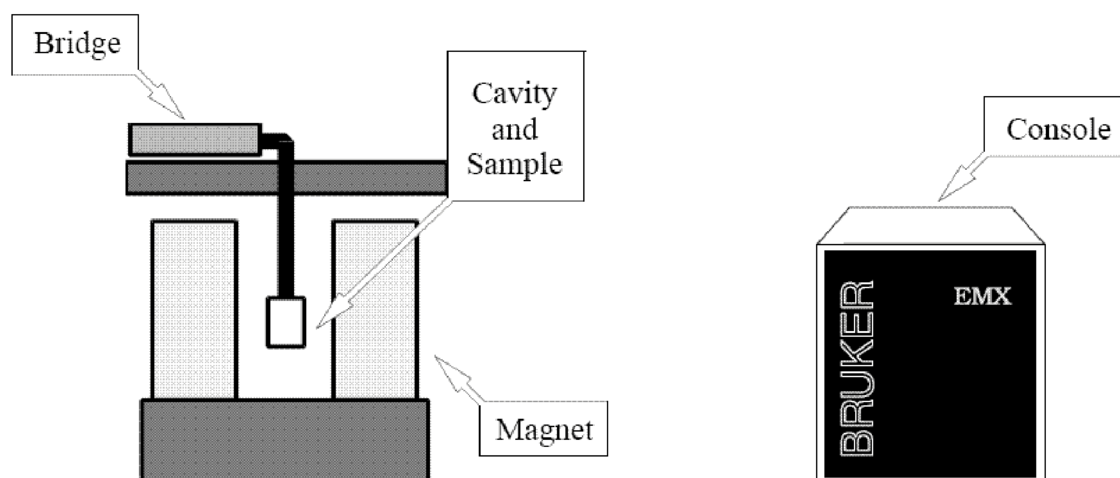

Figure 10-1: General layout of an EPR spectrometer

The electromagnetic radiation source and the detector are in a box called 'the microwave bridge'. The sample is a microwave cavity, which is a metal box that helps to amplify weak signals from the sample. There is a magnet to tune the electronic energy levels. We have also a console which

contains signal processing and control electronics and a computer. The computer is used for analyzing data and coordinating all the units for acquiring a spectrum.

10.1 Source

The frequency of radiant energy used in the majority of EPR spectrometers is approximately 9.5 GHz, in the medium-frequency microwave region. This frequency corresponds to a wavelength of about 32 mm. This source is usually a klystron, a vacuum tube with a low-noise characteristic. The field B is generated by oscillations within its own tunable cavity.

Table 10-10.1: Microwave frequency bands

Band	Frequency	$\boldsymbol{\lambda}$	$\boldsymbol{B_0(g=2)}$
L	1 GHz	30 cm	36 mT
C	3 GHz	10 cm	0.1 T
X	10 GHz	3 cm	0.35 T
K	24 GHz	1.25 cm	0.86 T
Q	35 GHz	8.5 mm	1.25 T
V	70 GHz	4.3 mm	2.5 T
W	94 GHz	3 mm	3.4 T

10.2 EPR cavity

In the EPR machine, a microwave cavity is used to amplify weak signals to the sample. A microwave cavity is a metal box with a rectangular or cylindrical shape which resonates with microwaves. The cavity stores the microwave energy; therefore at the resonance frequency of the cavity microwave will remain inside the cavity instead of being reflected back. Every cavity is characterized by the Q or quality factor, it is an indicator of how efficiently the cavity stores microwave energy. As Q increases, the sensitivity of the spectrometer increases. We can measure Q factors from this equation:

$$Q = \frac{\nu_{res}}{\Delta \nu} \tag{10.1}$$

where ν_{res} is the resonant frequency of the cavity and $\Delta \nu$ is the width at half height of the resonance.

Another way to express the quality factor is:

$$Q = \frac{2\pi(energy\ stored)}{energy\ dissipated\ per\ cycle} \tag{10.2}$$

Where the energy dissipated per cycle is the amount of energy lost during one microwave period. The presence of a standing wave inside the cavity is the consequence of the resonance condition. Standing electromagnetic waves have their electric and magnetic field component exactly out of phase (where the magnetic field is maximum, the electric field is minimum and vice versa). In the

following figure we can see the spatial distribution of the amplitudes of the electric and magnetic fields in the most common EPR cavity:

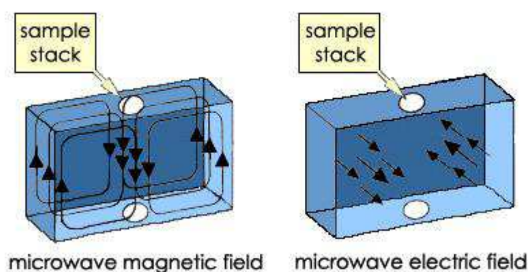

Figure 10-2: Magnetic and electric field patterns in an EPR cavity

We can use the spatial separation of the electric a magnetic fields in a cavity to great advantage. Most samples have non-resonant absorption of the microwaves via the electric field and the Q factor will be degraded by an increase in the dissipated energy. It is the magnetic field that drives the absorption in EPR. Therefore, if we place our sample in the electric field minimum we obtain the biggest signals and the highest sensitivity.

10.3 Magnetic field

In magnetic resonance experiments, the static magnetic field B usually must be very well controlled and stable. Variations of this field correspond to variations in energy separation. The magnitude of B may be measured and controlled by a Hall-effect detector. Since every absorption line has a non-zero width, it is convenient to use a scanning unit to traverse the region of field B encompassing the line. Unless B is uniform over the sample volume, the observed spectral line is broadened [21].

10.4 Signal channel

To enhance the sensitivity of the spectrometer a technique known as phase sensitive detection is used in order to have less noise from the detection diode and to eliminate baseline instabilities. The signal channel fits in the spectrometer console and contains the required electronics for the phase sensitive detection.The sample experienced a magnetic field strength that is modulated sinusoidally at the modulation frequency.

The signal channel is known as a lock-in amplifier of phase sensitive detector and produce a DC signal proportional to the amplitude of the modulated EPR signal: it compares the modulated signal with a reference signal having the same frequency as the field modulation and it is only sensitive to that signals which have the same frequency and phase as the field modulation. All the signals that not fulfill these requirements are suppresses.

10.5 Magnetic field controller

The magnetic field controller allows us to sweep the magnetic field in a controlled and precise manner for our EPR experiment. It consists of two parts; a part which sets the field values and the timing of the field sweep and a part which regulates the current in the windings of the magnet. A microprocessor in the controller controls the magnetic field values and the timing of the magnetic field sweep.

In Figure we can see a block diagram of the field controller and the associated components.

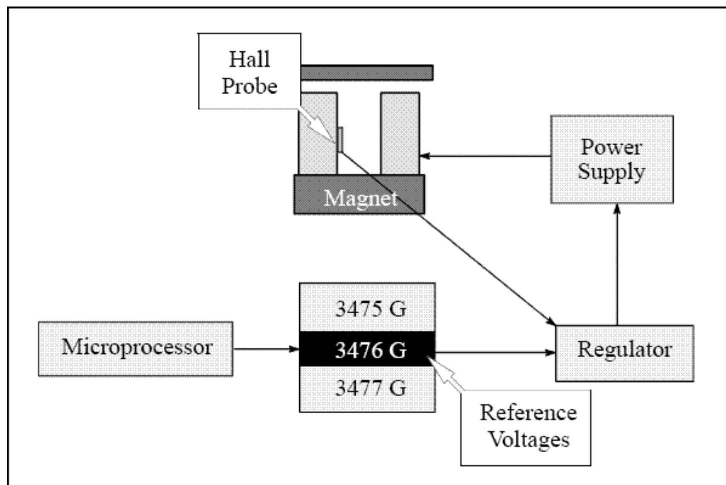

Figure 10-3: Block diagram of a field controller

The magnetic field regulation occurs via a Hall probe placed in the gap of the magnet. It produces a voltage that is dependent on the magnetic field perpendicular to the probe.

10.6 Spectrum

In figure we can see a block diagram of an EPR spectrometer containing all the analyzed individual components [21].

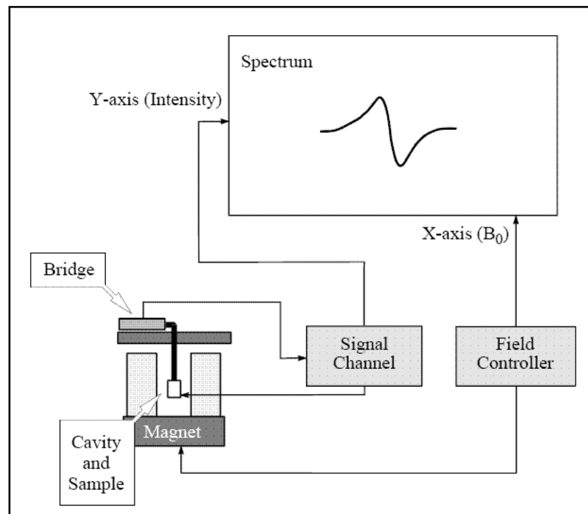

Figure 10-4: Block diagram of an EPR spectrometer

11 Oxidation and Deposition techniques

This chapter explains the oxidation and deposition techniques used to realize our EPR samples. Al2O3 was deposited for each group using Plasma Atomic Layer Deposition from OpAl. The OpAl system can provide both plasma and thermal ALD in a single tool. As far as the SiOx deposition is concerned, a dry thermal oxidation process was used.

11.1 Atomic Layer Deposition (ALD)

To deposit Al_2O_3 on our FZ-Si wafers we used the Atomic Layer Deposition Technique (ALD). In this section a small overview about this technique is given.

The ALD process is based on self-limiting surface reactions: the substrate surface is exposed to gas phase-precursors [22]. The reactions are self limiting because they automatically stop when all available surface groups have reacted: every surface chemical reaction occurs between a reactant (gas-phase) and a surface functional group [2, 22].

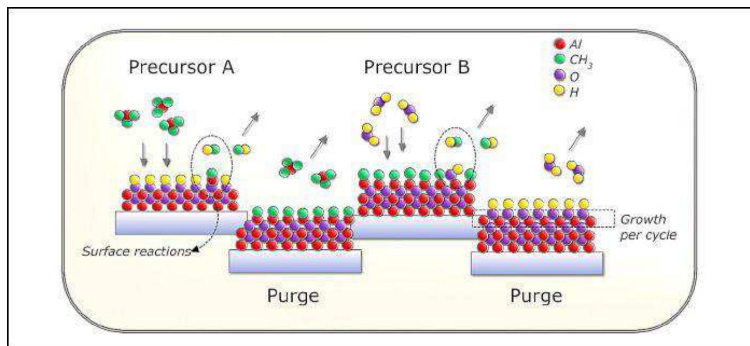

Figure 11-1: Schema of ALD cycle: two precursor dosing steps and two purge steps [2]

A standard ALD process uses two different precursors, that we can call A and B. An ALD cycle is based on the following steps: precursor A react with the substrate; the remaining precursor and reaction products are pumped away; precursor B is introduced; reaction occurs with the new surface functional group; at the end the initial surface groups are restored [2] .

Al2O3 can be deposited using ALD using trimethylaluminum (Al(CH3))3 as aluminum source.There are two possible method of ALD: thermal- and plasma assisted ALD. When processes with water and ozone are involved we can speak about thermal ALD, while the processes employing a plasma are typical of the plasma assisted ALD. In our work we decide to use the last one: plasma assisted ALD. The reactivity of plasma ALD can offer a better film quality with lower impurity levels [2].

Al2O3 deposition can be realized also by other techniques, such as sputtering and Plasma-enhanced chemical vapor deposition (PECVD). Advantages of ALD over PECVD are the perfect

uniformity achievable on large substrates, the low substrate temperatures used in the process. ALD allows also the production of multilayer structures [2].

In the following picture we can see a schematic representation of a thermal and plasma cycle.

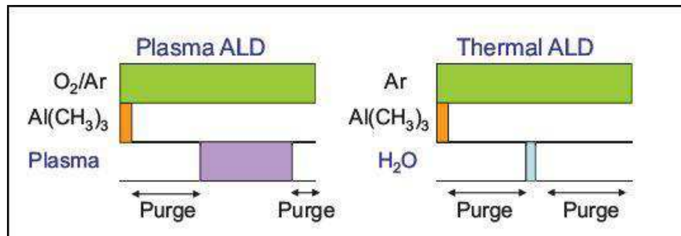

Figure 11-2: Schematic representationof typical plasma and thermal ALD cycles for AL2O3 [2].

For the first half-cycle the surface chemistry is the same for plasma and thermal ALD. During the second half-step we have a change of the surface from methyl-terminated to hydroxyl-terminated. In this second-half cycle the chemistry for plasma and thermal ALD is different: for thermal ALD for example methane is produced during the second half-cycle [2].

The following picture shows the thickness of the Al2O3 film in function of the number of ALD cycles, for both plasma and thermal ALD.

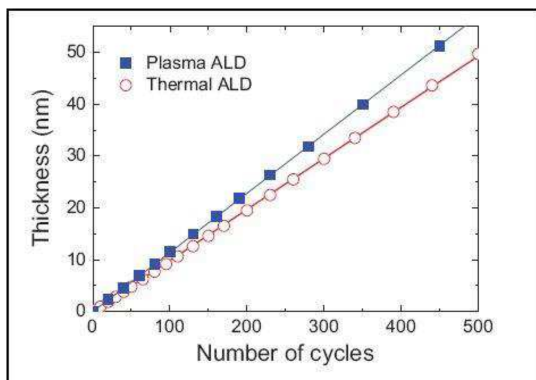

Figure 11-3: Al2O3 film thickness vs Number of cycles for both Plasma ALD (blue line) and Thermal ALD (red line) [2]

11.2 Dry thermal oxidation

In order to realize our Si/SiOx/Al2O3 layer stack systems, part of our Si samples underwent a dry thermal oxidation process before the Al2O3 ALD deposition. Thermal oxidation is one of the most important methods used to oxidize semiconductors. Other oxidation methods are for example electrochemical anodization and plasmaenhanced chemical vapor deposition (PECVD).

In the following picture we can see a schematic cross section of a resistance-heated oxidation furnace.

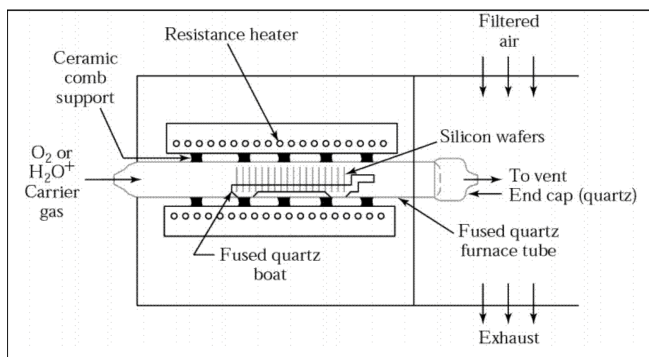

Figure 11-4: Schematic cross section of a resistance-heated oxidation furnace

Thermal oxidation of silicon in oxygen is called dry oxidation (equation (11.1)) and we call wet oxidation (equation (11.2)) thermal oxidation with water vapor wet:

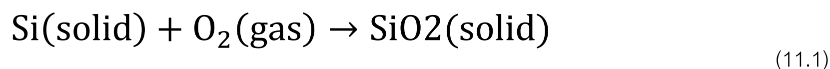

$$\mathrm{Si(solid)} + \mathrm{O_2(gas)} \rightarrow \mathrm{SiO2(solid)}$$

(11.1)

$$\mathrm{Si(solid)} + 2\mathrm{H_2O(gas)} \rightarrow \mathrm{SiO_2(solid)} + 2\mathrm{H_2(gas)}$$

(11.2)

During the formation of the oxide of thickness *x* a layer of silicon of thick-

ness 0.44 *x* is consumed.

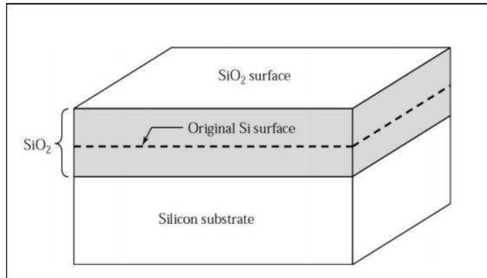

Figure 11-5: Growth of silicon dioxide by thermal oxidation

We can now summarize the basic model for silicon thermal oxidation.

A silicon slice contacts the oxidizing species (oxygen and water vapor): that results in a surface concentration of C_0 for these species. The magnitude of C_0 is equal to the equilibrium bulk concentration of the species in the oxidation temperature. The equilibrium concentration is proportional to the partial pressure of the oxidant adjacent to the oxide surface. The oxidizing species diffuses through the silicon dioxide layer, resulting in a concentration C_s at the surface of silicon. We can write at this point the expression for the flux F_1 as follows:

$$F_1 = D\frac{dC}{dx} \cong \frac{D(C_0 - C_s)}{x} \qquad (11.2)$$

where D is the diffusion coefficient of the oxidizing species and x is the thickness of the oxide layer already present.

At the silicon surface, the flux F_2 is given by:

$$F_2 = \kappa C_s \tag{11.3}$$

where κ is the surface reaction rate constant oxidation.

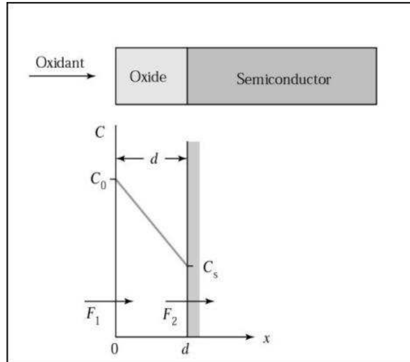

Figure 11-6: Thermal oxidation model

From equation (11.2) and equation (11.3) we can write:

$$F = \frac{DC_0}{x + \left(\frac{D}{\kappa}\right)} \tag{11.4}$$

And the growth rate of the oxide layer thickness is given by:

$$\frac{\mathrm{dx}}{\mathrm{dt}} = \frac{F}{C_1} = \frac{\frac{DC_0}{C_1}}{x + \left(\frac{D}{\kappa}\right)} \tag{11.5}$$

This equation can be solved to find the oxide thickness x after an oxida time t.

During the early stages of oxide growth the oxide thickness varies linearly with time. As the oxide layer becomes thicker, the oxidant must diffuse though the oxide layer to react at the silicon-silicon dioxide interface, and the reaction becomes diffusion limited. The oxide growth at this point becomes proportional to the square root of the oxidizing time, which results into parabolic growth rate.

12 Experimental plan and results

12.1 Introduction

Electron paramagnetic resonance (EPR) has been used to investigate the interface between Si and the high-k dielectric Al2O3, with or without the presence of a thermal grown SiOx layer. We also tried to understand the origin of fixed negative charges formed at the SiO2/Al2O3 interface. In our study several parameters were varied: the thickness of the Al2O3 layer, the interlayer SiOx thickness, the thickness and the surface of the Si substrate. Also the effect of different temperature treatments (annealing) on Si/Al2O3 and Si/SiOx/Al2O3 stacks were considered. We studied 5 different groups of samples: for the first 4 groups we used as starting substrates p FZ-Si, 50 µm thick and with a resistivity of 100 Ohm·cm; the starting substrate for group 5 is p-FZ Si, with a thickness of 250 µm and a resistivity of 100 Ohm·cm.

12.2 EPR experiments

Group 1

The aim of this experiment is to investigate the effect of annealing on Si/Al2O3 stack layers, comparing the spectra obtained by EPR
spectroscopy.
All the samples underwent a 30% KOH cleaning at 80°C for 1 minute. Potassium hydroxide is one of the anisotropic wet etching agents for silicon. The KOH etch rate is strongly affected by the

crystallographic orientation of the silicon. The wet etch process can be described by three basic steps: diffusion of the liquid etchant to the structure that is to be removed; the reaction between the liquid etchant and the material being etch away; diffusion of the byproducts in the reaction from the reacted surface.

Then the wafers underwent a HCl, hydrochloric acid, cleaning (3%) for 2 minutes, wet chemical cleaning using Nitric acid (HNO3) for 10 minutes at 110°C, followed by (HF) solution for 1 minute.

Isotropic etchant, such as HF and HNO3, having dissolution rates independent of orientation are needed: these tend to uniformly remove material and are limited by the mass transport of chemical species [23].

After the cleaning step the wafers are deposited with an Aluminum oxide passivation layer on both sides with Plasma Enhanced ALD, 300 cycles, 180°C. 300 cycles correspond to a thickness of about 35 nm.

Different annealing conditions were performed: three different samples were prepared. One subgroup did not undergo annealing after the Al2O3 deposition; the second one underwent an annealing process for 2 minutes (450°C, hot plates) and the last one underwent an annealing step for 5 minutes. The lifetime of the reference wafers before and after annealing step is measured using the QSSPC technique. To ensure that the desired thickness is achieved, the layer thickness of the reference wafer is measured using the ellipsometer characterization after the deposition process.

For all these three subgroups 10 small samples were put in a quartz tube for EPR measurements.

EPR measurements were performed at room temperature with a Bruker EMX machine, using a microwave frequency of approximately 9.8 GHz (X-band). The g values were calculated by comparing the field position of the resonance with that of a resonance of known value, in our case 2,2-diphenyl-1-picrylhydrazyl radical, DPPH. DPPH is in fact the most popular standard of the position (g-marker) and intensity of electron paramagnetic resonance: the EPR splitting factor for DPPH is calibrated at $g = 2.0036$.

To improve the signal-to noise ratio without distorting the EPR line, each spectrum has been averaged over a large number of scans, 537scans. Measurements were conducted at non saturating power with an attenuation of 20 dB.

Measurements were conducted at non saturating power. A measurement was conducted to test the saturating power. We obtained three spectra, measured at three attenuation values: 40 dB, 25 dB and 10 dB. This measurement showed that also measuring with attenuation value of 10 dB saturation did not occur; that allowed us to use a higher power for our measurements.

In figure we can see the experimental flow for group 1.

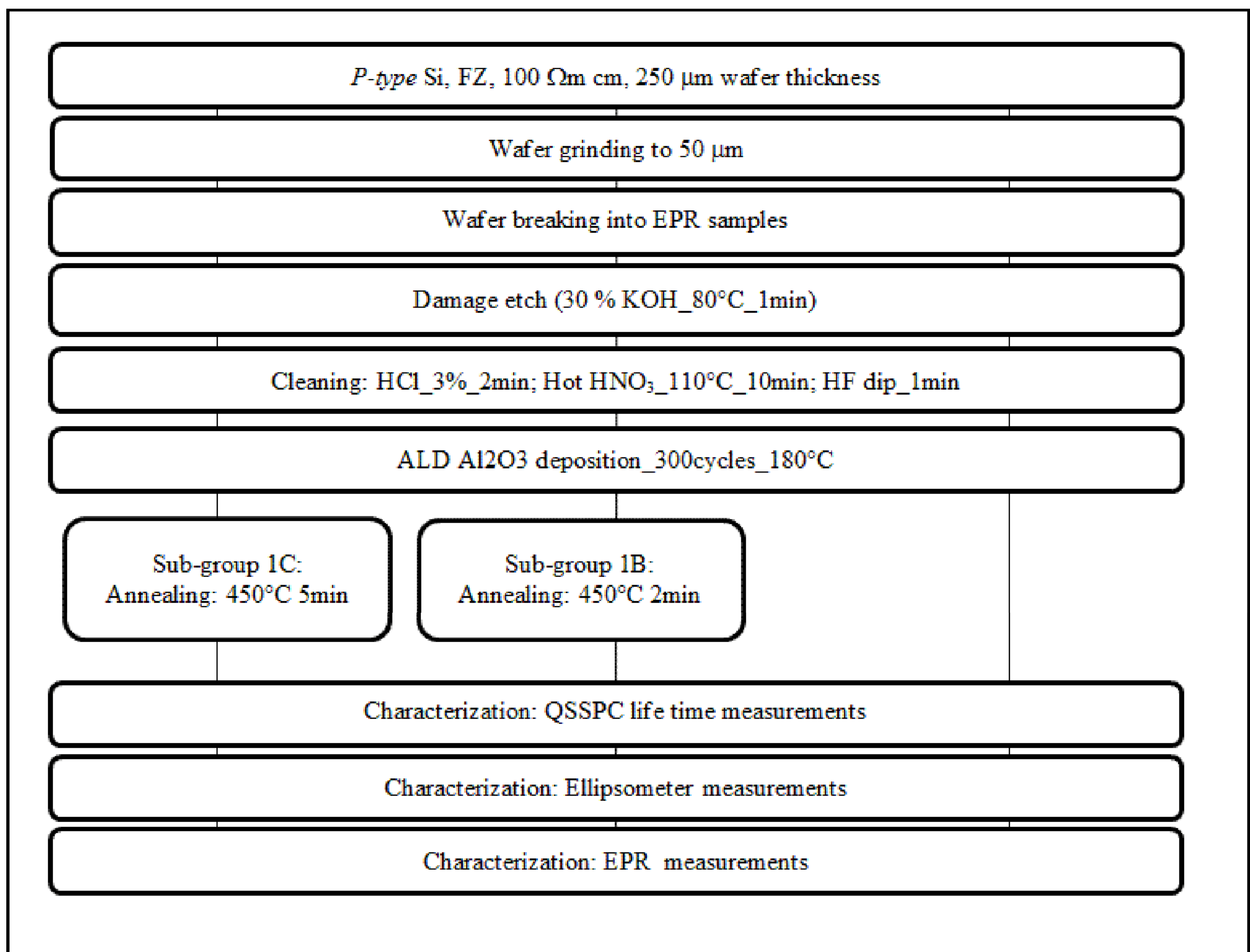

Figure 12-1: experimental flow for group 1

This table shows the different annealing conditions for the three subgroups under study. We also reported lifetime and thickness values, measured with the QSSPC technique and the Ellipsometer spectroscopy respectively.

Table 12-1: Annealing conditions, lifetime and thickness values of group 1

Sub-groups	substrates p-FZ-Si thickness	Al2O3 thickness (ALD cycles)	Annealing conditions	QSSPC lifetime measurements	Al2O3 thickness (nm): Ellipsometer measurements
1A	50 µm	300	-	05 µs	(39.48 ± 0.08)
1B	50 µm	300	2 mins,450°C, hotmplates	3.829 µs	(39.48 ± 0.08)
1C	50 µm	300	5 mins, 450°C, hotplates	7.051 µs	(39.48 ± 0.08)

For the lifetime measurement the principal errors that can be identified are the uncertainty of the resistivity of the wafer given by the manufacturer and the one related to the arbitrary choice of the optical constant (in the generalized mode).

The following figure shows the spectra observed at room temperature for a p-type FZ-Si layer. EPR allows the detection of both bulk and interface defects. We wanted therefore to compare this spectrum with those observed for Al2O3/Si systems in order to establish the nature of the detected

defects (bulk or interface). We fit this spectrum with known g-factors values, relating to Boron interstitial.

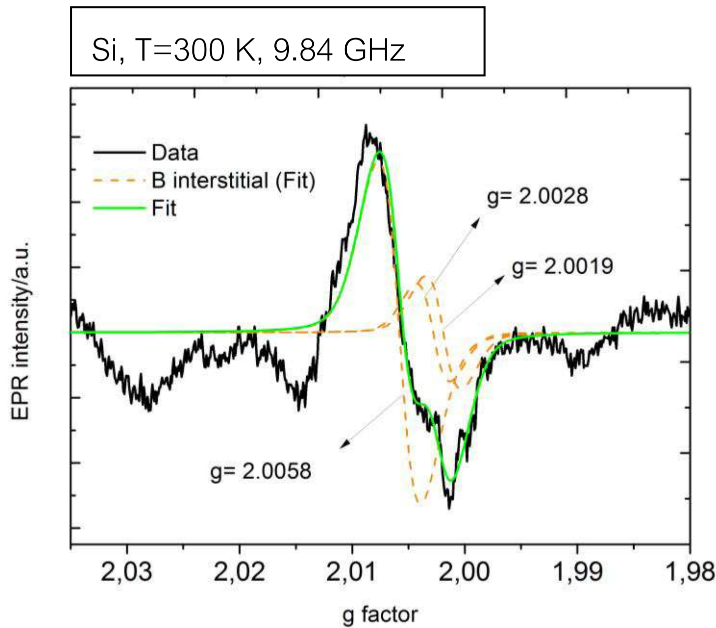

Figure 12-2: Electron Paramagnetic Resonance (EPR) spectra observed at room temperature for a p-type FZ-Si layer. The thick black solid line shows the measured data. The thin lines represent the signals of the anisotropic center (orange dashes) used to fit the experimental data. The thick green solid line is the overall result of the deconvolution

Table 12-2: g-factor values obtained for Si samples

Center number	g factor value	Possible Attribution
Center 0	$gx = 2.0058 \pm 0.0002$ $gy = 2.0028 \pm 0.0002$ $gz = 2.0019 \pm 0.0002$	Boron interstitial [24, 25]

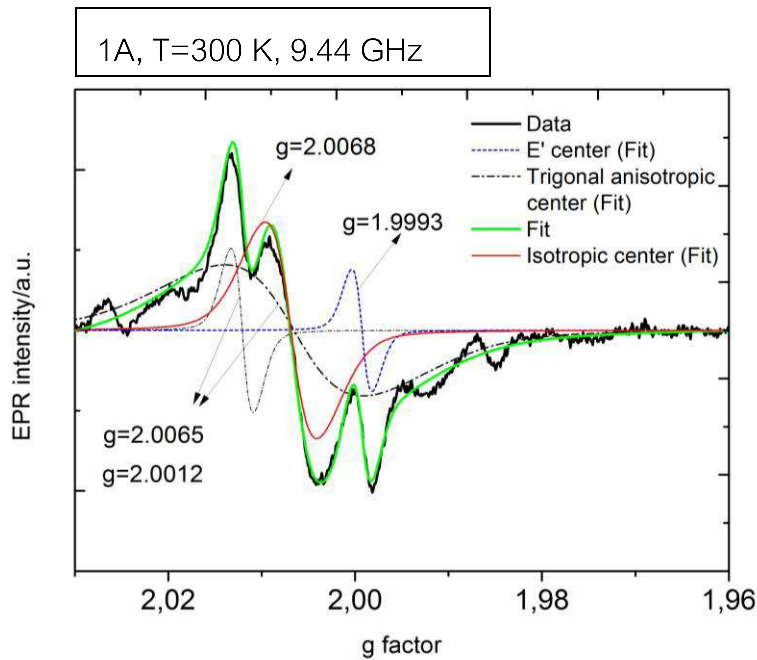

Figure 12-3: Electron Paramagnetic Resonance (EPR) spectra observed at room temperature for atomic layer deposition (ALD, 300 cycles)-grown Si/Al2O3 interfaces. The thick black solid line shows the measured data. The thin lines represent the signals of the trigonal anisotropic center (black dots-dashes), the isotropic center (red solid) and the E'-like center (blue dots-dashes) used to fit the experimental data. The thick green solid line is the overall result of the deconvolution

Table 12-3: g-factor values obtained for sub-group 1A

Center number	g factor value	Possible Attribution
Center 1	$g_x = g_Y = g_z = 2.0068 \pm 0.0002$	Si-db [26]
Center 2	$g_\parallel = 2.0012 \pm 0.0002$ $g_\perp = 2.0065 \pm 0.0002$	Pb0 center [2, 27, 28]
Center 3	$g = 1.9993 \pm 0.0001$	E'-like defect [2]

Interface defects: Pb0 and Pb1

Pb0 and Pb1 are typically (100)Si/SiO2 interface defects. Also Si/Al2O3 interface as well as Si interface with other high k dielectric such as ZrO2 exhibits this kind of defects. The Pb-type defect is a trivalent bonded Si atom. At the electronic point of view, the Si/Al2O3 interface can be regarded

as Si/SiO2-like. Many EPR studies have proved the similarity between Si/Al2O3 and Si/thermally grown SiOx.

The Pb-type defect is a trivalent bonded Si atom.

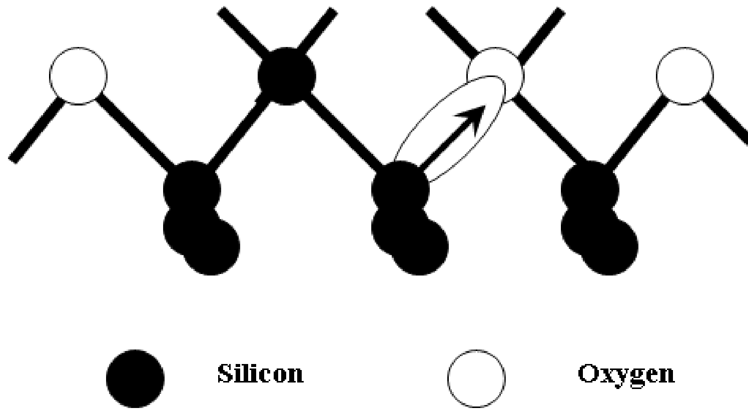

Figure 12-4: Schematic illustration of a Pb center at the (111)Si/SiO2 interface [29]

At the (111) Si/SiO2 interface the Pb center is supposed to be a (111) oriented silicon dangling bond. On (100) silicon, two related defects called Pb0 and Pb1 are observed. Poindexter and co-workers found that the Pb0(100)center is almost identical to the Pb(111) center, as far as its EPR spectrum and its electrical levels are concerned. The Pb1 (100) center, on the other hand, is characterized by a lower symmetry and lower electron-electron correlation energy. The Pb1 center could be considered characteristic for the (100) orientation because it has not been observed for the other orientation. The structure of the Pb(111) center is quite well understood; on the other hand the precise origin of the Pb0 and Pb1 resonances on (100) silicon is still an open question [27]. Poindexter et al. have proposed a model in which all of these defects are considered silicon dangling-bond centers: the only differences are the orientation and the neighbors (silicon or oxygen atoms) [30].

The Poindexter Pb0 (100) center corresponds to a (111) oriented dangling bond with three nearest-neighbor silicon atoms and a second-nearest neighbor oxygen, while the Pb1(100) center has one nearest neighbor oxygen [30, 31].

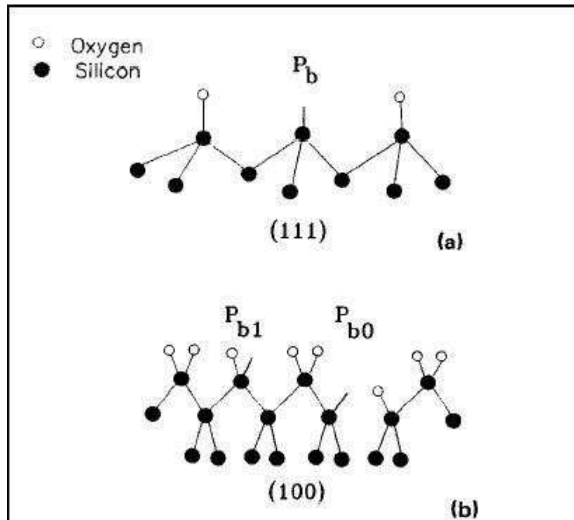

Figure 12-5: a) Dangling bond at the (111) interface b) Pointdexter model for Pb center at the (100) interface [31]

SPECTRA ANALYSIS AND DISCUSSION

The spectrum in Figure 12-3 appears to be the superposition of an isotropic signal with g=2.0068, an E' –like signal with g=1.9993 and an anisotropic signal ($g_{\parallel}$= 2.0012 and $g_{\perp}$= 2.0065). Because of the overlapping of the different lines, it is difficult to extract the anisotropic lines present in the spectra. Therefore we have tried several possible decompositions of the spectra and the best deconvolution has been obtained for the case described above. All the fits in our work assume Pseudo-Voigt lines.

No signal related to boron interstitial has been observed: that should lead to the conclusion that all the detected defects come from the interface (see spectrum SV0).

Dingemans et al. have already observed the E'-like center analyzing the EDMR spectra obtained for plasma ALD Al2O3 films deposited on Si(100)[2]. The E' like defect is associated with the SiOx interface.

E' centers can act as hole traps and they play an important role in trap-assisted tunneling phenomena in electrically stressed oxides. Both positively charged and neutral E' centers can be generated in SiO2 films; several E' variant can be generated in thin films and most of them involve hydrogen complexed E' centers.

For the isotropic signal we found g=2.0068; it is related to a common dangling bond center observed in disordered and amorphous silicon [2, 28].

It was possible also to identify the Pb0 anisotropic center ($g_{\parallel}$= 2.0012 and $g_{\perp}$= 2.0065). Stesmans and Afanas'ev have reported that Si/Al2O3 interface exhibits Pb-type defects: Pb0 and Pb1.[32] The same results were also obtained by Dingemans et al. [2] In table 1 the principal values of the Pb0 g-tensor obtained in different scientific works are reported.

Table 12-4: principal values of the Pb0 g-tensor obtained in different scientific works

Layers and interface orientation	g tensor: principal values
(100)Si/SiO2	g1= 2.0015 g2= g3= 2.0087 [27]
(100)Si/Al2O3	g1= 2.0036 g2= g3= 2.0087 [2]
(100)Si/Al2O3	g1= 2.0024 g2= g3= 2.0074 [28]
(100)Si/Al2O3/ZrO2	g1= 2.00185 g2= g3= 2.0081[32]

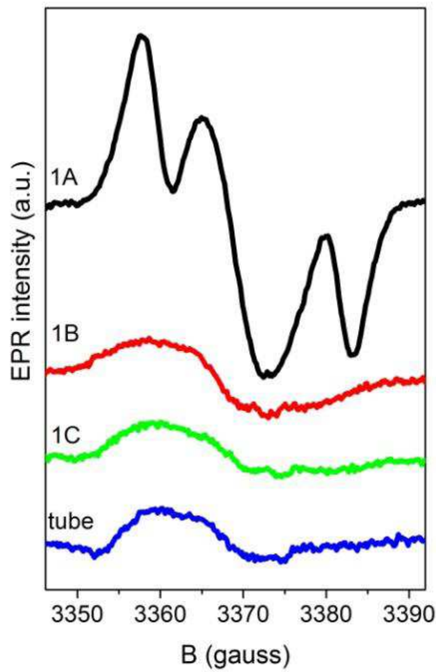

Figure 12-6: Electron Paramagnetic Resonance (EPR) spectra observed at room temperature for atomic layer deposition (ALD, 300 cycles)-grown Si/Al2O3 interfaces. Overall results of the deconvolution for sub-group 1A (black line), 1B (red line), 1C (green line)

As far as sub-groups 1B and 1C are concerned, our spectra did not reveal the presence of Si-dangling bonds (see figure 12-6). It seems therefore that the 5 minutes hot plates exposure doesn't cause further reduction in the concentration of unpassivated defects in compare with the 2 minutes annealing process. This fact is in good agreement with the results obtained by Dingemans et al [2]. In many studies a low defect interface density, D_{it}, was found after annealing.

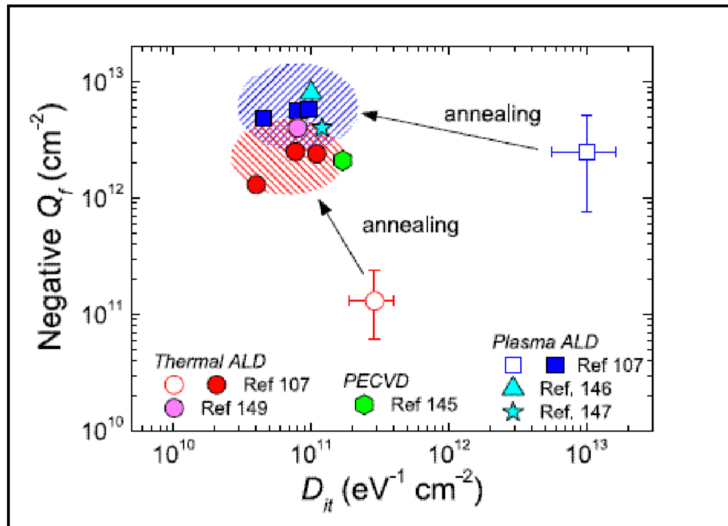

Figure 12-7: Dingemans et al. reported the influence of annealing on the negative charge Qf and on the interface defect density, Dit, obtained in various studies. Annealing took place at about 400°C [2]

As we can see from Table 12-1, lifetime of sub-groups 1B and 1C samples has increased after annealing. Comparing the two values of lifetime, we can notice that an annealing time of 2 minutes can already be sufficient to strongly reduce the surface recombination velocity and therefore activate the passivation performance. For an annealing time of 5 minutes we haven't noticed a further increase in the sample lifetime. As seen in *section 6*, Qf, the negative charge density, increases as the surface recombination velocity decreases. Therefore, we can say that the negative fixed charge density has increased after annealing.

Therefore we found out a correlation between the increase of negative charge density Qf and the absence of paramagnetic silicon dangling bonds.

Group 2

In the second experiment samples were prepared varying the thickness of the Al2O3 layer.We also investigated the effect of annealing on these Si/Al2O3 stack layers. EPR spectra were compared with those of group 1.

In figure we can see the experimental flow for group 2.

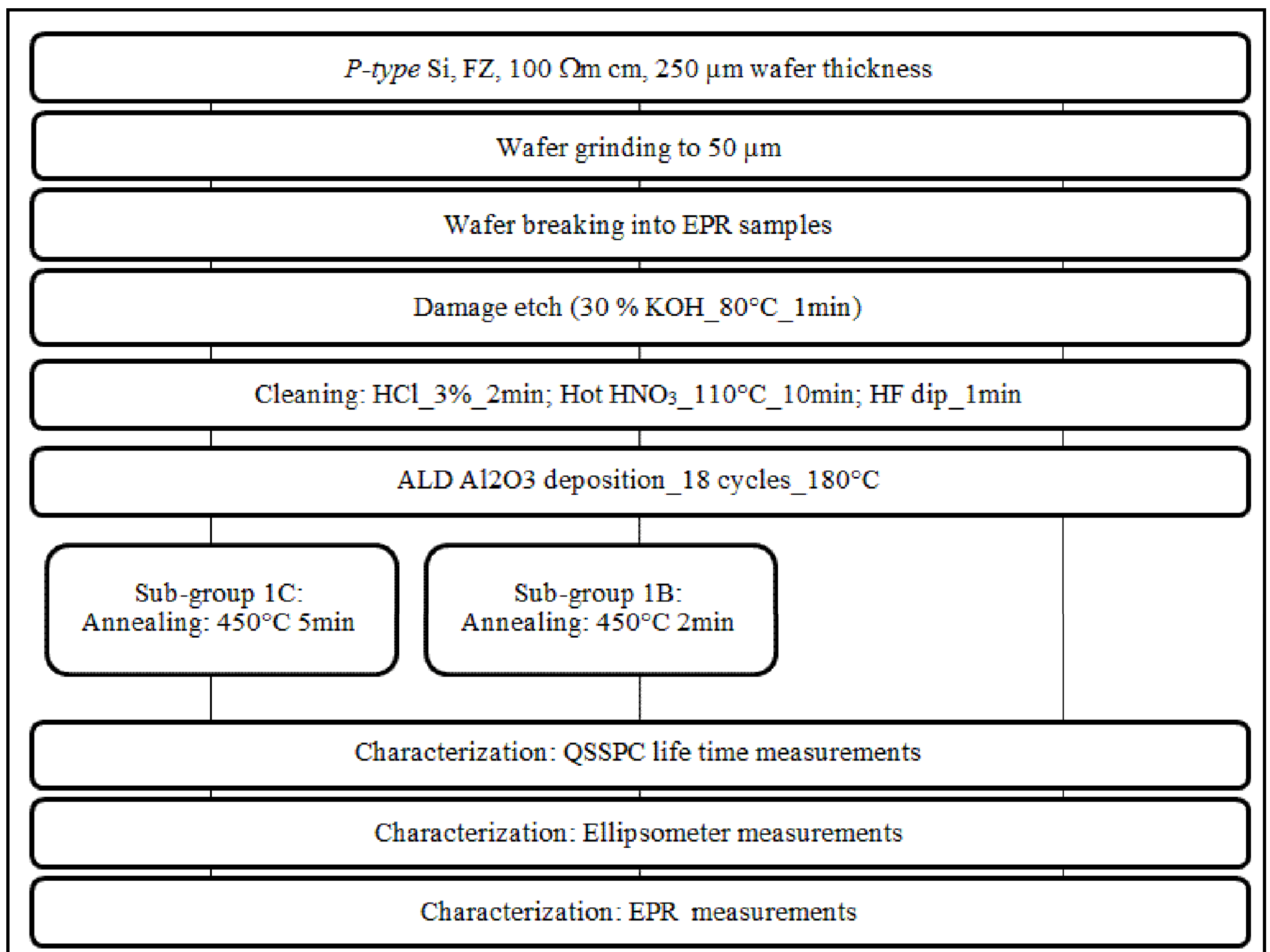

Figure 12-8: experimental flow for group 2

All the samples of group 2 underwent the same cleaning step as group 1. After the cleaning step the wafers are deposited with an Aluminum oxide passivation layer on both sides with Plasma Enhanced ALD, 18 cycles, 180°C. The thickness of Al2O3 was varied: 18 cycles corresponds to a thickness of a few nm. To ensure that the desired thickness is achieved, the layer thickness of the reference wafer is measured using the ellipsometer characterization after the deposition process. Different annealing conditions were performed: three different samples were prepared. One sub-group did not undergo annealing after the Al2O3 deposition, the second one underwent an annealing process for 2 minutes (450°C, hot plates) and the last one underwent an annealing step for 5 minutes.The lifetime of the reference wafer before the annealing step is measured using the QSSPC technique.

EPR measurements were conducted with the same parameter as group 1 (See group 1).

In this case, to improve the signal-to noise ratio without distorting the EPR line, each spectrum has been averaged over a 999 scans.

Table 12-5: Annealing conditions, lifetime values of group 2

Sub-groups	substrates p-FZ-Si thickness	Al2O3 thickness (ALD cycles)	Annealing conditions	QSSPC lifetime measurements
2A	50 µm	18	-	23 µs
2B	50 µm	18	2 mins,450°C, hotplates	344 µs
2C	50 µm	18	5 mins, 450°C, hotplates	501 µs

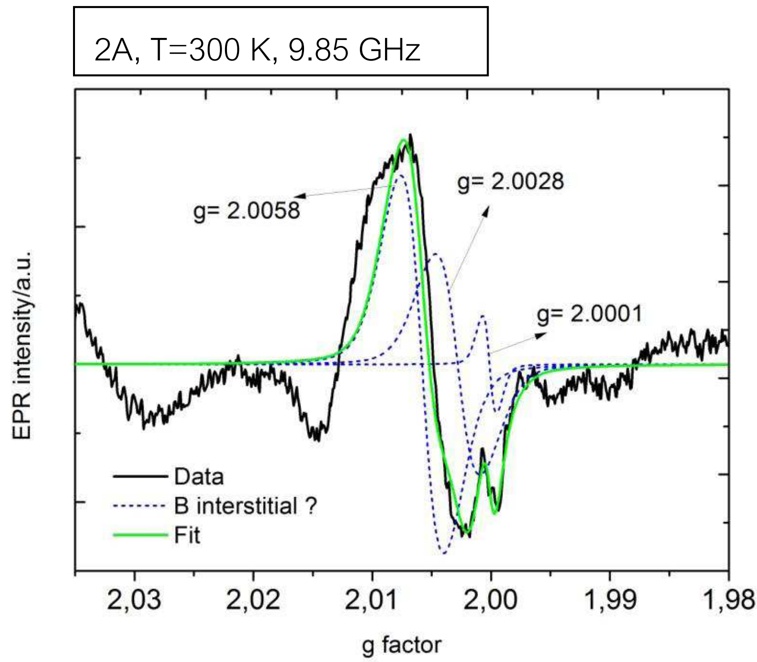

Figure 12-9: Electron Paramagnetic Resonance (EPR) spectra observed at room temperature for atomic layer deposition (ALD, 18 cycles)-grown Si/Al2O3 interfaces. The thin lines represent the signals of the anisotropic center (blue dashes) used to fit the experimental data. The thick green solid line is the overall result of the deconvolution

Table 12-6: g-factor values obtained for sub-group 2A

Center number	g factor value	Possible Attribution
Center 0	$g_x = 2.0058 \pm 0.0002$ $g_Y = 2.0028 \pm 0.0002$ $g_z = 2.0001 \pm 0.0002$	Boron interstitial [24, 25]

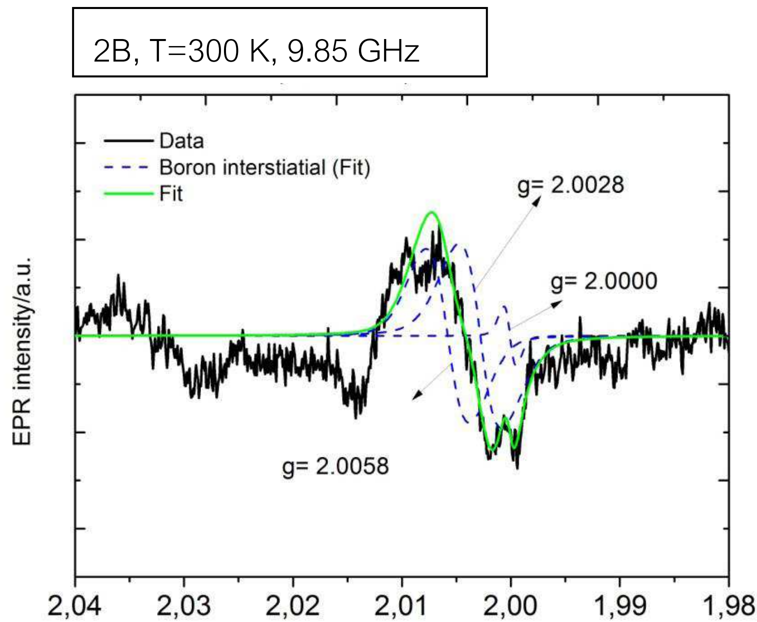

Figure 12-10: Electron Paramagnetic Resonance (EPR) spectra observed at room temperature for atomic layer deposition (ALD, 18 cycles)-grown Si/Al2O3 interfaces (2 mins,450°C, hotplates). The thin lines represent the signals of the anisotropic center (blue dashes) used to fit the experimental data. The thick green solid line is the overall result of the deconvolution

Table 12-7: g-factor values obtained for sub-group 2B

Center number	g factor value	Possible Attribution
Center 0	$g_x = 2.0058 \pm 0.0002$ $g_Y = 2.0028 \pm 0.0002$ $g_z = 2.0000 \pm 0.0002$	Boron interstitial [24, 25]

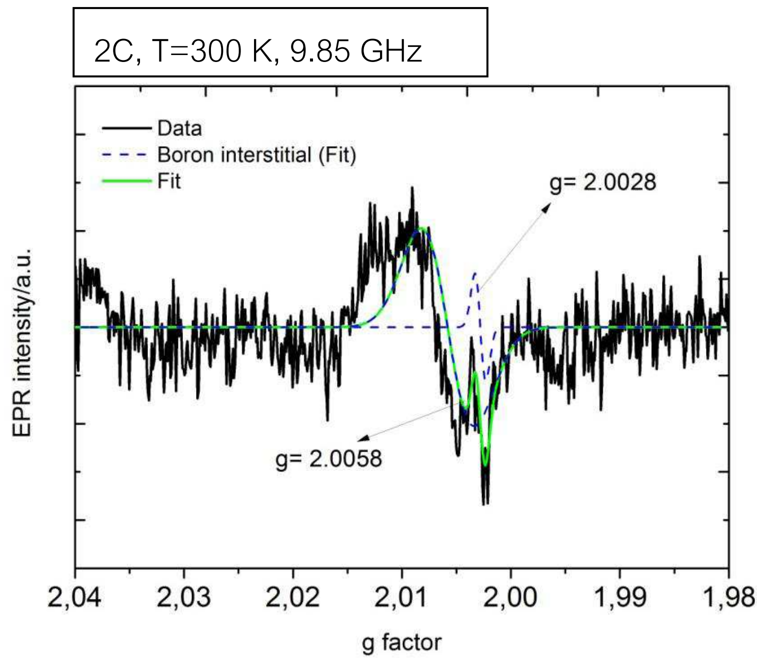

Figure 12-11: Electron Paramagnetic Resonance (EPR) spectra observed at room temperature for atomic layer deposition (ALD, 18 cycles)-grown Si/Al2O3 interfaces (5 mins, 450°C, hotplates). The thin lines represent the signals of the anisotropic center (blue dashes) used to fit the experimental data. The thick green solid line is the overall result of the deconvolution

Table 12-8: g-factor values obtained for sub-group 2B

Center number	g factor value	Possible Attribution
Center 1	$g_x = 2.0058 \pm 0.0002$ $g_Y = 2.0028 \pm 0.0002$	Boron interstitial [24, 25]

SPECTRA ANALYSIS AND DISCUSSION

For this second experiment we fitted our spectra assuming only the presence of an isotropic center (blue dashes), possibly related to a boron interstitial. Pseudo-Voigt lines have been therefore fixed at the known g-values for Boron interstitial: gx=2.0058; gy=2.0028 and gz=2.0000. No lines related to Silicon dangling bonds, E' center has been detected. This could probably be due to the thinner Al2O3 deposited layer: 18 cycles correspond to a few nm in thickness. That should explain why we

can see only defects related to the bulk. It was also more difficult to fit our spectra because the sensitivity of the EPR apparatus is directly proportional to the volume of the samples: in this case we put in the quartz tube the same amount of samples (10) but we lowered the thickness of the Al2O3 layer.

COCOS MEASUREMENTS

We measured the total negative charge at the Si/Al2O3 interface of two reference wafers using the COCOS technique: “Corona-Oxide-Semiconductor Characterization” (see *Appendix*).
One wafer underwent usual cleaning steps and the Al2O3 ALD deposition (18 cycles)
The second wafer underwent the usual cleaning steps, the ALD deposition (18 cycles) and an annealing process using hot plates (450°C, 5 minutes). In this table we show the results:

Table 12-9: Annealing condition, AL2O3 thickness (cycles) and Qtot measured using the COCOS technique

Sub-group	Annealing condition	Al2O3 thickness(cycles)	$\mathrm{Qtot}(\mathrm{cm}^{-2})$
2A	5 minutes, 450°C hotplates	18	$-7 \cdot 10^{12}$
2C	Without annealing	18	$-3.6 \cdot 10^{12}$

The results show that although we can’t detect with the EPR analysis any paramagnetic Silicon dangling bonds, at the Si/Al2O3 interface a negative charge density is still present and the value increase after annealing treatment. QSSPC measurements (see table 12-5) show also a strong increase in the lifetime for the two samples that underwent the annealing process.

Group 3

The thickness of the SiOx layer between the Si substrate and the Al_2O_3 layer strongly impacts the passivation quality and interface parameters of the stack. S.Mack et al. found out that a certain thermal SiOx thickness is required to achieve appropriate chemical passivation [33].

It has been demonstrated that an increased in the SiO_2 layer thickness over the range of 1-30 nm leads to a decrease in negative Qf, with a transition from net negative charge to positive fixed charge[2]. In figure we can see the experimental flow for group 3.

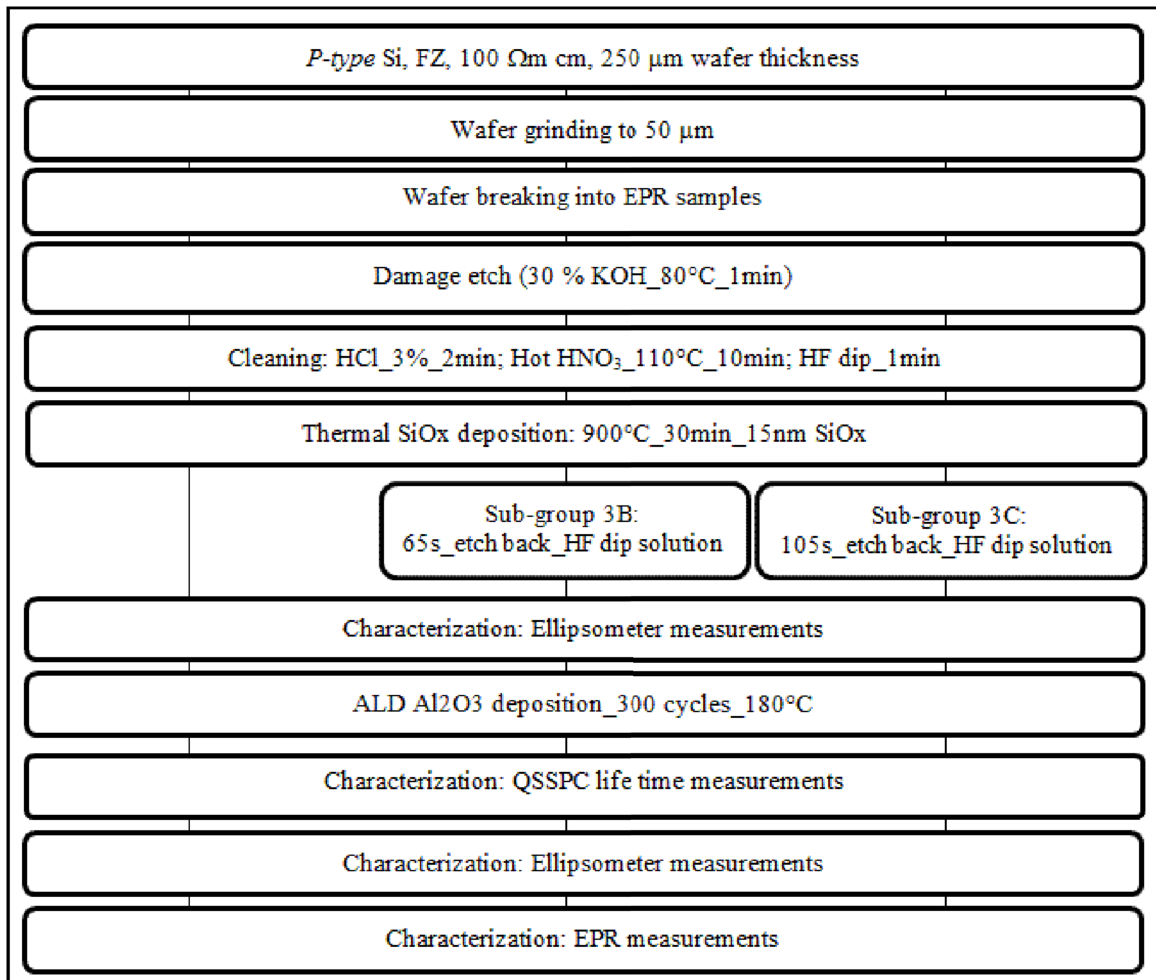

Figure 12-12: experimental flow for group 3

We prepared three groups of samples with different SiOx layer thicknesses to investigate this effect with the EPR technique.

The samples of this group underwent the same cleaning steps as group 1 and 2. After the cleaning step, thermal SiOx was deposited: 900°C, 15 nm SiOx, 30 minutes.

For this group the thickness of the SiOx layer between the Si substrate and the Al2O3 layer is the varying parameter. We decided to study the effect due to three different thicknesses of SiOx: ~15 nm, ~7nm and ~3 nm.

To achieve our scope two reference wafers underwent an etch back process using a HF solution in order to reduce the thickness of the SiOx layer.

A wafer test was used to establish the duration of the etch back process to obtain the desirable thicknesses. The initial thickness of the SiOx layer was measured with the ellipsometer characterization. After that, this wafer underwent a 30 s etch back process using a HF solution. The next step was to measure the thickness of the SiOx layer after the HF etch back with the ellipsometer characterization. This procedure was repeated three times. Figure (12-13) shows the plot of the SiOx layer thickness in function of the etching time.

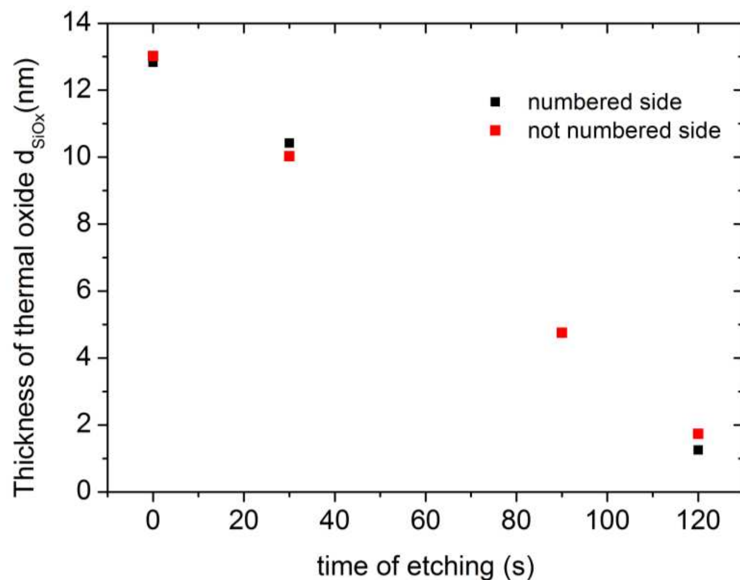

Figure 12-13: Thickness of the thermal oxide SiOx layer versus time of etching. Black dots represent the numbered side and the red dots represent the not numbered side of the reference wafer

From this plot we were able to establish the duration of the etch back process to achieve the desirable thicknesses:

105 s of etching correspond to a thickness of about 3 nm.

65 s of etching correspond to a thickness of about 7 nm.

After the etch back process, all the wafers are deposited with an Aluminum oxide passivation layer on both sides with Plasma Enhanced ALD, 300 cycles, 180°C. Lifetime of the reference wafers was measured using the QSSPC technique.

Table 12-10: Al2O3 thickness (cycles) and lifetime values of group 3

Sub-groups	substrates p FZ-Si thickness	Etch back time(s)	Al2O3 thickness (ALD cycles)	QSSPC lifetime measurements
3A	50 µm	-	300	64 µs
3B	50 µm	65	300	47 µs
3C	50 µm	105	300	42 µs

EPR measurements were made with the same parameters of group 1.To improve the signal-to noise ratio without distorting the EPR line, each spectrum has been averaged over a 537 scans. Measurements were conducted at non saturating power with an attenuation of 20 dB.

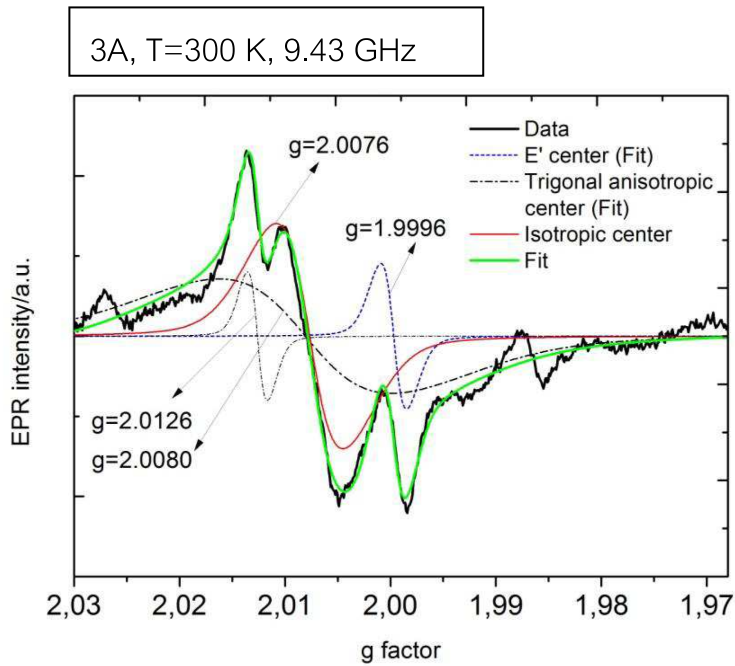

Figure 12-14: Electron Paramagnetic Resonance (EPR) spectra observed at room temperature for atomic layer deposition (ALD, 300 cycles)-grown Si/SiOx (15nm)/Al2O3 interfaces. The thin lines represent the signals of the trigonal anisotropic center (black dots-dashes), the isotropic center (red solid) and the E'-like center (blue dots-dashes) used to fit the experimental data. The thick green solid line is the overall result of the deconvolution

Table 12-11: g-factor values obtained for sub-group 3A

Center number	g factor value	Possible Attribution
Center 1	$g_x = g_Y = g_z = 2.0076 \pm 0.0002$	Si-db [26]
Center 2	$g_{\parallel} = 2.0080 \pm 0.0003$ $g_{\perp} = 2.0126 \pm 0.0002$	Pb0 center [2, 27, 28]
Center 3	$g = 1.9996 \pm 0.0001$	E'-like defect [2]

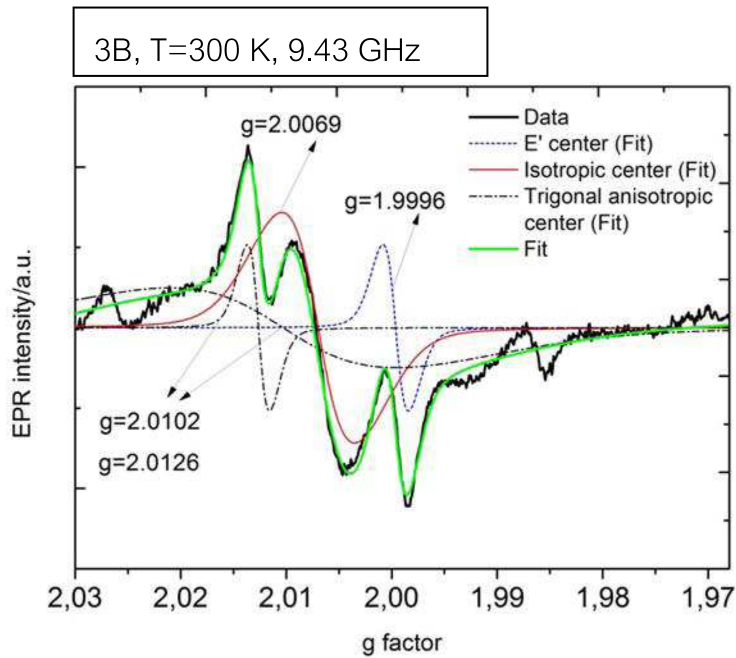

Figure 12-15: Electron Paramagnetic Resonance (EPR) spectra observed at room temperature for atomic layer deposition (ALD, 300 cycles)-grown Si/SiOx (7nm)/Al2O3 interfaces. The thin lines represent the signals of the trigonal anisotropic center (black dots-dashes), the isotropic center (red solid) and the E'-like center (blue dots-dashes) used to fit the experimental data. The thick green solid line is the overall result of the deconvolution

Table 12-12: g-factor values obtained for sub-group 3B

Center number	g factor value	Possible Attribution
Center 1	$g_x = g_Y = g_z = 2.0069 \pm 0.0001$	Si-db [26]
Center 2	$g_{\parallel} = 2.0102 \pm 0.0001$ $g_{\perp} = 2.0126 \pm 0.0001$	Pb0 center [2, 27, 28]
Center 3	$g = 1.9996 \pm 0.0001$	E'-like defect [2]

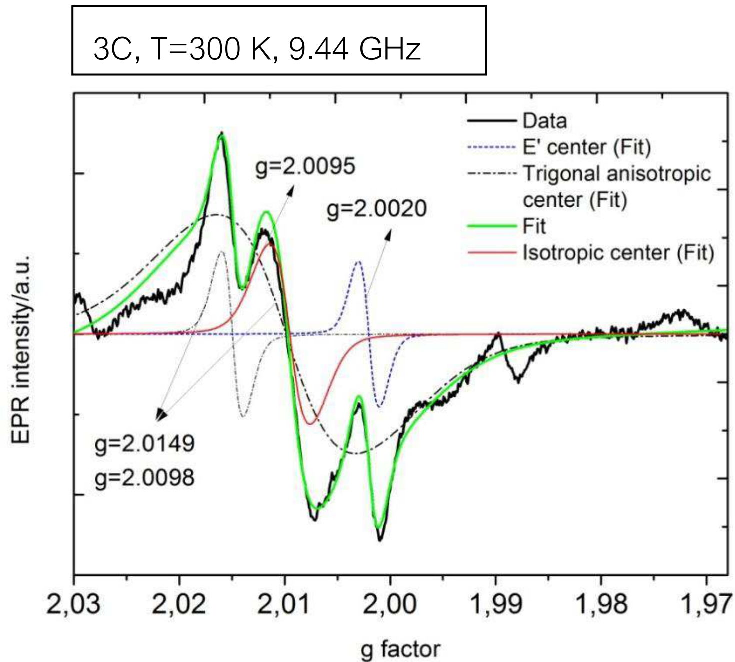

Figure 12-16: Electron Paramagnetic Resonance (EPR) spectra observed at room temperature for atomic layer deposition (ALD, 300 cycles)-grown Si/SiOx (3nm)/Al2O3 interfaces. The thin lines represent the signals of the trigonal anisotropic center (black dots-dashes), the isotropic center (red solid) and the E'-like center (blue dots-dashes) used to fit the experimental data. The thick green solid line is the overall result of the deconvolution

Table 12-13: g-factor values obtained for sub-group 3C

Center number	g factor value	Possible Attribution
Center 1	$g_x = g_Y = g_z = 2.0096 \pm 0.0001$	Si-db [26]
Center 2	$g_{\parallel} = 2.0149 \pm 0.0002$ $g_{\perp} = 2.0098 \pm 0.0001$	Pb0 center [2, 27, 28]
Center 3	$g = 2.0020 \pm 0.0001$	E'-like defect [2]

COCOS MEASUREMENTS

We measured the total negative charge at the Si/SiOx/Al2O3 interface of three reference wafers using the COCOS technique:

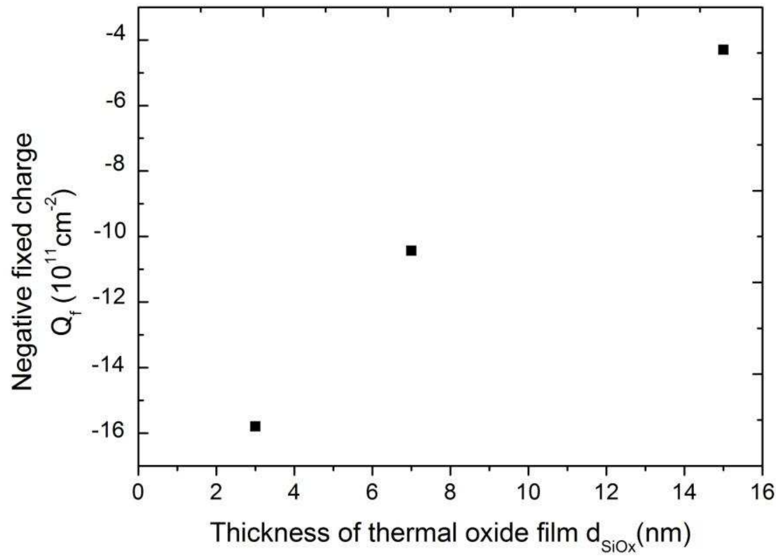

Figure 12-17: Negative fixed charge density vs. thickness of thermal oxide film SiOx

We plotted Qf, the total negative charge at the interface, in function of the SiOx layer thickness.

The results are shown in table:

Table 12-14: total negative charge at the interface in function of the SiOx layer thickness

Sub-group	SiOx thickness(nm)	$\mathrm{Qtot}(\mathrm{cm}^{-2})$
3A	15	$-4{,}3 \cdot 10^{11}$
3B	7	$-10{,}43 \cdot 10^{11}$
3C	3	$-15{,}8 \cdot 10^{11}$

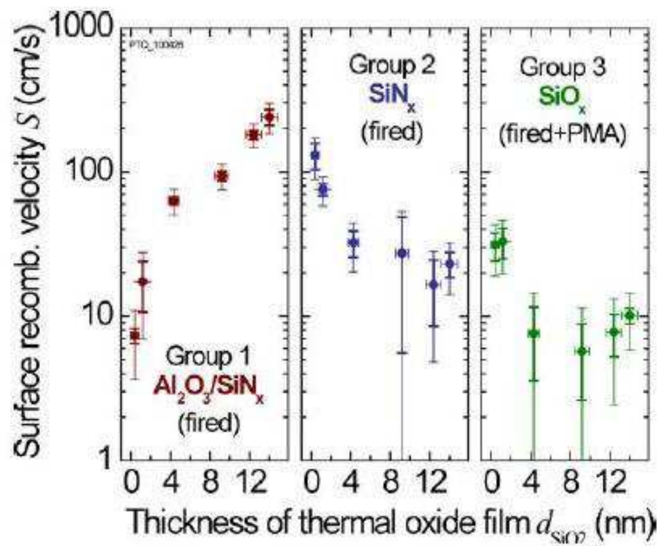

Figure 12-18: Surface recombination velocity versus thermal SiOx thickness for three capping layer systems [33]

Our results are in agreement with those obtained by Mack et al. [34](see figure, Group 1).

The thin thermal SiO2 layer between Si and Al2O3 influences the physical properties of the interface. The surface recombination velocity SRV increases strongly with increasing thickness of the thin thermal SiOx and this leads to a reduction of the density of negative charge to $|Q_{tot}| < 5 \times 10^{11}\ \mathrm{cm}^{-2}$ for $d_{\mathrm{SiO2}} \geq 12\ \mathrm{nm}$ and thus reduces field effect passivation [33]. One explanation to this phenomenon could be that SiO2 acts as a barrier: it could reduce charge injection from the Si substrate into defects states at the SiOx/Al2O3 interface. Studies have demonstrated that this charge injection across the interface may play a role in the formation of the negative charge [2].

SPECTRA ANALYSIS AND DISCUSSION

The spectra in figure appear to be the superposition of an isotropic signal, an E' –like signal and an anisotropic signal. The same results have been obtained for the sub-group 1A. Because of the overlapping of the different lines, it is difficult to extract the anisotropic lines present in the spectra.

All the fits in our work assume Pseudo-Voigt lines. Like subgroup 1A, no signal related to boron interstitial has been observed: all the detected defects may come from the interface.

Table 12-15: g-factor values from spectrum 1A and 3C

Center number	g factor value		Possible Attribution
	Sub-group 1A	Sub-group 3C	
Center 1	$g_x = g_Y = g_z = 2.0068 \pm 0.0002$	$g_x = g_Y = g_z = 2.0096 \pm 0.0001$	Si-db [26]
Center 2	$g_{\parallel} = 2.0012 \pm 0.0002$ $g_{\perp} = 2.0065 \pm 0.0002$	$g_{\parallel} = 2.0149 \pm 0.0002$ $g_{\perp} = 2.0098 \pm 0.0001$	Pb0 center [2, 27, 28]
Center 3	$g = 1.9993 \pm 0.0001$	$g = 2.0020 \pm 0.0001$	E'-like defect [2]

As far as sub-groups 1A and 3C are concerned, the thickness of the SiOx layer between the Si substrate and the Al2O3 layer should be comparable. In fact, Al2O3 deposited by ALD on Si(100) substrates exhibits a very thin interfacial SiOx layer [2, 34]. The presence of this thin SiOx layer was also confirmed by the EPR spectra. In the case of sub-group 3C, on the other hand, we controlled the thickness of the thermal SiOx layer (3nm). If we compare the spectra, they appear to be the superposition of the same signals: an isotropic signal, a E' –like signal and an anisotropic signal. Comparing the spectra however a big shift in the g-factor components of the Center 2 was found. A possible explanation could be the different nature of the oxide. In the case of sub-group 1A, a native SiOx layer is present; for sub-group 3A on the other hand, we deposited a thermal oxide. This difference could be due to different molecular structures.

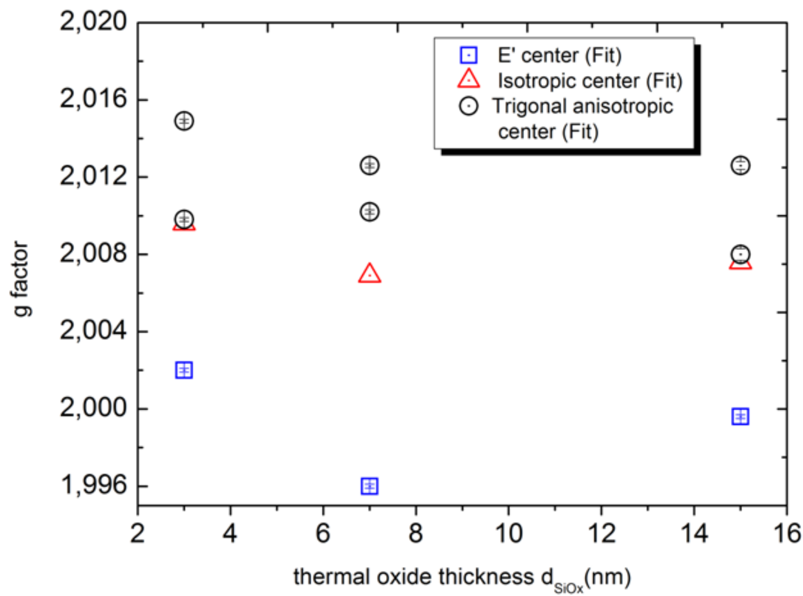

Figure 12-19: g-factors versus thermal oxide thickness of the samples

Group 4

In this experiment we analyzed the EPR spectra of Si/Al2O3 stacked layer after texturing the substrate Si surface.

Surface texturing

Surface texturing is essentially a process used in standard silicon solar cell fabrication to minimize the reflection losses at the front surface. During the process of texturing in mono-crystalline Si substrates, the planar surface of Si wafers is etched along the faces of the crystal planes [35]. When the surface is appropriately aligned with respect to the internal atoms, the structure of the *c*-Si wafer results in a surface made of pyramids. Commercial mono-crystalline silicon solar cells are textured with tetrahedral pyramids consisting of four planes (111) and four edges (100) [35]. To texture Si solar cells anisotropic wet alkaline etchants such as KOH are used.

For these reasons, we expected the concentration of dangling bonds at the Si/Al2O3 surface to be different.

In figure we can see the experimental flow for group 4.

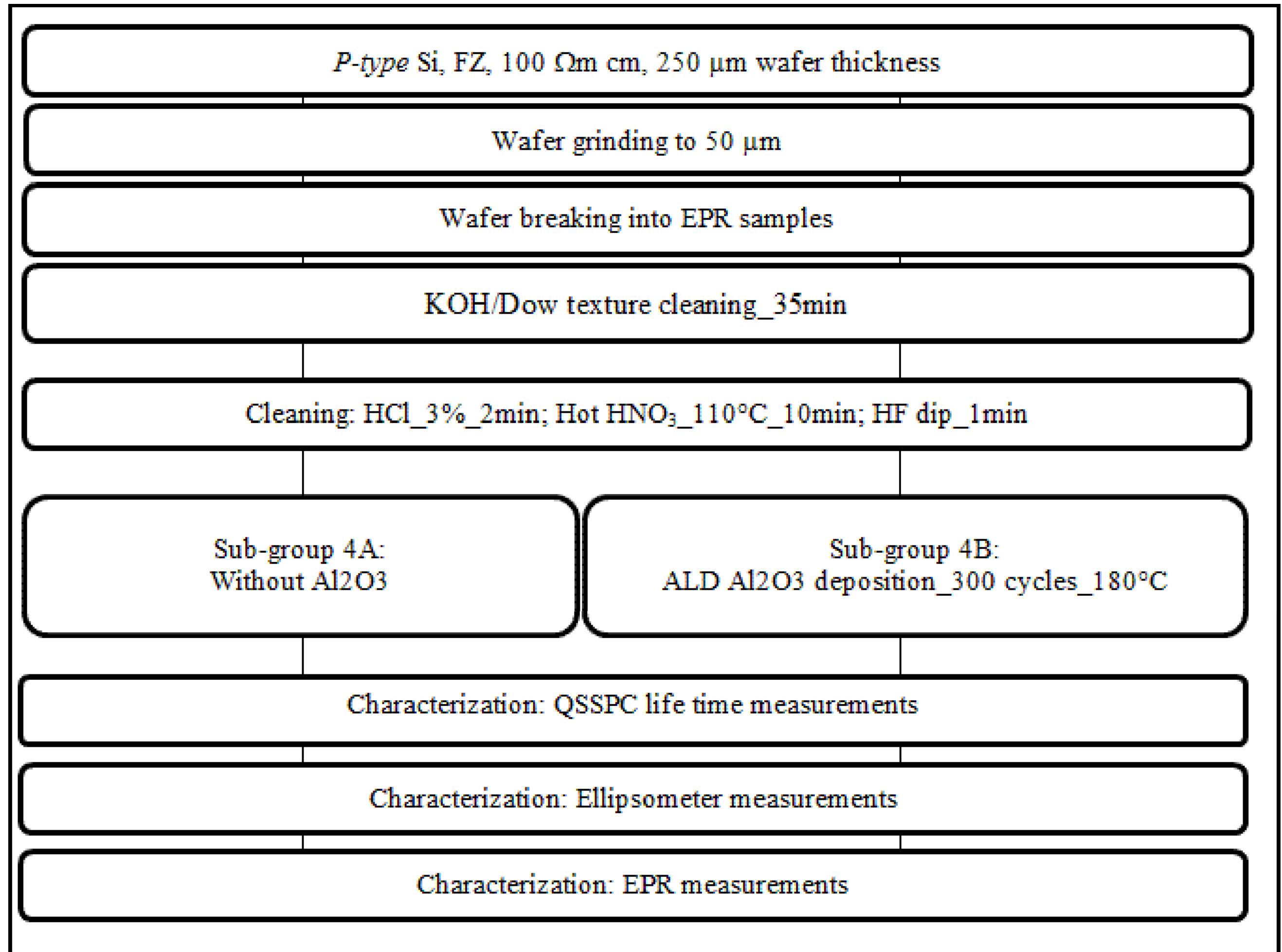

Figure 12-20: experimental flow for group 4

In order to texture the surface of our wafer, the samples underwent a KOH/Dow texture cleaning for 35 minutes. After that they underwent a HCl cleaning for 2 minutes, a HNO3 cleaning for 10 minutes and an HF cleaning for 1 minute as usual.

After the cleaning step the wafers are deposited with an Aluminum oxide passivation layer on both sides with Plasma Enhanced ALD, 300 cycles, 180°C. Lifetime of the reference wafers, with and without Al2O3, was measured using the QSSPC technique.

To improve the signal-to noise ratio without distorting the EPR line, the spectrum has been averaged over a 537 scans. Measurements were conducted at non saturating power with an attenuation of 20 dB.

Table 12-16: substrates thickness and Al2O3 thickness (cycles) of group 4

Sub-groups	substrates p-FZ-Si thickness	Al2O3 thickness (ALD cycles)
4A	50 µm	-
4B	50 µm	300

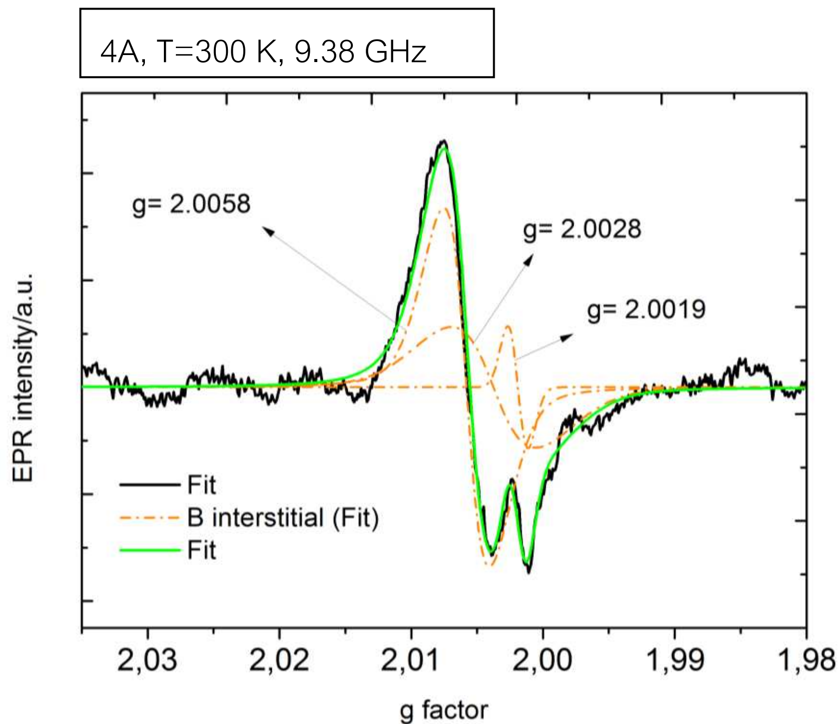

Figure 12-21: Electron Paramagnetic Resonance (EPR) spectra observed at room temperature for a p-type textured FZ-Si layer. The thick black solid line shows the measured data. The thin lines represent the signals of the anisotropic center (orange dashes) used to fit the experimental data. The thick green solid line is the overall result of the deconvolution

Table 12-17: g-factor values obtained for sub-group 4A

Center number	g factor value	Possible Attribution
Center 0	$g_x = 2.0058 \pm 0.0001$ $g_y = 2.0028 \pm 0.0001$ $g_z = 2.0019 \pm 0.0001$	Boron interstitial [24, 25]

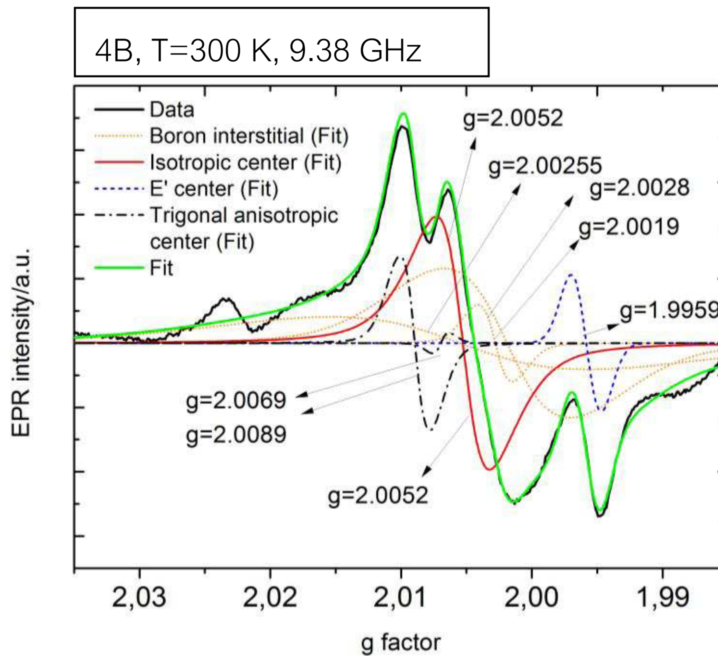

Figure 12-22: Electron Paramagnetic Resonance (EPR) spectra observed at room temperature for atomic layer deposition (ALD, 300 cycles)-grown Si/SiOx (7nm)/Al2O3 textured interfaces. The thin lines represent the signals of the trigonal anisotropic center (black dots-dashes), the isotropic center (red solid), the E'-like center (blue dots-dashes) and the anisotropic center (orange dashes) used to fit the experimental data. The thick green solid line is the overall result of the deconvolution

Table 12-18: g-factor values obtained for sub-group 4B

Center number	g factor value	Possible Attribution
Center 1	$g_x = g_Y = g_z = 2.0052 \pm 0.0001$	Si-db [26]
Center 2	$g_{\parallel} = 2.0069 \pm 0.0001$ $g_{\perp} = 2.0089 \pm 0.0002$	Pb0 center [2, 27, 28]
Center 3	$g = 1.9993 \pm 0.0001$	E'-like defect [2]
Center 0	$g_x = 2.0055 \pm 0.0001$ $g_Y = 2.0028 \pm 0.0001$ $g_z = 2.0019 \pm 0.0001$	Boron interstitial [24, 25]

SPECTRA ANALYSIS AND DISCUSSION

We can at this point make a comparison between spectra Si and 4A. We fitted spectrum 4A with known g-factors values relating to Boron interstitial (gx= 2.0058, gy= 2.0028 and gz= 2.0019). Although our spectra can be well fitted using the same g-factor values, a difference in the shape has been noticed.

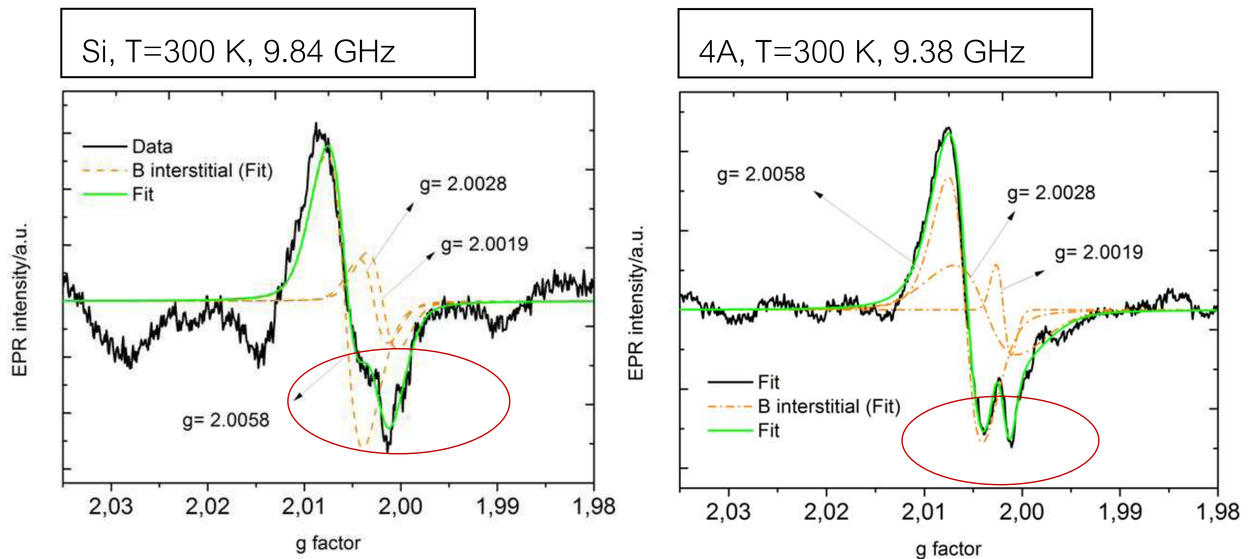

In the first spectrum, the two g-factor components gy=2.0028 and gz= tend to overlap. After texturing the Si surface we can see clearly the effect due to these two different components.

Group 5

In this experiment we analyzed the EPR spectra of Si/Al2O3 stacked layer with a starting substrate of a different thickness in respect with group 1,2,3 and 4. Al2O3 is deposited on a p FZ Si sub-strate, 250 μm thick and with a resistivity of 100 Ohm ·cm.

The aim of this experiment is to investigate the effect of a different thickness of the FZ-Si substrate in the EPR signal and to study the angular dependence of the g values varying the angle between *B* and the (100) interface normal $\hat{n}$ in a range 0°-90°.

The samples underwent a wet chemical cleaning using Nitric acid (HNO3) for 10 minutes at 110°C, followed by (HF) solution for 1 minute. In order to maintain the surface crystal orientation, the samples were not subjected to KOH cleaning.

After the cleaning step the wafers are deposited with an Aluminum oxide passivation layer on both sides with Plasma Enhanced ALD, 300 cycles, 180°C.

In figure we can see the experimental flow for group 5.

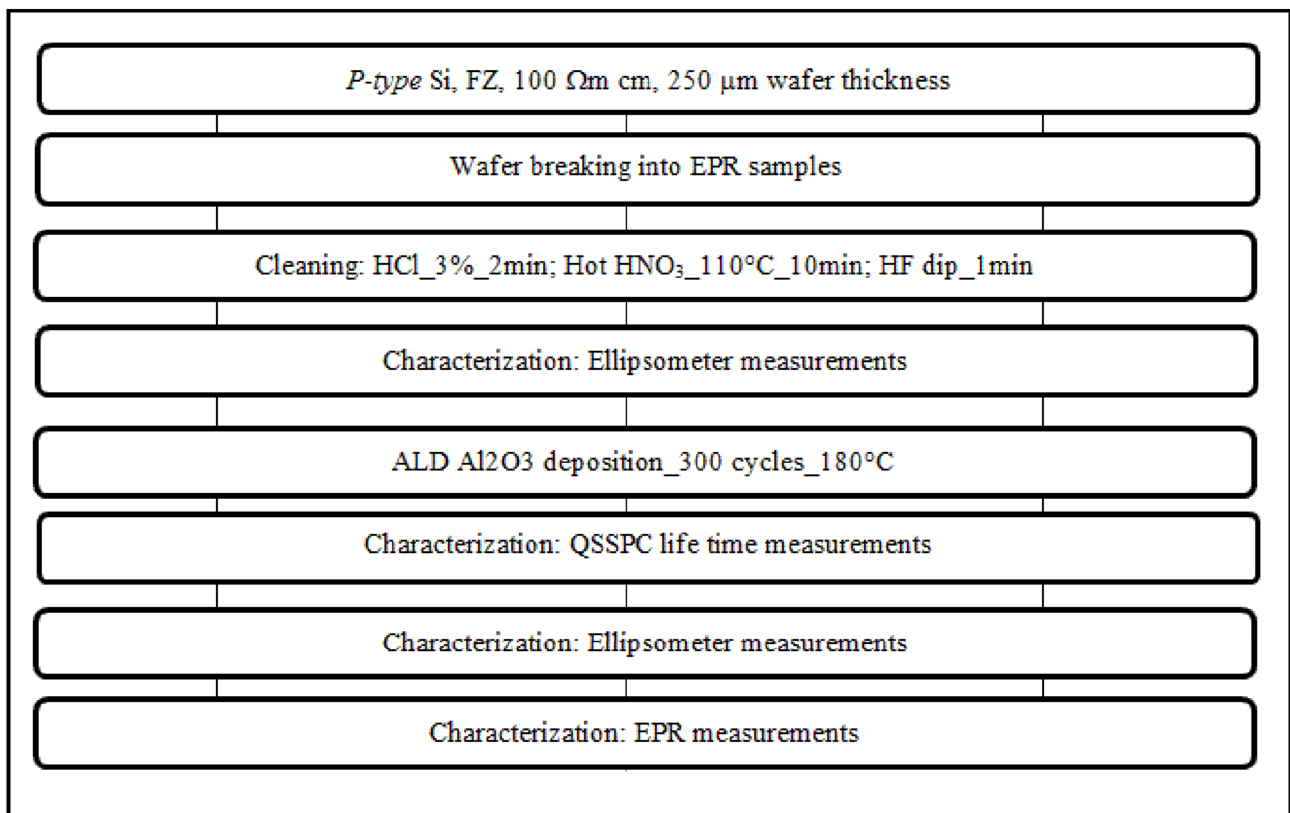

Figure 12-23: experimental flow for group 5

Measurements were carried out on a bundle of ten slices and were conducted at room temperature (300 K). In order to align the samples along the z axis, a thinner quartz tube was inserted in the standard quartz tube. The first measurement was conducted at $B \perp \hat{n}$: the angle was fixed 0°. After each measurement the angle was increased to 15° up to 90°.

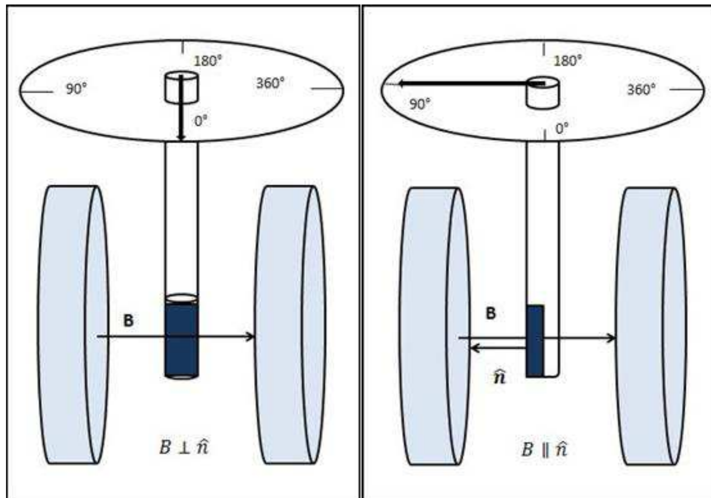

Figure 12-24: experiment set up for our measurements of group 5

The figure above shows the experiment set up for our measurements.

EPR measurements were made with the same parameters of group 1.To improve the signal-to noise ratio without distorting the EPR line, each spectrum has been averaged over a 537 scans. Measurements were conducted at non saturating power with an attenuation of 20 dB.

In the following pictures we reported the spectra of group 5.

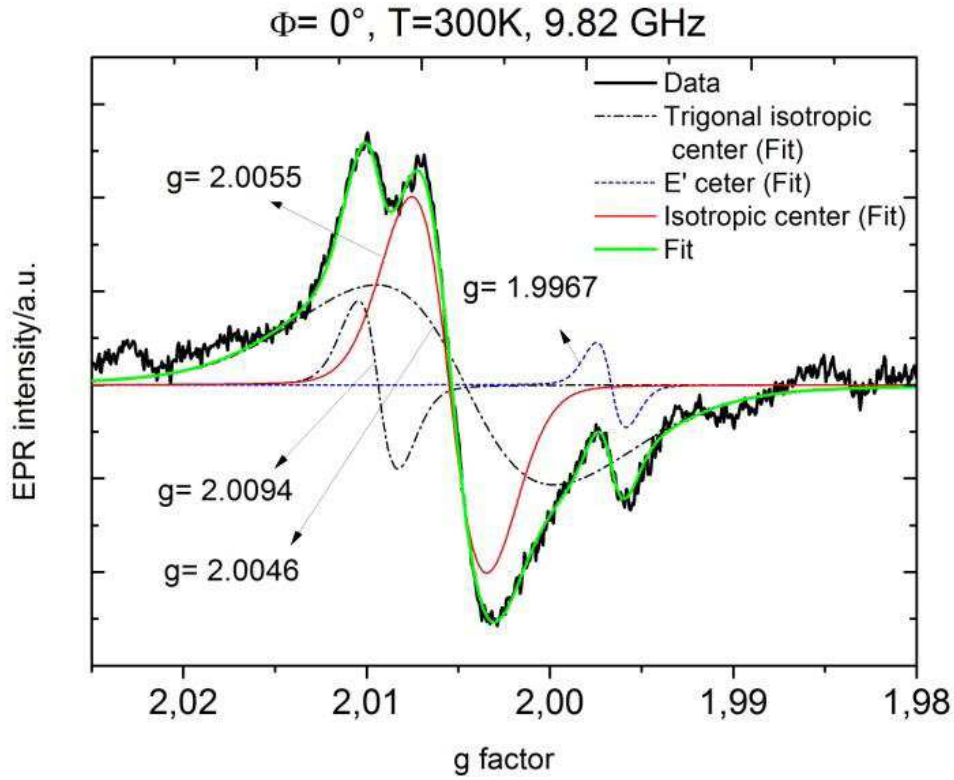

Figure 12-25: Electron Paramagnetic Resonance (EPR) spectra observed at room temperature for atomic layer deposition (ALD, 300 cycles)-grown Si/Al2O3 interfaces. The thick black solid line shows the measured data. The thin lines represent the signals of the trigonal anisotropic center (black dots-dashes), the isotropic center (red solid) and the E'-like center (blue dots-dashes) used to fit the experimental data. The thick green solid line is the overall result of the deconvolution ($\phi = 0°$)

Table 12-19: g-factor values obtained for sub-group φ=0°

Center number	g factor value	Possible Attribution
Center 1	$g_x = g_y = g_z = 2.0055 \pm 0.0001$	Si-db [26]
Center 2	$g_{\parallel} = 2.0094 \pm 0.0002$ $g_{\perp} = 2.0046 \pm 0.0002$	Pb0 center [2, 27, 28]
Center 3	$g = 1.9967 \pm 0.0001$	E'-like defect [2]

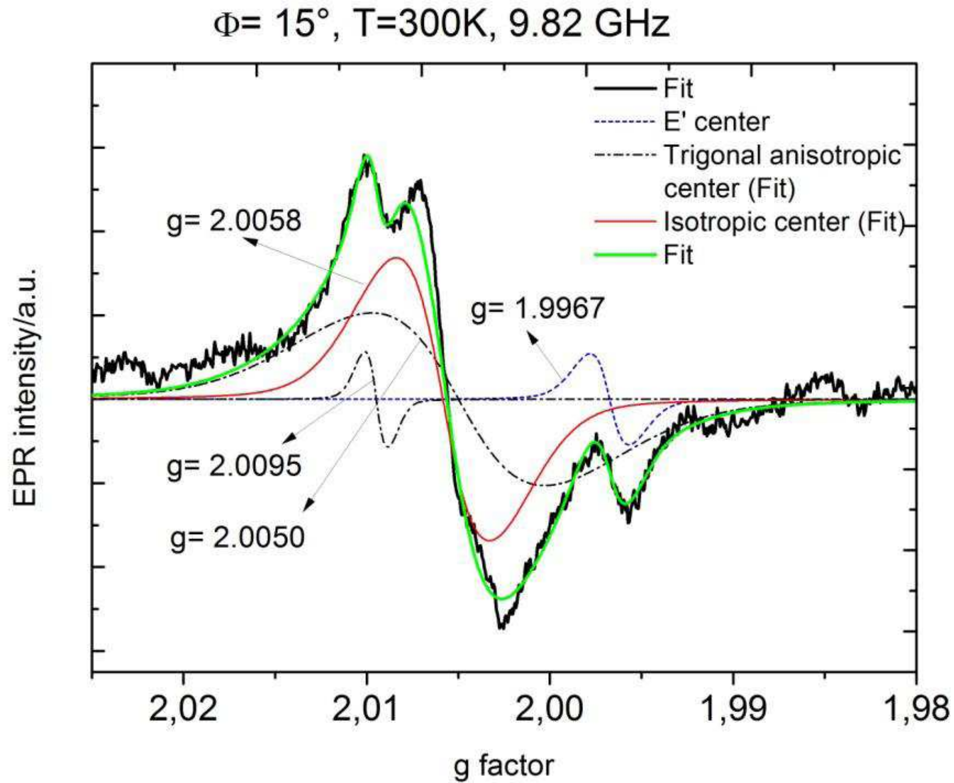

Figure 12-26: Electron Paramagnetic Resonance (EPR) spectra observed at room temperature for atomic layer deposition (ALD, 300 cycles)-grown Si/Al2O3 interfaces. The thick black solid line shows the measured data. The thin lines represent the signals of the trigonal anisotropic center (black dots-dashes), the isotropic center (red solid) and the E'-like center (blue dots-dashes) used to fit the experimental data. The thick green solid line is the overall result of the deconvolution ($\phi = 15°$)

Table 12-20: g-factor values obtained for sub-group φ=15°

Center number	g factor value	Possible Attribution
Center 1	$g_x = g_y = g_z = 2.0058 \pm 0.0001$	Si-db [26]
Center 2	$g_{\parallel} = 2.0095 \pm 0.0002$ $g_{\perp} = 2.0050 \pm 0.0003$	Pb0 center [2, 27, 28]
Center 3	$g = 1.9967 \pm 0.0001$	E'-like defect [2]

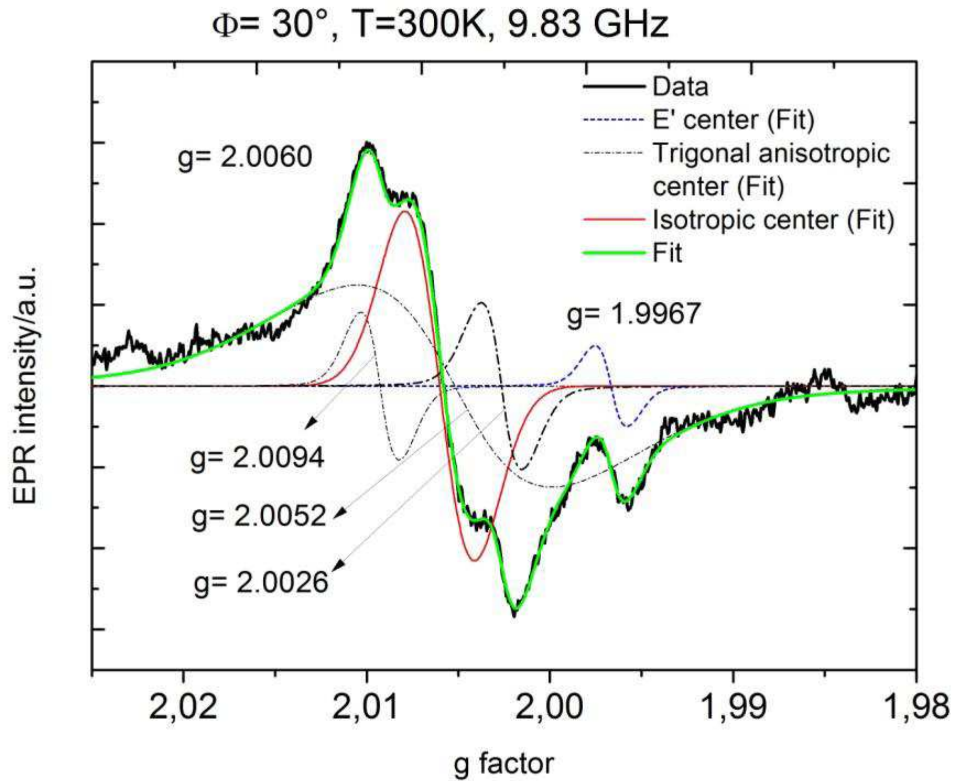

Figure 12-27: Electron Paramagnetic Resonance (EPR) spectra observed at room temperature for atomic layer deposition (ALD, 300 cycles)-grown Si/Al2O3 interfaces. The thick black solid line shows the measured data. The thin lines represent the signals of the trigonal anisotropic center (black dots-dashes), the isotropic center (red solid) and the E'-like center (blue dots-dashes) used to fit the experimental data. The thick green solid line is the overall result of the deconvolution ($\phi = 30°$)

Table 12-21: g-factor values obtained for sub-group φ=30°

Center number	g factor value	Possible Attribution
Center 1	$g_x = g_y = g_z = 2.0060 \pm 0.0001$	Si-db [26]
Center 2	$g = 2.0094 \pm 0.0002$ $g = 2.0052 \pm 0.0002$ $g = 2.0026 \pm 0.0001$	Pb0 center [2, 27, 28]
Center 3	$g = 1.9967 \pm 0.0001$	E'-like defect [2]

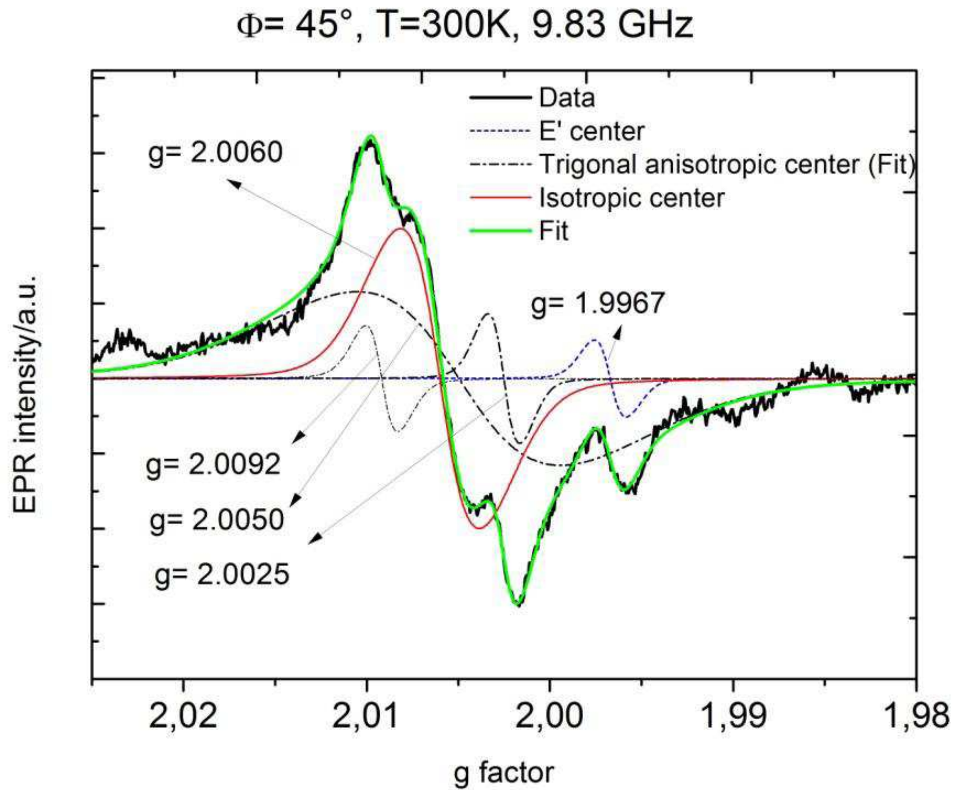

Figure 12-28: Electron Paramagnetic Resonance (EPR) spectra observed at room temperature for atomic layer deposition (ALD, 300 cycles)-grown Si/Al2O3 interfaces. The thick black solid line shows the measured data. The thin lines represent the signals of the trigonal anisotropic center (black dots-dashes), the isotropic center (red solid) and the E'-like center (blue dots-dashes) used to fit the experimental data. The thick green solid line is the overall result of the deconvolution ($\phi = 45°$)

Table 12-22: g-factor values obtained for sub-group φ=45°

Center number	g factor value	Possible Attribution
Center 1	$g_x = g_y = g_z = 2.0060 \pm 0.0001$	Si-db [26]
Center 2	$g_{\parallel} = 2.0092 \pm 0.0001$ $g_{\perp} = 2.0050 \pm 0.0002$ $g = 2.0025 \pm 0.0001$	Pb0 center [2, 27, 28]
Center 3	$g = 1.9967 \pm 0.0001$	E'-like defect [2]

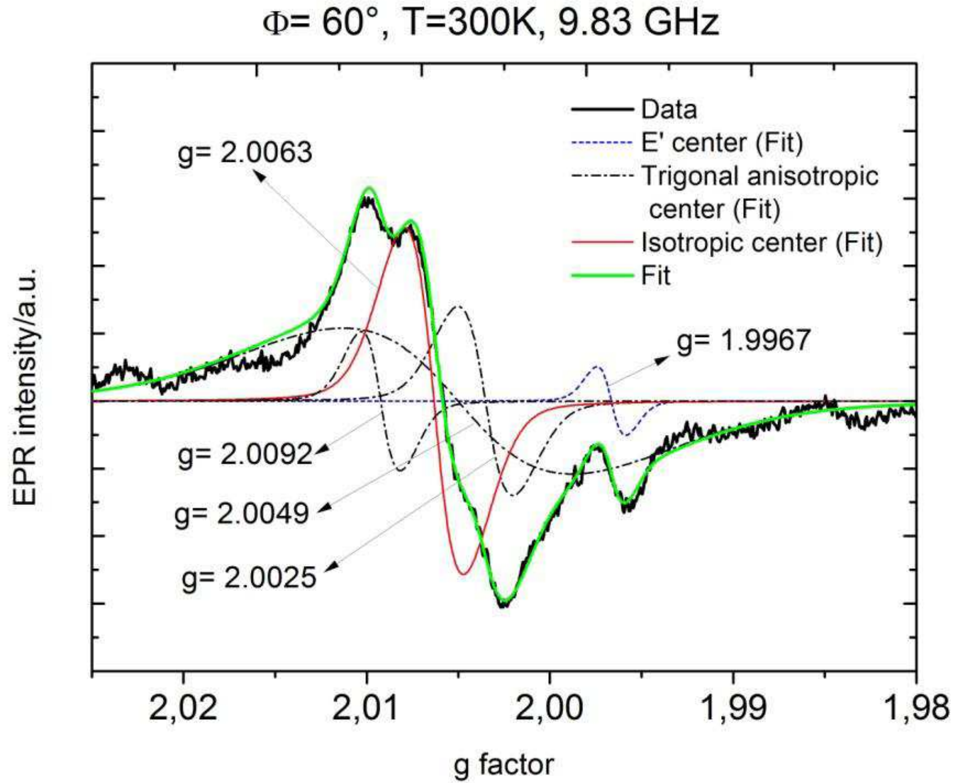

Figure 12-29: Electron Paramagnetic Resonance (EPR) spectra observed at room temperature for atomic layer deposition (ALD, 300 cycles)-grown Si/Al2O3 interfaces. The thick black solid line shows the measured data. The thin lines represent the signals of the trigonal anisotropic center (black dots-dashes), the isotropic center (red solid) and the E'-like center (blue dots-dashes) used to fit the experimental data. The thick green solid line is the overall result of the deconvolution ($\phi = 60°$)

Table 12-23: g-factor values obtained for sub-group φ=60°

Center number	g factor value	Possible Attribution
Center 1	$g_x = g_y = g_z = 2.0063 \pm 0.0001$	Si-db [26]
Center 2	$g = 2.0092 \pm 0.0002$ $g = 2.0049 \pm 0.0002$ $g = 2.0025 \pm 0.0002$	Pb0 center [2, 27, 28]
Center 3	$g = 1.9967 \pm 0.0001$	E'-like defect [2]

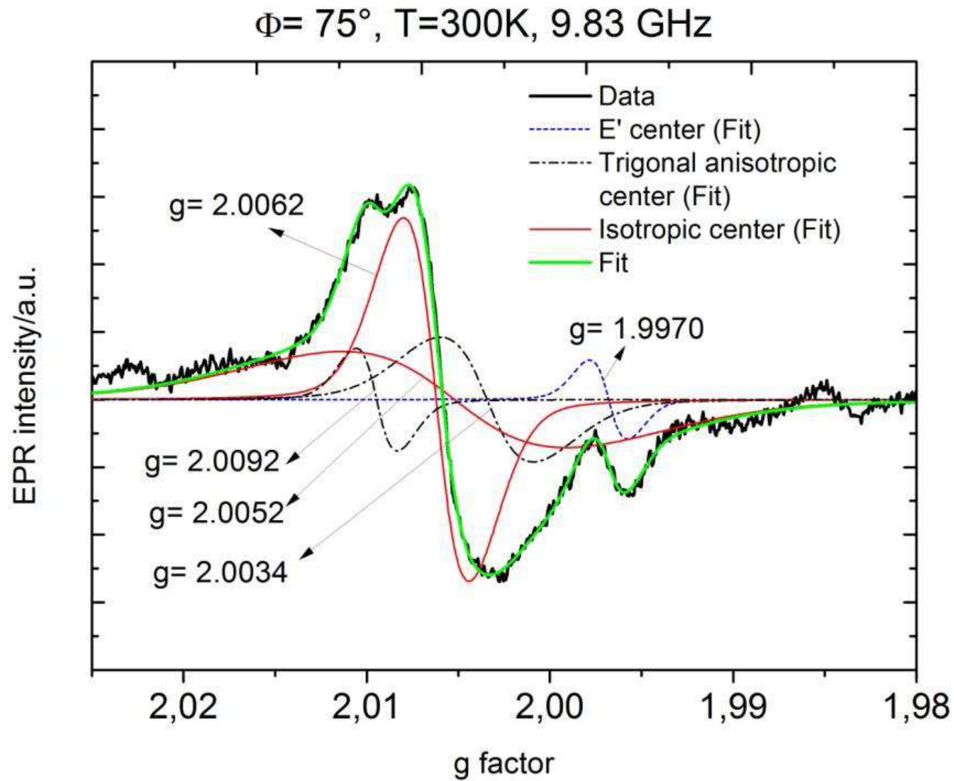

Figure 12-30: Electron Paramagnetic Resonance (EPR) spectra observed at room temperature for atomic layer deposition (ALD, 300 cycles)-grown Si/Al2O3 interfaces. The thick black solid line shows the measured data. The thin lines represent the signals of the trigonal anisotropic center (black dots-dashes), the isotropic center (red solid) and the E'-like center (blue dots-dashes) used to fit the experimental data. The thick green solid line is the overall result of the deconvolution ($\phi = 75°$)

Table 12-24: g-factor values obtained for sub-group φ=75°

Center number	g factor value	Possible Attribution
Center 1	$g_x = g_y = g_z = 2.0062 \pm 0.0001$	Si-db [26]
Center 2	$g = 2.0092 \pm 0.0001$ $g = 2.0052 \pm 0.0001$ $g = 2.0034 \pm 0.0001$	Pb0 center [2, 27, 28]
Center 3	$g = 1.9967 \pm 0.0001$	E'-like defect [2]

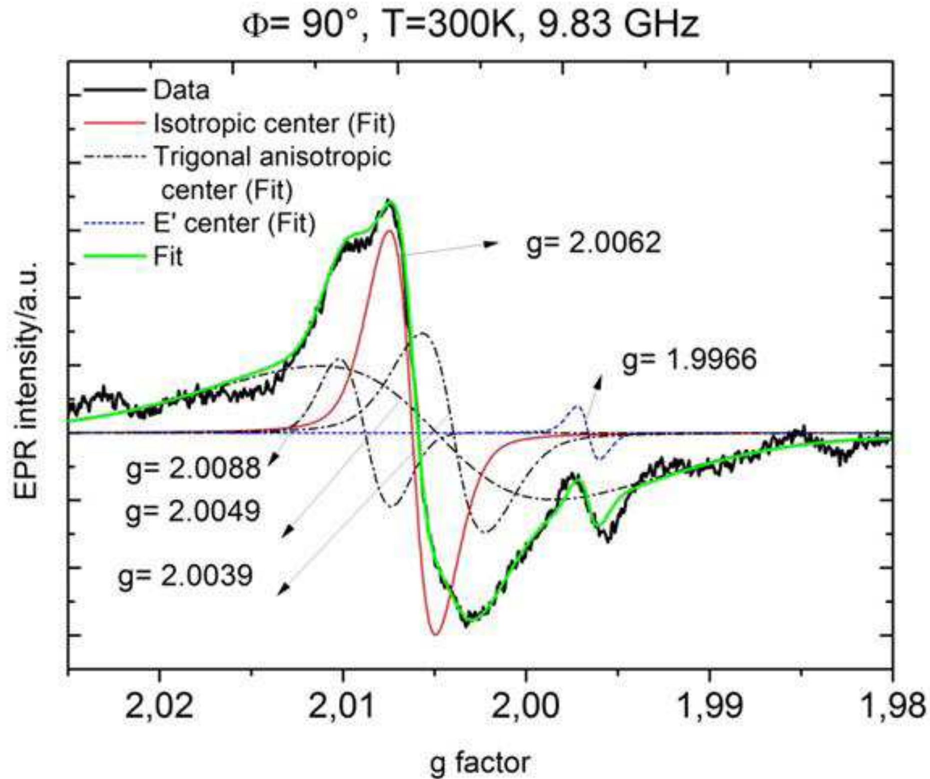

Figure 12-31: Electron Paramagnetic Resonance (EPR) spectra observed at room temperature for atomic layer deposition (ALD, 300 cycles)-grown Si/Al2O3 interfaces. The thick black solid line shows the measured data. The thin lines represent the signals of the trigonal anisotropic center (black dots-dashes), the isotropic center (red solid) and the E'-like center (blue dots-dashes) used to fit the experimental data. The thick green solid line is the overall result of the deconvolution ($\phi = 90°$)

Table 12-25: g-factor values obtained for sub-group φ=90°

Center number	g factor value	Possible Attribution
Center 1	$g_x = g_y = g_z = 2.0062 \pm 0.0002$	Si-db [26]
Center 2	$g = 2.0088 \pm 0.0004$ $g = 2.0049 \pm 0.0002$ $g = 2.0039 \pm 0.0003$	Pb0 center [2, 27, 28]
Center 3	$g = 1.9967 \pm 0.0001$	E'-like defect [2]

SPECTRA ANALYSIS AND DISCUSSION

In all the spectra we found the presence of signals due to the trigonal anisotropic center, the isotropic center and the E'-like center. For the first two sub-group $\phi = 0°$ and $\phi = 15°$, the best fit were obtained using for the trigonal anisotropic center, as fitting parameters, $g_{\parallel} = 2.0094 \pm 0.0002$; $g_{\perp} = 2.0046 \pm 0.0002$ (for $\phi = 0°$) and $g_{\parallel} = 2.0095 \pm 0.0002$; $g_{\perp} = 2.0050 \pm 0.0003$ (for $\phi = 15°$).

As far as the anisotropic trigonal center is concerned, for the other angles the best fit were obtained using three g-factor components as fitting parameters.

In the figure below we reported a graph showing the angular dependence of the g-factors observed in ALD grown Si/Al2O3, rotating the sample: angles were varied in the range 0°-90° with an accuracy of 5°. Figure 14-6 shows our experiment set up.

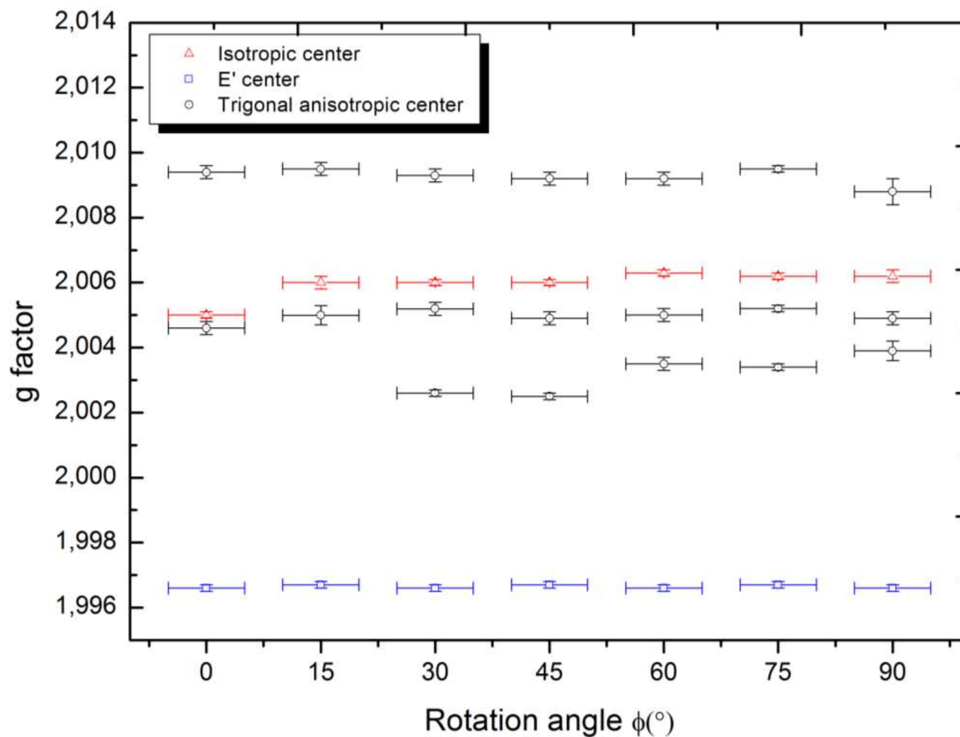

Figure 12-32: Angular dependence of the g-factors observed in ALD grown Si/Al2O3, rotating the sample

13 Conclusion

The reduction of the film thickness to nanometer dimensions is one possible way to achieve cost competitiveness in the semiconductor industry. The surface to volume ratio is increasing and that leads to electrical losses due to surface recombination. Thin films of Al2O3 are favorable for the passivation of the p-type silicon surfaces. The passivation properties of this dielectric material are related to a decrease of the interface defect density combined with an enhancement of the field effect passivation by a significant increase of negative fixed charge density Qf during annealing. Therefore, experiments were carried out to understand the origin of this negative fixed charge. The presence of a SiOx interlayer between Si and Al2O3 appers to play a key role in the origin of the negative charge formation and in the interface defect density. It has been demonstrated that an increase in the SiOx interlayer thickness over the range 1-30 nm gives rise to a decrease in negative Qf. As a matter of fact, SiOx acts as a barrier, reducing charge injection from the Si substrate into defect states at the SiOx/Al2O3 interface. In our study this effect has been demonstrated using the *COCOS* technique (see *Appendix*): we measured the total negative charge at the Si/SiOx/Al2O3 interface of three reference wafers and we found out the the negative charge denisity Qf decreases with the increase of the SiOx layer thickness.

Simulations and experiments have provided evidence that the negative charge at the SiOx/Al2O3 interface may be related to Al vacancy V_{Al} and O interstitial O_{i} .

In addition, for annealed Al2O3 samples, the fixed negative charge density was observed to increase. In our study, using the COCOS technique, also this effect has been demonstrated (see group 2 in section 12-2).

To detect the physical and chemical nature of the interfacial defects, electron paramagnetic resonance (EPR) was found to be a powerful technique. EPR is a spectroscopic technique that detects species that have unpaired electrons. Many authors have reported that Si/Al2O3 interface exhibits P_b-type defect. This kind of defects is a trivalently bonded Si atom and it represents the prominent electronically active defects characteristic of the Si/SiOx interface. Our observations, using EPR spectroscopy, are in line with the formation of an interfacial SiOx layer. Analysing the spectra of group 1 (Si/Al2O3), it was possible to identify an isotropic center, an E'-like defect and an anisotropic center (P_{b0}-like). The same results were obtained by Dingemans et al. [2]. The E'-like defects are associated with the SiOx interface. After an annealing step, EPR did not reveal the presence of any defect states.

Finally, in our work we studied the angular dependence of the g values varying the angle between *B* and the (100) interface normal $\hat{n}$ in a range 0°-90°. In all the spectra we found the presence of signals due to the trigonal anisotropic center, the isotropic center and the E'-like center in line with our expectations.

14 Appendix

14.1 Corona-Oxide-Semiconductor Characterization

Corona-oxide-semiconductor characterization is a technique for characterization of semiconductor. Positive or negative charge comes from a corona source and it deposited on a semiconductor sample surface. A high voltage source is used by the corona source to ionize room air. The corona source produces a uniform flow of ionized air molecules toward the wafer surface. The molecules retain very little kinetic energy during the process because of the short atmospheric mean free path of ionized gas.

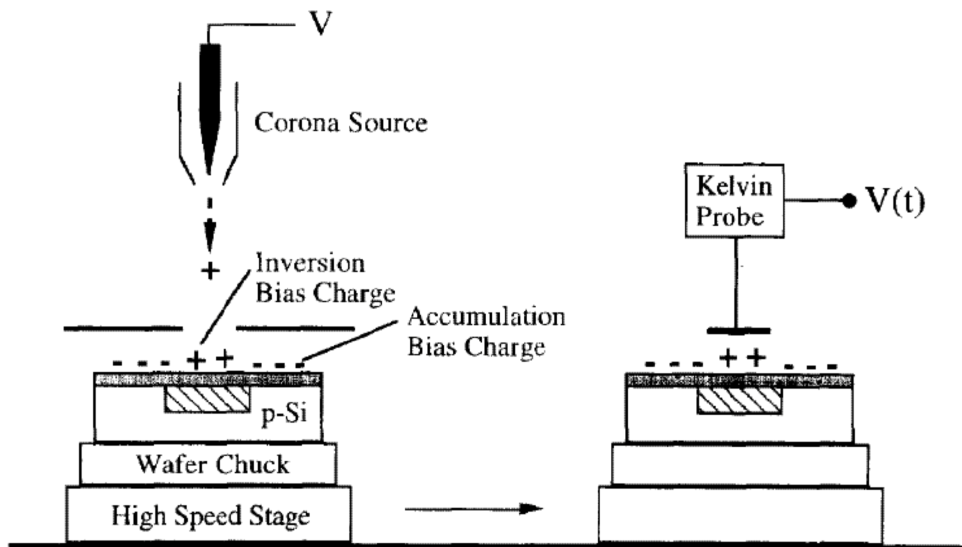

Figure 14-1: Negative charge is deposited locally on an oxidized p-Si wafer [36]

Positive charge is deposited in two possible modes:

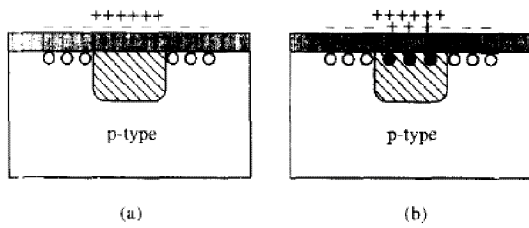

Figure 14-2: Semiconductor substrate pulsed into deep-depletion from a) accumaltion, b) depletion [36]

In the first mode, the device is driven by the positive charge pulse from accumulation into deep depletion. Also in the second mode the charge pulse drives the device from accumulation into deep depletion: the device can then reach inversion. After that, a second positive charge pulse drives the device from inversion into deep depletion. In this mode only the substrate bulk properties are measured: interface electron- hole pair generation is reduced. Then, after the deposition of the charge, we have to determine the transient response of the device. The sample moves from the corona source to a Kelvin probe, where the voltage is measured [36].

14.2 Experimental set up: pictures

In this section some pictures of our experimental set up are reported.

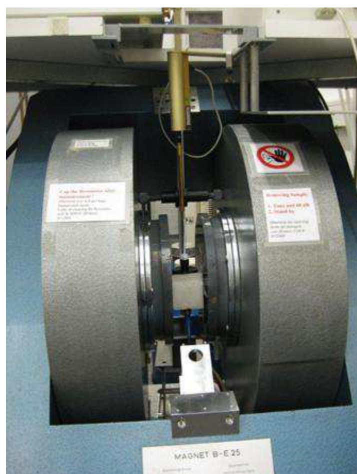

Figure 14-3: The sample is in a cavity, which is a metal box that helps to amplify

weak signals from the sample.There is a magnet to tune the electronic energy levels

Figure 14-4: The *Bruker* console contains signal processing and control electronics and a computer

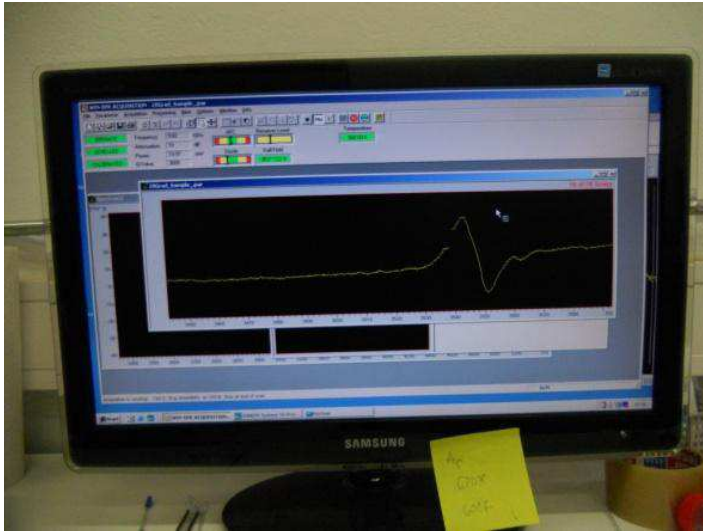

Figure 14-5: The computer is used for analyzing data and coordinating all the units for acquiring a spectrum

Figure 14-6: our experiment set up for the measurements of group 5

15 Acknowledgements

Firstly, I would like to express my sincere gratitude to my Professor *Anna Cavallini*, for giving me the opportunity to perform my Master thesis at the Fraunhofer Institue for Solar Energy Systems (ISE) in Freiburg, for her suggestions, support and encouragement during the master thesis.

I would like to offer my special thanks to my group leader at the Fraunhofer ISE, Dr. *Marc Hofmann* for giving me the opportunity to work with his group and for his professional guidance.

I am extremely gratefull to my supervisor *Saskia Kuehnhold* for assisting me anytime, for her valuable suggestions and encouragement.

Secondly, I would like to thank all my friends at ISE, especially *Daniele, Rekha, Eugene, Luis, Davide, Ino, Tim and Torge*, for their company, friendship and support. I wish to thank also all my friends in Freiburg, especially *Martina, Simon, Mario, Jakob, Giovanni, Marika, Teresa, Margerita, Anais, Robert, Michael*, for their unconditional help during the good and bad times. Their company had made this experience one of the best experiences of my life.

I would also like to extend my thanks to all my Professors in Bologna, for their support and encouragement.

Furthermore, it would not have been possible to write this thesis without the help and support of the kind people around me: I would like to thank all my collegues and friends in Bologna, especially *Alessandra, Cristiano, Laura, Silvia, Giulia, Francesco, Marco, Julian, Matteo, Federico, Valeria, Margherita, Luca, Alice, Silvia and Annalisa*, for their love and encouragement.

Last but not least, I wish to thank my family, my mother *Morena* and my father *Roberto*, for their infinite support throughout everything with their best wishes. Without you I would never been able to finish this dissertation: thank you with all my heart.

Bibliography

1. S.M.Sze, *Phisics of Semiconductor Devices.* 2007.
2. Dingemans, G. and E. Kessels, *Status and prospects of Al2O3-based surface passivation schemes for silicon solar cells.* Journal of Vacuum Science & Technology A: Vacuum, Surfaces, and Films, 2012. **30**(4): p. 040802-040802-27.
3. H.Bube, R., *Photovoltaic Materials*. 1998.
4. A.Neamen, D., *Semiconductor Physics and Devices*. 2003.
5. Biro, D., et al. *Thermal oxidation as a key technology for high efficiency screen printed industrial silicon solar cells*. in *Photovoltaic Specialists Conference (PVSC), 2009 34th IEEE*. 2009.
6. Ashcroft, M., *Solid State Physics.* 1976.
7. Hofmann, M., *Rear Surface Conditioning and Passivation for Locally Contacted Crystalline Silicon Solar Cells*. 2008.
8. Oliver Schultz, A.M., Martin Hermle. Stefan W. Glunz, *Progress in Photovoltaics*. 2008.
9. Kerr, M.J. and A. Cuevas, *Very low bulk and surface recombination in oxidized silicon wafers.* Semiconductor Science and Technology, 2002. **17**: p. 35-8.
10. Hong, J., et al., *Influence of the high-temperature "firing" step on high-rate plasma deposited silicon nitride films used as bulk passivating antireflection coatings on silicon solar cells.* Journal of Vacuum Science & Technology B: Microelectronics and Nanometer Structures, 2003. **21**(5): p. 2123-2132.
11. Gatz, S., et al., *Thermal stability of amorphous silicon/silicon nitride stacks for passivating crystalline silicon solar cells.* Applied Physics Letters, 2008. **93**(17): p. 173502.
12. Kittel, C., *Introduction to Solid State Physicsc*. 1996.
13. B.G.Streetman, *Solid State Electronics*, ed. Prenticeall. 1990.
14. Sinton, R.A., A. Cuevas, and M. Stuckings. *Quasi-steady-state photoconductance, a new method for solar cell material and device characterization*. in *Proceedings of the*

25th IEEE Photovoltaic Specialists Conference. 1996. Washington DC, USA: IEEE; New York, NY, USA.

15. Nagel, H., C. Berge, and A.G. Aberle, *Generalized analysis of quasi-steady-state and quasi-transient measurements of carrier lifetimes in semiconductors.* Journal of Applied Physics, 1999. **86**(11): p. 6218-6221.
16. S.Rein, *Lifetime Spectroscopy: A Method of Defect Characterization in Silicon for Photovoltaic Applications*. Springer--Verlag Berlin Heidelberg (2005).
17. H.Macdonald, D., *Recombination and Trapping in Multicrystalline Silicon Solar Cells*, in *The Australian National University,(2001).*
18. *<Spectroscopic Ellipsometry Principles and Applns - H. Fujiwara (Wiley, 2007) 0470016086.pdf>.*
19. Lenahan, P.M. and J.F. Conley, *What can electron paramagnetic resonance tell us about the Si/SiO2 system?* Journal of Vacuum Science & Technology B: Microelectronics and Nanometer Structures, 1998. **16**(4): p. 2134-2153.
20. Eisberg, R. and R. Resnick, *Quantum Physics of atoms, molecules, solids, nucley, and particles*. 1923, United States of America.
21. John A. Weil, J.R.B., *Electron Paramagnetic Resonance: Elementary Theory and Practical Applications, Second Edition*. 2007.
22. George, S.M., *Atomic Layer Deposition: An Overview.* Chem. Rev. 2010, 110, 111–131.
23. Karen A. Reinhardt, W.K., *Handbook of Silicon Wafer Cleaning Technology (Materials Science and Process Technology)*, W.K. Karen A.Reinhardt, Editor.
24. Watkins, G.D., *Defects in irradiated silicon: EPR and electron-nuclear double resonance of interstitial boron.* Physical Review B, 1975. **12**(12): p. 5824-5839.
25. Watkins, G.D., *EPR of a trapped vacancy in boron-doped silicon.* Physical Review B, 1976. **13**(6): p. 2511-2518.
26. Jones, B. and R. Barklie, *Electron paramagnetic resonance evaluation of defects at the (100) Si/Al2O3 interface.* Journal of Physics D: Applied Physics, 2005. **38**(8): p. 1178.

27. von Bardeleben, H.J.C., J. L., *EPR Studies of the Microscopic Structure of the (100) Si/SiO2 Interface: current status and perspectives.* Brazilian Journal of Physics, 1997. **vol. 27**(Issue 2): p. p.314-324.

28. Baldovino, S., et al., *Investigation of point defects at the high-k oxides/Si(100) interface by electrically detected magnetic resonance.* Journal of Non-Crystalline Solids, 2003. **322**(1–3): p. 168-173.

29. Thareja, G., *Electron Spin Resonance of interface defects at the Si-SiO2 interface.* March 21, 2007(Submitted as coursework for AP272, Stanford University, Winter 2007).

30. Poindexter, E.H., et al., *Interface states and electron spin resonance centers in thermally oxidized (111) and (100) silicon wafers.* Journal of Applied Physics, 1981. **52**(2): p. 879-884.

31. Stathis, J.H. and L. Dori, *Fundamental chemical differences among Pb defects on (111) and (100) silicon.* Applied Physics Letters, 1991. **58**(15): p. 1641-1643.

32. *Electron Spin Resonance Characterization of Defects at Interfaces in Stacks of Ultrathin High-**K** Dielectric Layers on Silicon.* MRS Proceedings, 2003. **786**: p. E1.4.

33. Mack, S., et al., *Silicon surface passivation by thin thermal oxide/PECVD layer stack systems.* IEEE Journal of Photovoltaics, 2011. **1**(2): p. 135-45.

34. Hoex, B., et al., *Silicon surface passivation by atomic layer deposited Al_2O_3.* Journal of Applied Physics, 2008. **104**: p. 044903.

35. McIntosh, K.R. and L.P. Johnson, *Recombination at textured silicon surfaces passivated with silicon dioxide.* Journal of Applied Physics, 2009. **105**(12): p. 124520.

36. Schroder, D.K., et al., *CORONA-OXIDE-SEMICONDUCTOR device CHARACTERIZATION.* Solid-State Electronics, 1998. **42**(4): p. 505-512.